The Nansen Environmental and Remote Sensing Center

NERSC

a non-profit
research institute affiliated with
the University of Bergen

Thormøhlensgate 47,
N-5006 Bergen
Norway

DOPSCAT

Feasibility Investigation of Global Ocean Surface Current Mapping using ERS, MetOp and QuikScat Wind Scatterometer

ESTEC Contract N° 4000/10/NL/AF 4000102097

Study team:

NERSC, Norway
CLS, France
KNMI, the Netherlands
ARESYS, Italy
TAS, France
Ifremer, France.

NERSC

Ifremer

CLS
COLLECTE LOCALISATION SATELLITES

Koninklijk Nederlands
Meteorologisch Instituut
Ministerie van Infrastructuur en Milieu

ThalesAlenia Space

aresys

The Nansen Environmental and Remote Sensing Center

Nansen Environmental and Remote Sensing Center
Thormøhlensgate 47
N-5006 Bergen - NORWAY
Phone: +47 55 20 58 00 Fax. +47 55 20 58 01
E-mail: administrasjon@nersc.no Web.site: http://www.nersc.no

a non-profit environmental research center affiliated with the university of Bergen

REPORT

TITLE Feasibility Investigation of Global Ocean Surface Current Mapping using ERS, MetOp and QuikScat Wind Scatterometer	**REPORT No.** NERSC Technical Report # 331
CLIENT **European Space Agency**	**CONTRACT No.** 4000/10/NL/AF 4000102097
CONTACT PERSONS Johnny A. Johannessen	**AVAILABILITY**
AUTHORS J.A. Johannessen, K.-F. Dagestad, F. Collard, Pierre Fabry, Romain Housson, A. Stoffelen, J. de Kloe, B. Chapron, A. Recchia, J. Richard, Vivien Enjolras	**DATE** July 9, 2013
APPROVAL	

CONTENT

NOTE THAT THE DESCRIPTION OF THE DOPSCAT SIMULATOR IS PROVIDED IN A SEPARATE DOCUMENT

1 Introduction

Objectives and Approach

DOPSCAT aims at assessing the potential of scatterometer instruments for sea surface currents retrieval whereas these instruments are primarily designed for surface wind vector estimation. The objectives are two fold:

- To obtain some preliminary results on the existing scatterometer data capitalizing on new signal processing techniques;
- To propose an optimized scatterometer concept maintaining the good directional NRCS detection performances and coverage for wind vector retrieval but, at the same time, allowing Doppler shift estimation with sufficient accuracy for surface current measurement.

Together with the new concept ideas, the project will provide recommendations on signal processing techniques and required geophysical model function for surface current retrieval from the Doppler estimates.

The study team expertise and composition is outlined below.

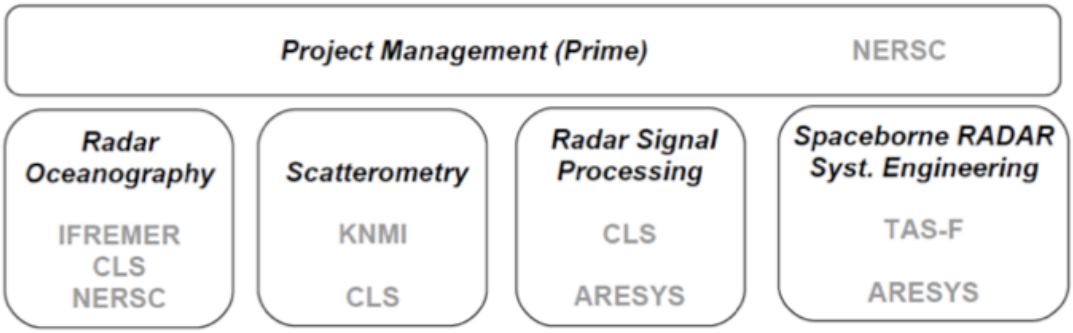

The study approach has the following breakdown:

• WP 1000: Review of user requirements and achievements using SAR data

• WP 2000: Analyses of the adequacy of the existing scatterometer data for surface current estimation

• WP 3000: Case studies using selected data sets for extraction of surface current information

• WP 4000: Provision of recommendation for future scatterometer development

• WP 5000: Project coordination and management

The flowchart illustrates the logic and major connections between the different WPs and Sub-WPs. This progress report will predominantly focus on WP 1000 with the Sub-WPs 1100 and 1200 which are importantly feeding into WP2000.

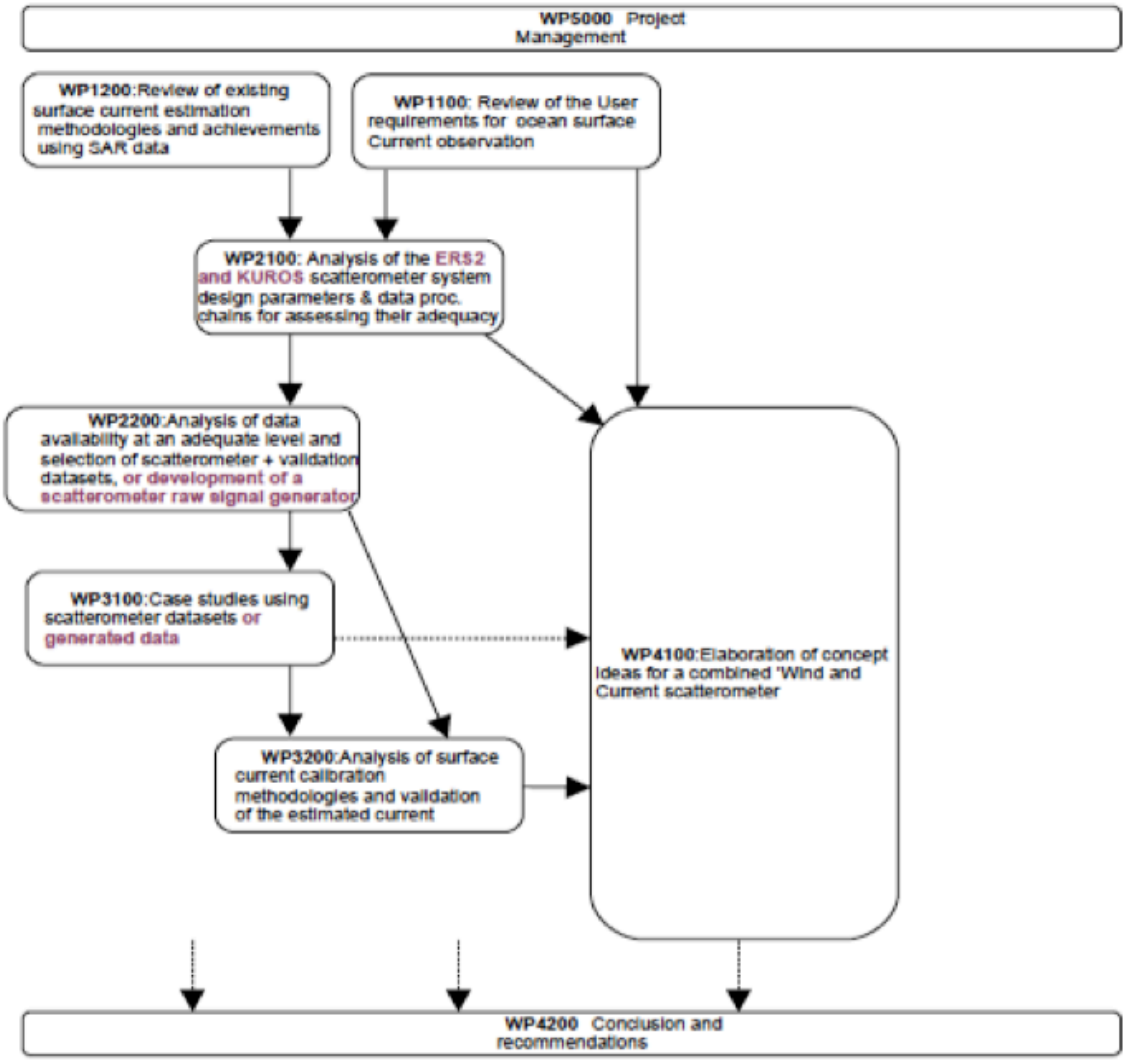

Figure 1. *Flowchart illustrating the logic and major connections between the different WPs and Sub-WPs.*

2. TASK REPORTS

Task 1000
Sub-Task 1100: Review of user requirements for ocean surface current observations

Ocean circulation is one of the most important parameters regulating and determining the Earth´s climate. An example is the great impact of the Gulf Stream for the West European climate. Sea surface currents also transport and distribute biogeochemical material including biomass and pollutants. Currents are generated from the forces acting upon the water mass including the rotation of the Earth, winds, temperature and salinity differences and tidal forces. Additionally, the depth contours, the shoreline influence the currents' direction and strength.

A basic tool for measuring the oceanographic topography and subsequently derive the surface geostrophic current is the radar altimeter. This method is presently undergoing great improvements as a result of new quantitative knowledge of the marine geoid from the GRACE and GOCE satellites. Yet, the ocean's mesoscale and submesoscale energy is difficult to map with conventional radar altimeters and gravity missions because of the narrow illuminated swath as well as spatial resolution of the gravity field (> 200 km). For instance, eddies in the North Atlantic have typical radii of 20-30 km, elevation amplitudes of 40-60 cm, translational velocities of 2.5 km/day and orbital motion of around 0.5 m/s. Moreover they are known for their complex 2-3 D dynamics including convergence and divergence bands that are not in geostrophic balance. Hence, direct 2D mapping of such open ocean eddies and their characteristic surface velocity field including estimation of vorticity and divergence is yet inadequate.

For coastal applications, the geostrophic assumption is often also not supported. The structure of surface currents in the coastal environment is generally very complex, dominated by the local bathymetry, tidal cycles, and wind and sea state conditions. Imaging instruments are then certainly more ideally suited for coastal observations. Conventional along-track interferometry techniques can provide a measure of the instantaneous sea surface scatterer velocity by measuring the phase difference between two return signals from the same surface patch, separated by a very short time interval. Direct instantaneous frequency determination from the phase history analysis of single antenna returns is less conventional, but can also be used to evaluate the mean velocity of scatterers on the ocean surface. Both techniques have demonstrated the feasibility to infer current velocities along the radar line-of-sight direction. These techniques have the potential to meet very high spatial resolution requisites of the order of km, but have the disadvantage that only one component of the two-component surface current is mapped. Furthermore the radar line-of-sight velocity is strongly influenced by the wind generated wavelet motion, long wave orbital velocities, wind and residual wave drifts (Chapron et al. 2005; Mouche et al. 2008; Johannessen et al., 2008; Hansen et al., 2011). These sources must be correctly removed before the strength of the range directed surface current can be determined.

Based on the existing literature (see Robinson 2005, references in Ocean Surface Currents Web and Robinson and Birnk 2005), an initial list with the characteristic velocities of some characteristic ocean current regimes has been compiled in Table 1. This table also contains the typical temporal and spatial scales of the different current structures and clearly reveals the contrast between open ocean current features and common coastal ocean current features

(e.g. tidal currents). The total dynamic range of surface currents is rarely exceeding 4-5 m/s. However, the range varies from current regimes to current regimes such as, for instance, associated with exceptionally strong tidal currents versus mesoscale eddy currents.

Moreover, the measurement retrieval accuracy is also highly important. Typically this must be less than approximately 0.10 m/s and independent of current regimes as indicated in Table 2 after e.g. Stammer et al., 2007; IGOS Coastal Theme Report, 2006.

Phenomenon	Approximate time scale (hr)	Approximate Length scale (km)	Approximate Velocity scale (cm s^{-1})
Equatorial currents	240	50-100	10 – 150
Western boundary currents	48	10-100	10 – 200+
Ocean mesoscale eddies	120	10-20	10 – 50
Ocean fronts	120	1-5	30
Tidal currents	1	0.1 – 20	10 – 200+
Coastal current	6	0.1-5	5 - 50

Table 1. Characteristic velocities arranged according to oceanic phenomena

Source	Application	Units	Accuracy			Δx (km)			Δt (hr)			δ (hr)		
			tsh	brk	obj	ths	brk	obj	thrs	brk	obj	thrs	brk	obj
Stammer et al (2007)	Golobal Oceanography	cm s^{-1}.	10	5	1	100	50	15	360	240	120	7d		3h
	Coastal oceanography	cm s^{-1}.	10	5	1	1	0.1	0.01	12	3	1	1		0.15
	Surge/shelf modelling	cm s^{-1}.	10	5	1	1	0.1	0.01	12	3	1	1		0.15
	Marine dispersion	cm s^{-1}.	1	1	0.5	5	5	0.1	3	1	0.5	120		2
IGOS Coastal Theme Report (2006)	Coastal currents	cm s^{-1}.	10	?	3	5	?	0.3	24	?	1	1		1
UK National Centre for Ocean	Global operational ocean forecasting	cm s^{-1}.	20		10	60		5	24	0.3	1	1		0.1

Table 2. Characteristic retrieval accuracies, spatial and temporal resolutions and product delay time.

Considering the values in these tables as a general guide to surface current characterization and observation requirements a number of regions can be specified as suitable for case studies to investigate the satellite retrievals of ocean surface currents using scattreometers, including:

1. Energetic boundary currents with strong thermal and ocean colour features large enough to cause atmospheric instability and surface roughness changes: The Gulf Stream region centred on [38.32° N, -64.78° E]
2. Agulhas Current retro-reflection with strong thermal and ocean colour features large enough to cause atmospheric instability and surface roughness changes. Additional large surface waves due to wind-current interactions. Suggested region centred on [-37.5° N, 18.5° E]
3. Regional sea with small tidal currents but strong thermal and ocean colour features. Additional internal wave surface manifestations in the Western Mediterranean: Mediterranean Sea centred on [36.0° N, 3.0° W]
4. Coastal up-welling region off the coast of Spain and Portugal with energetic mesoscale dynamics and coastal jets are expected during up-welling events and atmospheric stability centred on [40.5° N, 10.0° W]
5. Open ocean gyre with small surface currents centred on [46.0° N, 34.0° W]

An example of the impact of the strong Agulhas Current on the scatterometer wind retrievals is shown in Figure 2 (top) that displays the absolute wind speed difference between scatterometry and ECMWF wind climatology. The elongated pattern of the wind speed anomaly reaching up to 1.3 m/s is clearly having a shape in good agreement with the southwestward flow of the Agulhas Current core shown in Figure 2 (bottom) as depicted from the range Doppler velocity and sea surface temperature map. This illustrates (somehow) that there might be a leakage between roughness and velocity estimates from the Doppler method. Ideally, the perfect case is to consider the Bragg case, and the Doppler shift is simple to interpret, and the surface current velocity easy to deduce. When the Doppler shift results from a combination of sources as mentioned above, the derived range directed surface velocity is also controlled by meter-scale waves. If these waves are themselves impacted in their development by the underlying current, the cross section will change, and so will the Doppler shift. This may be tested using the DOPRIM to assess the interplay between the forcing impacted by the surface current, the resulting strength of roughness, and the Doppler shift

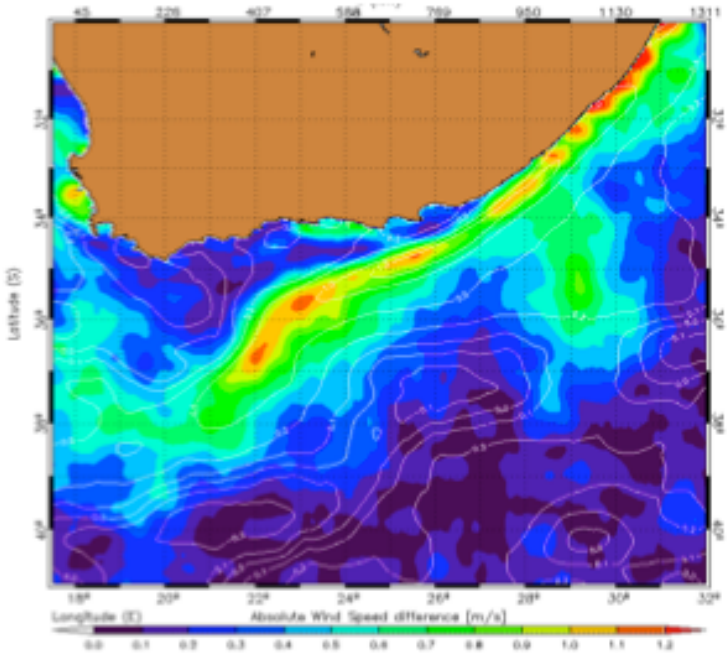

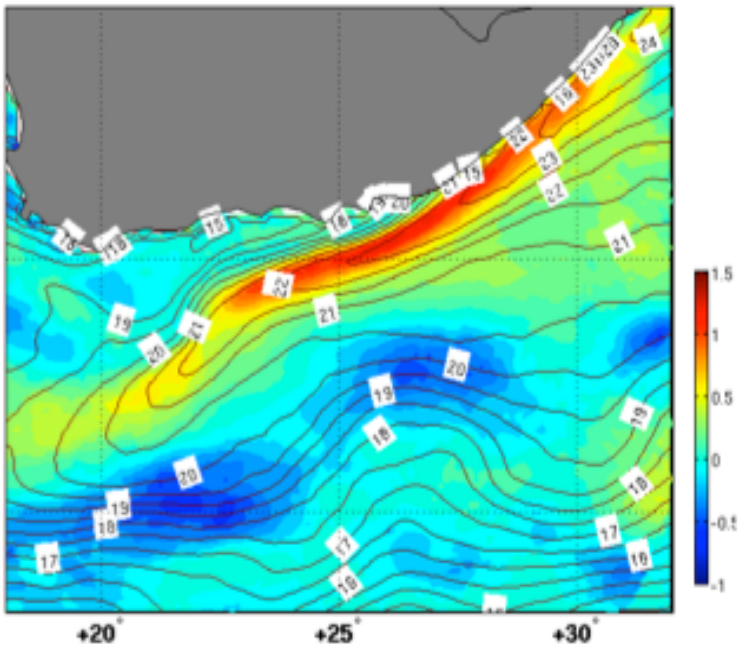

Figure 2. *Wind speed anomalies (top) and range Doppler velocity and SST (bottom)*

In this study these regional characteristics are used to define the dynamic range of surface currents spanning from 0.05 m/s to 4 m/s with a retrieval accuracy of ~ 0.10 m/s at a spatial and temporal resolution of approximately 10 km and 12-24 hours. Note that better accuracy (cm/s) is needed over longer integration time. Moreover, the obzservation requirements for tidal currents are not feasible in terms of satellite based resolution and time variability. These are rather well suited to be covered by coastal HF/VHF radars and therefore not further considered in this Doppler scatterometer study.

Task 1000

Sub-Task 1200: Review of existing surface current estimation methods and achievements using SAR data.

The ASAR wide-swath products, now include the Doppler centroid grid, with a sampling of about 5 km in range and 10 km in azimuth can also be used to estimate reliable geophysical Doppler shift. Quite some pre-processing steps are required to go from the raw Doppler centroid towards a geophysical Doppler shift. First an estimation of a reference Doppler centroid is performed using ESA-CFI orbit propagator software, then any remaining bias over land is removed. Finally non-geophysical biases in range and also backscatter related biases in azimuth are filtered out. Once we get to a geophysical Doppler shift or velocity, a last geophysical processing step based on CDOP is performed to estimate the radial surface current. Before applying systematic corrections of the Doppler velocities based on CDOP wind dependant Doppler shift, it was impossible to perform systematic quantitative estimations of surface current when the wind direction was significantly off the SAR azimuth direction. For all radial surface current derived from SAR in this paper, we have applied the CDOP correction using ancillary wind direction data. Any error in the wind direction will then lead to an error on the CDOP correction and subsequently on the surface current estimate.

Unfortunately, with ENVISAT orbit, no scatterometer wind direction data are sufficiently close in space and time to be used (ASCAT on METOP is close in time but not on the same orbit as ENVISAT) so global atmospheric model wind direction are used. As shown later, correction is larger at low incidence angle. On the contrary, surface current radial component is larger at large incidence angle. As a result, the ratio between surface current and CDOP correction is much larger at high incidence angles and therefore the error caused by wind direction error, lower. High incidence angles are therefore, more suitable for surface current estimation from Doppler shift. An example of the correction effect is illustrated in Fig. 3.

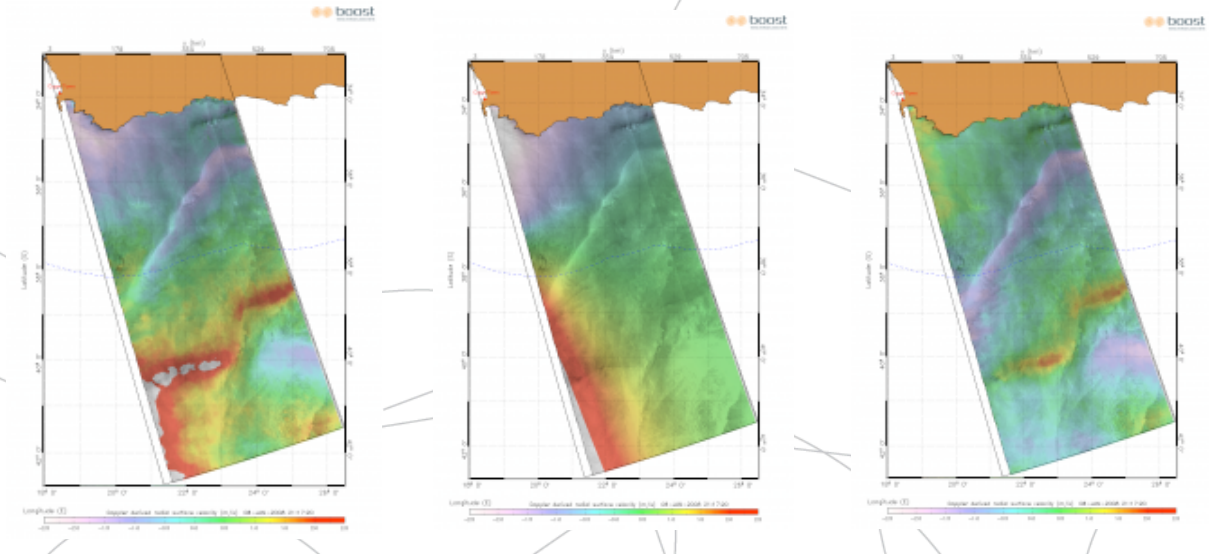

Figure 3: *Illustration of the wind correction effect on the case of the Agulhas current for the January 08 2008 at 21 h 15 min 43 sec. a) total observed radial velocities from Doppler shift. b) Predicted sea state related Doppler shift using CDOP model and ancillary ECMWF surface wind data. c) Difference between total observed radial velocities and predicted sea state Doppler velocities.*

Even in this Agulhas Current regime with very intense surface currents, the wind corrections at low incidence angles are of the same order of magnitude or larger than the residual signal from radial surface currents. The correction is therefore mandatory to provide an unbiased radial surface current estimate. Resulting radial surface current has then been compared to radial velocities recorded by a few Lagrangian drifters available under the swath of ASAR wide swath within 6 hours from the satellite overpass (see Figure 4 and 5).

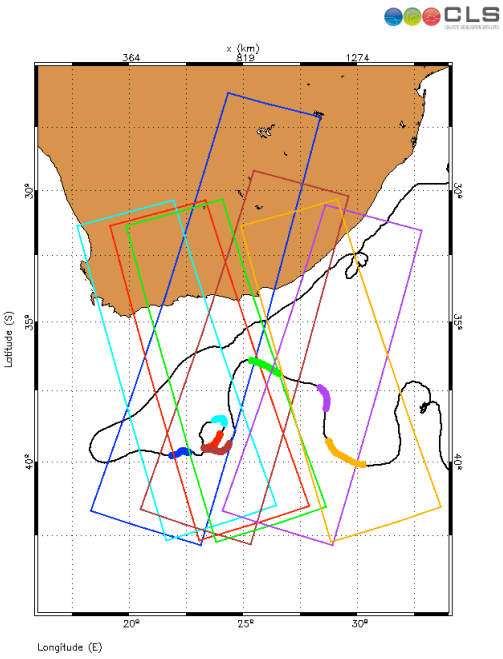

Figure 4: *ASAR wide swath acquisitions over a Lagrangian drifter in the Agulhas region*

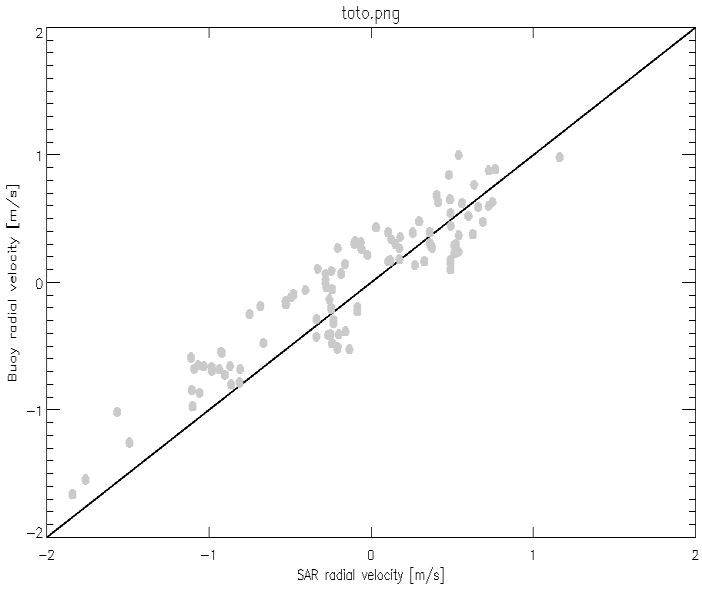

Figure 5: *Comparison of radial surface current estimate from SAR and Lagrangian drifter velocities projected to radial SAR direction*

Calibration of SAR Doppler shifts. This consists in removing Doppler contributions that are not related to surface motion (e.g. satellite motion) but also contributions that are not induced by motions but by miss-pointing. Estimation of Doppler shift related to satellite motion and mechanical miss-pointing may be accomplished by using a geometric model such as the Envisat CFI software which estimates the return frequency from a moving radar platform at given incidence angle and satellite attitude. Using this information with the CFI software, we are then able to get a geometrically predicted Doppler to use for the estimation of Doppler centroid anomalies, further providing information about the sea surface motion.

However, the precise pointing of the antenna boresight is not only affected by mechanical miss-pointing but also by a slowly varying electronic miss-pointing caused by the uncoordinated drift of the active antenna individual TR modules. To calibrate the Doppler shift caused by these drifts, the range dependant bias can be calibrated by using nearly land in the same or close orbit.

The Doppler Centroid grid as provided is ASAR WSM products is estimated on 12 consecutive bursts of Level 0 data and 356 range lines after range and azimuth focussing. The aim is to look at the potential of this information for ocean current information retrieval. This grid of estimates is however not directly ready for geophysical interpretation as a measure of sea surface motions. First one needs to extract the anomaly of this Doppler estimate compared to a reference model of a frozen surface. And secondly one needs to correct for the non

geophysical biases in the Doppler Centroid estimates. The necessary steps to derive a geophysical grid of Doppler anomaly estimates from the initial raw Doppler Centroid estimates grid provided in ASAR WSM products (see Figure 6) is provided below.

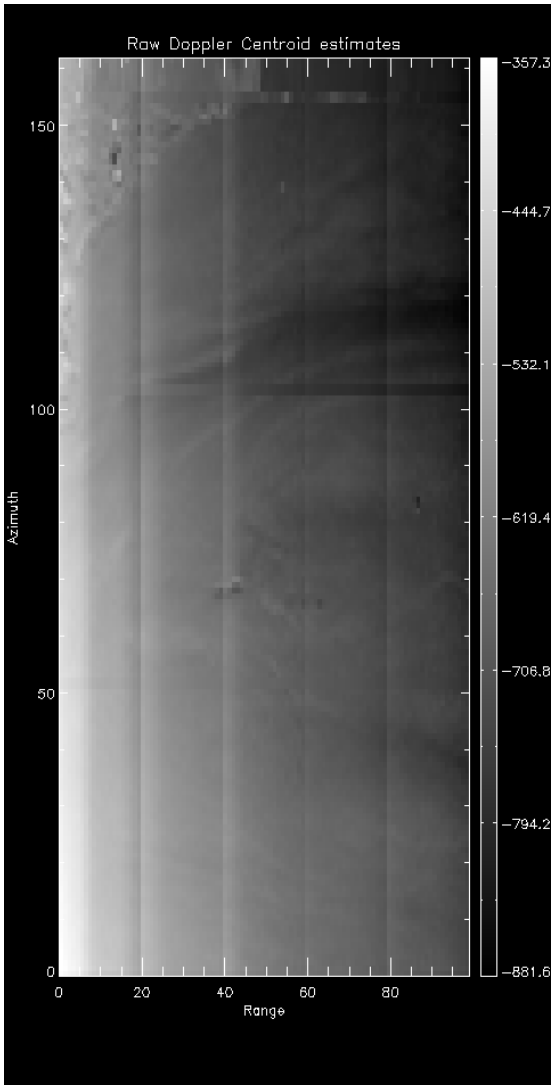

Figure 6: *Uncalibrated Doppler centroid estimates*

Given the orbital position, motion and pointing of the radar antenna relative to the Earth surface, one can estimate the expected Doppler Centroid variations along the orbit. The use of ESA CFI software libraries is very helpful for these type of geometrical calculations. A reference Doppler Centroid value can then be estimated for each single Doppler estimates and removed to obtain the so-called anomaly of Doppler centroid or Doppler shift as illustrated in Figure 7 a, b.

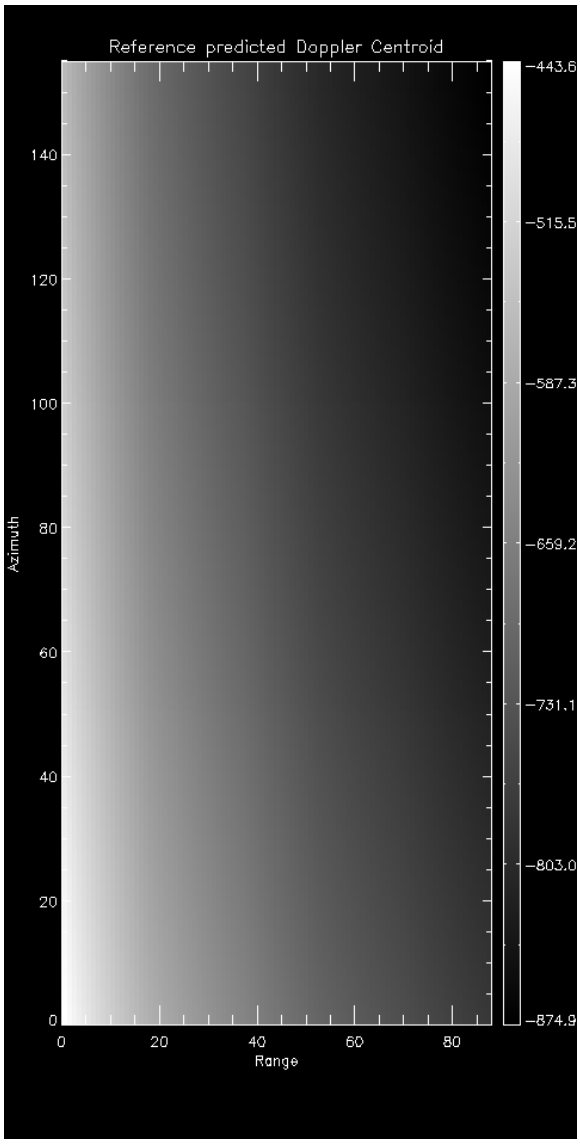

***Figure 7a**. Expected Doppler centroid grid*

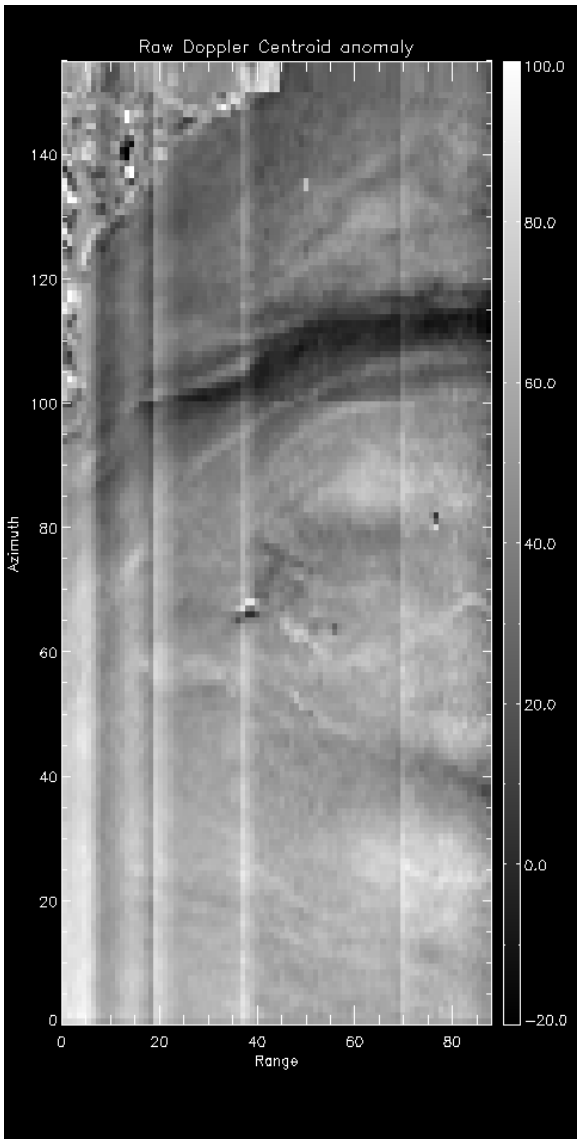

***Figure 7b**. Resulting Doppler centroid anomaly after removal of expected Doppler centroid*

Estimation and removal of range dependent instrumental bias. A Doppler estimator bias is observed along the range direction of the Doppler grid. However, except for some special cases this bias is found to be regular along the azimuth direction within one given product. However this observed bias do not seem to be stable in time as demonstrated on the analysis of 6 consecutive Doppler grids estimated from the same scene over the rain forest every 35 day Envisat cycle (see Figure 8). The same bias is illustrated for a Doppler grid over an ocean scene to illustrate its significance compared to the oceanic signal (Figure 9). Thus a simple first order correction consists in removing the average value along each azimuth line of the Doppler grid. Strictly speaking, this bias should only be estimated over the Doppler grid portions over land where we do not expect any mean Doppler shift bias. However, when no such land portions are available within the image, the same azimuthal average removal can be applied resulting in a Doppler grid that can only be further interpreted in the azimuth direction in terms of relative motions since the mean is arbitrary set to 0.

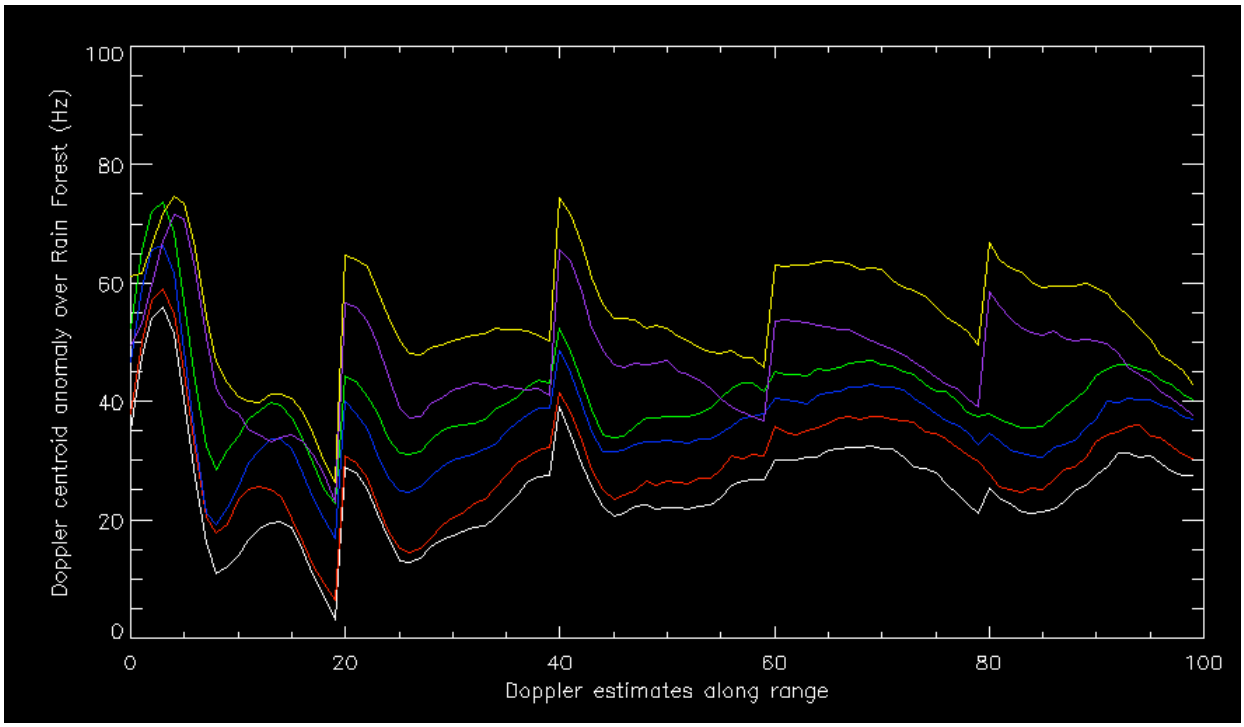

Figure 8. ASAR Wide swath Doppler grid averaged in the azimuth direction for six scenes over the same area of the rainforest. Each scene is plotted with a different colour. The Doppler grid has 100 estimates in the range direction (i.e., 20 per subswath). *The 6 acquisitions are the following:*
ASA_WSS_1PNDPA20050222_025842_000000622035_00003_15588_0092.N1;
ASA_WSS_1PNDPA20050329_025842_000000612036_00003_16089_0144.N1;
ASA_WSS_1PNDPA20050503_025850_000000622037_00003_16590_0090.N1;
ASA_WSS_1PNDPA20050607_025848_000000622038_00003_17091_0110.N1;
ASA_WSS_1PNDPA20051025_025847_000000612042_00003_19095_0089.N1;
ASA_WSS_1PNDPA20051129_025842_000000622043_00003_19596_0109.N1.

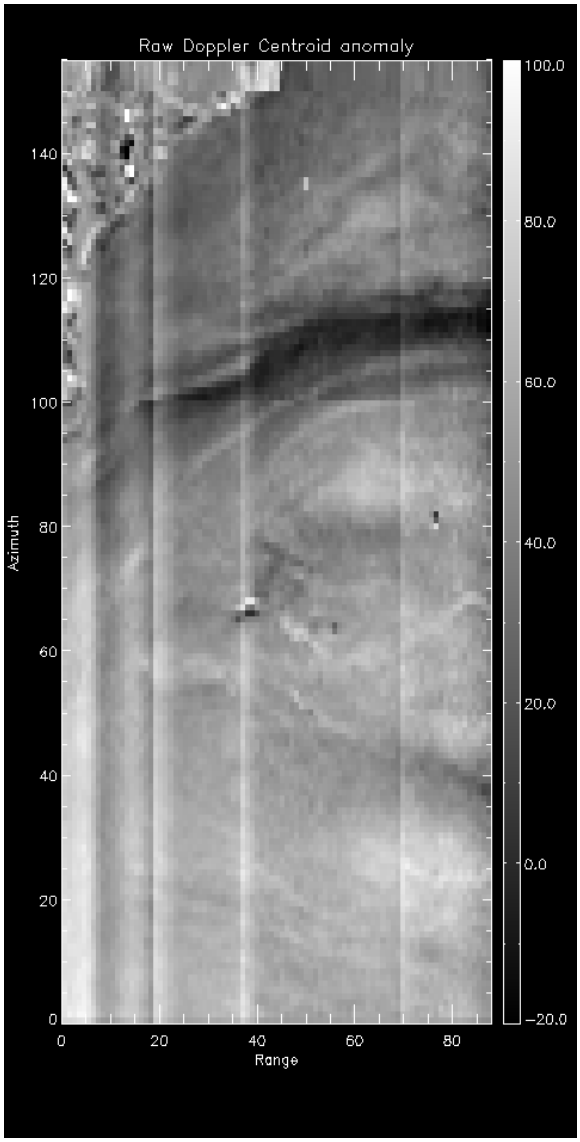

Figure 9a. *Before range bias filtering*

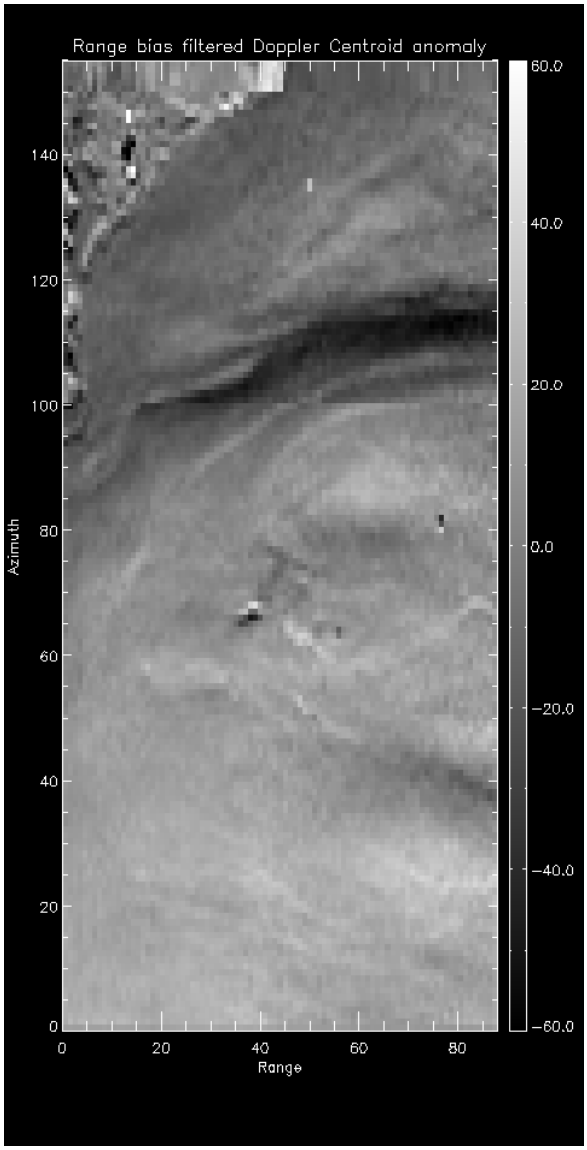

Figure 9b. *After range bias filtering*

Estimation and removal of bias caused by Azimuthal NRCS gradient. As for many Doppler centroid estimators used for SAR processing, a strong azimuthal gradient of NRCS will result in a asymmetric Doppler spectrum (uneven intensity at lower or higher radar azimuth look angle) and will inevitably cause a bias in the centroid frequency estimates. However, since the NRCS is also well known after range and azimuth focusing, it is possible to estimate this bias directly from focussed NRCS within the block used for each Doppler centroid estimate. This bias is becoming of dominant importance when the Doppler centroid estimates is done over small blocks in the azimuth direction (ie 12 bursts in this case) since the azimuthal radiometric gradient are not smoothed out anymore.

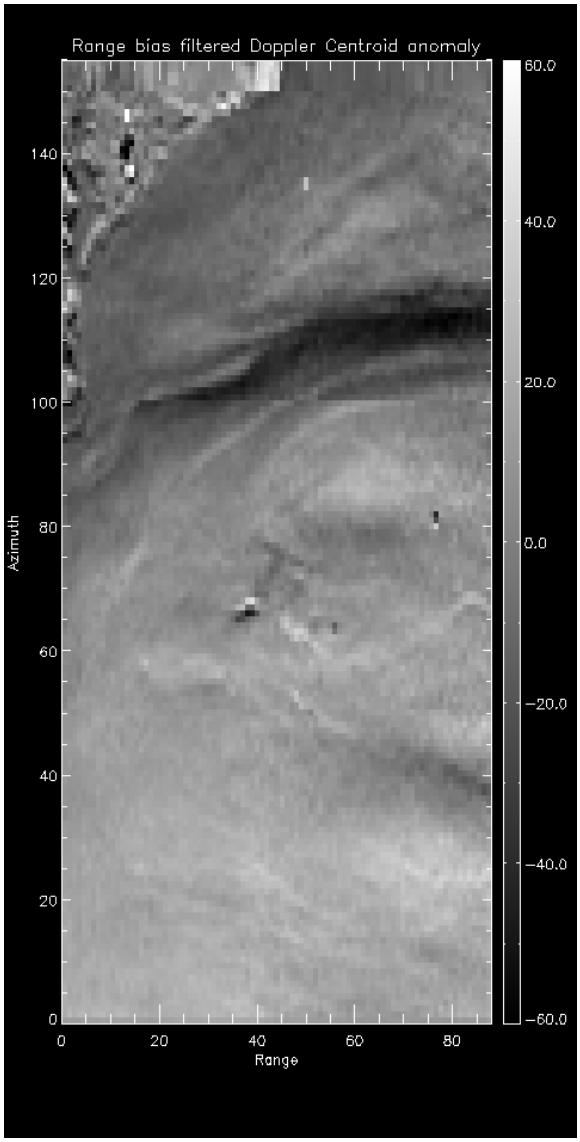

Figure 1a: *Doppler centroid anomaly before azimuthal radiometric gradient removal*

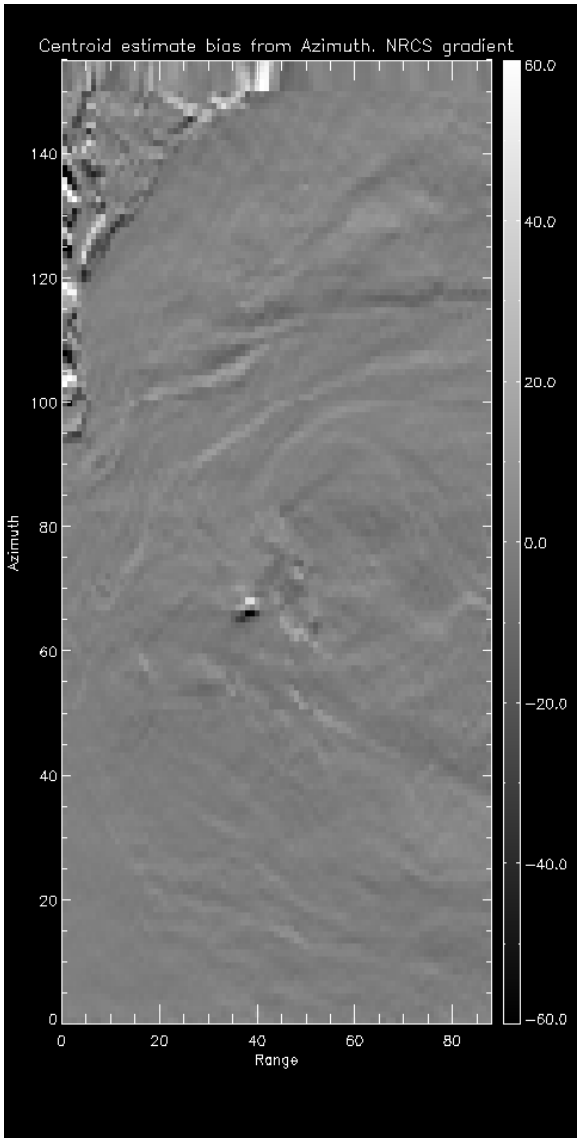

Figure 10b: *Expected Doppler centroid bias from observed azimuthal radiometric gradient on azimuthally focused NRCS.*

Sample ocean surface velocities observed over the Gulf stream current. A simple conversion of the resulting Doppler shift into a radial surface velocity and then to a horizontal surface velocity is giving a first glance at the potential use of such products for ocean current estimation as illustrated in Figure 11 a,b.

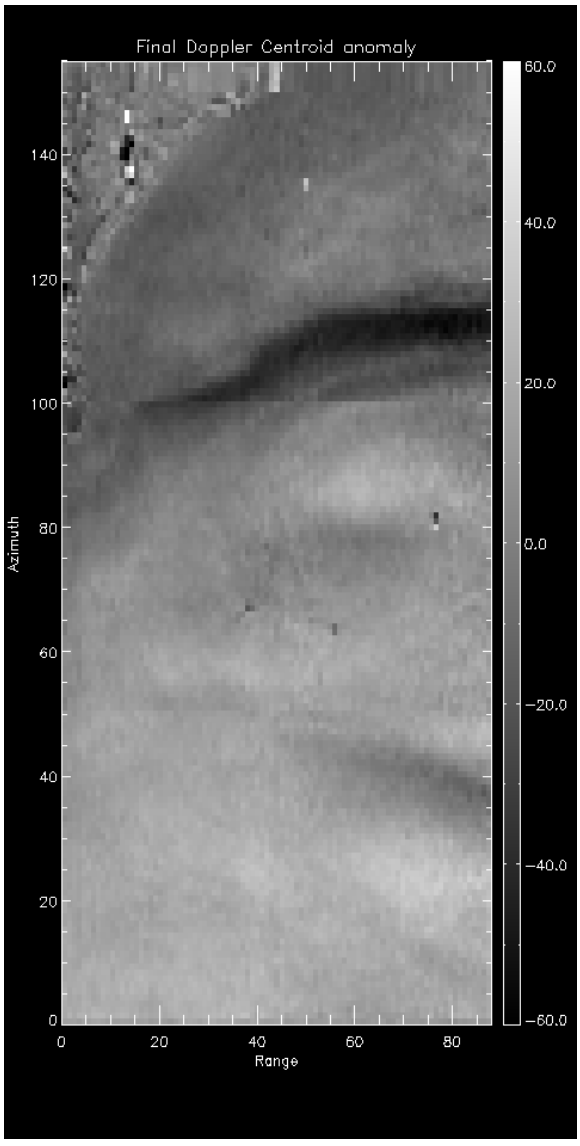

Figure 2a. *Doppler centroid anomaly after range and azimuth biases removed*

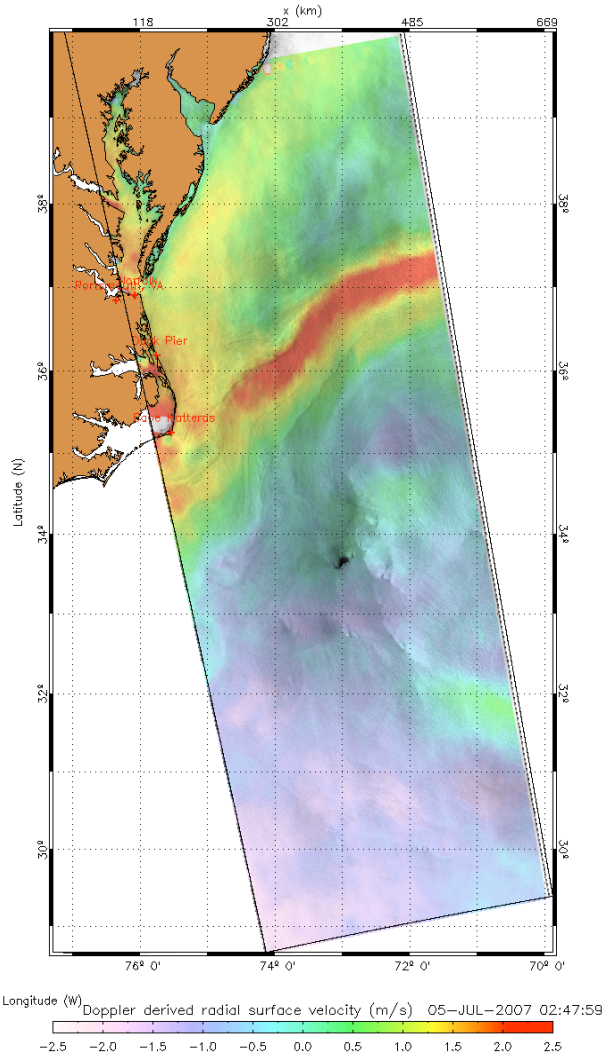

Figure 11 b: *Horizontal surface velocities as a direct transcription of the observed Doppler shift (without sea-state bias removal). Sea surface roughness in background.*

Applicability to existing scatterometers.

A Doppler calibration technique allowing retrieving the Geophysical Doppler from SAR I/Q data has previously been described. Such a technique could be applied to I/Q scatterometer data on condition that we are able to:

- Estimate the sensor attitude with a sufficient accuracy,
- Get the satellite orbital parameters (position, speed, acceleration)

First of all, an investigation of the existing scatterometers systems led us to the conclusion that not all scatterometer systems do provide datasets at a level required for investigation of the Doppler shifts. This is further elaborated below.

- **SASS-SEASAT** and **NSCAT** have been discarded since they make use of a bench of Doppler filters to discriminate the range location of the echoes (ref: DR47), which intrinsically brings an ambiguity between range and velocity and compromises the measurements over oceans.

- For **QUIKSCAT** Doppler filters are used on-board to cope with the large Doppler shift caused by the rotating antenna and to center the AD conversion on the effective signal frequency band. But the signal is then detected onboard and no complex data are or have been available on ground (personal communication Ernesto Rodrigez, NASA).

- For **ASCAT** the I/Q signal is not and have never been available on ground. The received echo signal is de-chirped onboard with an image of the transmitted pulse, filtered and down-converted to baseband. The baseband signal is sampled and processed by the onboard digital signal processor. The onboard processing is basically a power spectrum estimation (transformation to frequency domain and square modulus detection) followed by (spatial) low pass filtering. This results in echo power spectra, where each frequency corresponds to a specific slant range distance. Hence this range Doppler spectrum is ambiguous between target motion and range distance and cannot be used for our purpose. The echo power spectra are packed to nominal ASCAT source packets and transferred to the ground, where they serve as input data for the ASCAT ground processing (ref. DR37).

- For **OCEANSAT2** (where KNMI is officially co-PI of the cal-val activities) no access to data nor any information on data availability were available at the time. The system is a clone of QUIKSCAT. As such it is not anticipated that this system is able to provide useful data for this study.

- For **ERS-2** it appears that the scatterometer system is able to provide raw I/Q data continuously to the ground stations. The Doppler shift estimation on ERS-2 scatterometer data (described in ref. DR43) is used to estimate the yaw of the platform since the Gyros are out of order. The methodology used to estimate the Doppler shift is however not considered optimal. Even if the ERS-2 complex data are available and suitable for Doppler estimation, the large bandwith compared to the low PRF is anticipated to be a limiting factor to the precise estimation of Doppler shifts (a few Hz) required for surface current retrievals.

Whereas the ERS-2 orbit is known with sufficient accuracy, it is known (from ref: DR43) that due to gyroscopes malfunction, a new attitude and orbit control system is used on-board ERS-2 since the beginning of 2001. The new piloting mode of the spacecraft, termed zero-gyro mode (ZGM), does not use any of the gyroscopes. The remaining attitude sensors (a Digital Earth Sensor and a Digital Sun Sensor) are used to pilot the spacecraft. While the pitch and roll attitude angles have almost nominal values, the yaw angle can exhibit large variations around its nominal yaw-steering mode (YSM) value. A two stage compensation of the Doppler shift was initially designed to compensate (coarse compensation on-board and finer on-ground) for the shift introduced by a spacecraft in perfect YSM but now a significant part

of the spectrum of the received echo is shifted outside the bandpass of the on-ground low-pass filter. Without any correction, the received spectrum for the Fore and Aft beam would be completely out of the bandpass of the low pass filters (25KHz). The initial design relied heavily on the use of look-up tables that were pre-computed for a perfectly yaw-steered spacecraft. This is because compensation law is time dependent (orbit time and echo time) with coefficients provided by macro-commands. The coefficients are updated every 15 seconds according to (ref: DR53).

The ground processing chain has been modified (ref: DR43) to include an on-the-fly measurement of the yaw angle measurement of the residual Doppler shift yaw angle estimated from the received raw data by measuring the residual Doppler frequency shift. The mean Doppler frequency shift is measured by computing the best-fit of a Gaussian window onto the spectrum of the received echo. This estimate is more robust than the one based on the computation of the center of gravity of the spectrum, particularly when, due to the frequency shift, a major part of the spectrum is shifted outside the anti-aliasing filter bandwidth. This technique seems to be able to follow (along track) a residual Doppler shift of a few kHz with an error of few tens of Hz. In (ref. 53) the authors analyzed the Doppler shifts induced by yaw errors on the ERS-2 mid and Fore/Aft beams. As expected the mid beam is more sensitive to yaw errors. The residual shift is up to 30 Khz for the Mid beam and up to 20 Khz for the Fore/Aft beams. They make use of models (linear, second order) for the Doppler shift across track and estimate the model parameters via a minimum root square error fit of the residual Doppler frequency across track. They reach the conclusion that for a serious yaw error of 10 deg the error in the residual Doppler is up to 400 Hz in the case of second order model (3 parameters used for the fit).

Error budget and impact on surface current retrieval accuracy: In this error analyses aims at evaluating the impact of instrument and geophysical errors sources on the sea surface current radial velocity when extracted from the Doppler centroid measurement (f_{Dc}). Doppler centroid is defined as the radar return frequency shift at the antenna beam center. Therefore, Doppler centroid encompasses the signature of any displacement (whose radial component is non-null) of the observed scene relative to the antenna. The Doppler centroid anomaly (f_{Dca}) estimate is defined as the difference between the Doppler centroid measurement and the predicted Doppler shift arising from the relative velocity of the satellite (including the antenna) and rotating Earth (f_{Dp}).

$$f_{Dca} \equiv f_{Dc} - f_{Dp} \qquad \textit{(Eq. 1)}$$

If we assume an error-free f_{Dp} prediction and f_{Dca} estimate, then the Doppler shift anomaly can be directly attributed to geophysical displacements of the surface (whose radial component is non-null). This anomaly should be zero for a surface at rest with respect to the Earth. Hereafter, f_g stands for the geophysical contribution to the Doppler centroid. The sea surface radial velocity v_{rad} is related to the geophysical Doppler shift through the relation:

$$v_{\mathrm{rad}} = -\frac{\lambda_0}{2\sin\theta} f_g, \qquad \textit{(Eq. 2)}$$

where:

- λ_0 Is the radar wavelength,
- θ Is the radar incidence angle.

However, f_{Dp} prediction and f_{Dca} estimate can be polluted by errors. Also sea surface radial velocities can be due to other geophysical phenomena than sea surface current. Thus

$$\begin{cases} f_{Dca} \neq f_g \\ v_{\text{rad}}^{\text{current}} \neq v_{\text{rad}} \end{cases} \qquad \textit{(Eq. 3)}$$

A more general definition for the geophysical Doppler shift is:

$$f_g = f_{Dca} - f_{\text{err}}, \qquad \textit{(Eq. 4)}$$

where f_{err} accounts for errors of both f_{Dc} and f_{Dp}. Several reasons for errors exist **Error! Reference source not found.**]. Mis-pointing of the antenna (f_{Dp}) and non homogeneity of the radar intensity along the azimuth direction f_{Dc} are two of them.

It has been shown that the sea state is contributing significantly to the geophysical Doppler shift **Error! Reference source not found.**]. At first order, this contribution can be estimated, in average, by using surface wind vector information. In short, the relatively small scales in the sea state that are the steepest and the major contributors to the Doppler shift are generally in equilibrium with the surface wind. The sea surface radial velocity can thus be decomposed such as:

$$v_{\text{rad}} = v_{\text{rad}}^{\text{current}} + v_{\text{rad}}^{\text{wind}} + v_{\text{rad}}^{\otimes}, \qquad \textit{(Eq. 5)}$$

where $v_{\text{rad}}^{\text{current}}$, $v_{\text{rad}}^{\text{wind}}$ and $v_{\text{rad}}^{\otimes}$ respectively stand for the radial sea surface current, radial sea surface wind contributions and a cross term that encompasses any potential interactions between wind/waves/current. For now, sea state/surface current interactions that can be large in area of strongly varying surface current over short distances are neglected. We assume that, at a resolution of 5 km (such as ASAR Doppler grid), these rapidly varying surface currents are averaged out. In the case of scatterometers, this assumption remains valid as their resolution is coarser than 5 km. Therefore, a simplified relationship between radial sea surface current and sea surface radial velocity is:

$$v_{\text{rad}}^{\text{curr}} = v_{\text{rad}}(\theta, \lambda_0) - v_{\text{rad}}^{\text{wind}}(\theta, \phi_{\text{wind}}, \lambda_0, \text{pol}, \text{u}_{10}), \qquad \textit{(Eq. 6)}$$

where

- pol denotes the polarization of the radar antenna,
- Φ_{wind} is the azimuth direction of the wind relative to the radar antenna. $\Phi_{\text{wind}}=0°$ *(*resp. *180°)* when wind blows toward to (resp. away from) the antenna. It is called upwind (resp. downwind) configuration. $\Phi_{\text{wind}}=90°$ or *270°*when wind blows along the azimuth direction of the antenna: It is called crosswind configuration.
- u_{10} is the 10 m height wind speed.
- Φ_{curr} stands for the azimuth direction of the sea surface current relative to the radar antenna. Convention relative to the antenna is the same than for wind.

The sea surface current radial velocity is given by:

$$\begin{aligned} v_{\text{rad}}^{\text{current}} &= \left|\vec{v}_{\text{current}}\right| \cos\phi_{\text{current}} = \frac{\lambda_0}{2\sin\theta} f_{\text{current}} \\ &= \frac{\lambda_0}{2\sin\theta}\left(f_{\text{Dca}} - f_{\text{err}}\right) - \frac{\lambda_0}{2\sin\theta} f_{\text{wind}} \end{aligned} \qquad \textit{(Eq. 7)}$$

The sea surface wind contribution to the radial velocity has been studied by co-locating ASCAT wind vectors with ASAR geophysical Doppler shift in area free of strong current and a geophysical model function (GMF) CDOP **Error! Reference source not found.**] has been built for C-band such as:

$$f_{wind} = CDOP(\theta, \phi_{wind}, u_{10}, pol)$$

$$v_{rad}^{wind} = \frac{\lambda_0}{2\sin\theta} f_{wind} \qquad \textit{(Eq. 8)}$$

The use of this set of equations can give an idea on the sensitivity of sea surface current radial velocity measurements with respect to errors and measurements configuration. In previous equations, polarization, incidence angle and radar frequency are considered as unambiguous known quantities whereas the predicted Doppler shift (f_{Dp}), the Doppler centroid measurement (f_{Dca}) or the wind information (u_{10}, Φ_{wind}) can be erroneous.

Figure 12 presents a general view of what could be a situation of measurement for one single antenna. For clarity, the different angles involved in the equations are indicated.

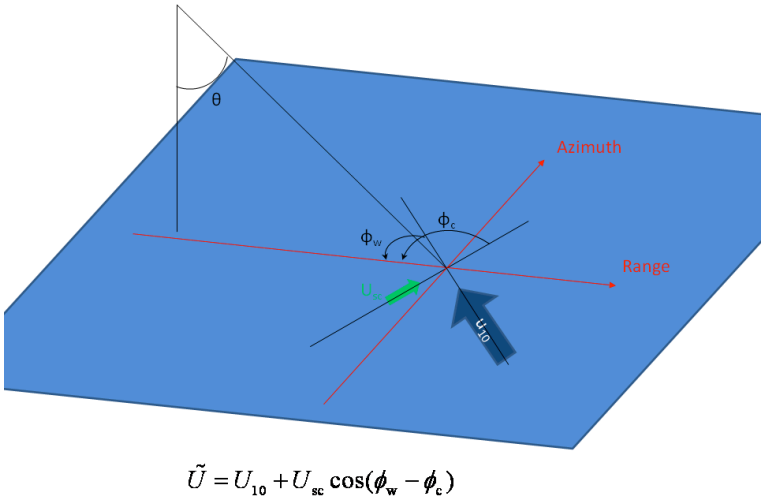

$$\tilde{U} = U_{10} + U_{sc}\cos(\phi_w - \phi_c)$$

Figure 12: *General configuration of measurement.* $\tilde{u}$ *is the wind speed relative to the ocean motion;* u_{sc} *is the sea surface current intensity;* u_{10} *is the wind speed relative to Earth.*

Radar configuration and non moving target Doppler shift prediction. The two main sources of error in the Doppler shift estimation are the Doppler shift estimator and the non moving predicted Doppler shift reference. The Doppler shift estimator error is dependent on the homogeneity of the scene but for a typical homogeneous scene over the ocean, the accuracy is about 5 Hz. The non moving predicted Doppler shift reference error is directly dependant of the knowledge of mechanical pointing and orbit but also to the electronic misspointing of the antenna boresight. Antenna boresight misspointing is a characteristic of active antenna arrays that may have drifting or failing TR modules that modify slightly the antenna pattern including fine directivity. This source of error is slowly moving and can be corrected using proper calibration methodology. However the mechanical pointing errors are random and bounded to the accuracy of the star trackers. For Envisat, an accuracy of 3 millidegrees in pointing resulting in an accuracy of about 10 Hz in terms of Doppler shift is achieved at best.

The use of CDOP GMF enables to investigate the relative importance of the wind contribution with respect to the incidence angle, polarization for a given sea surface current. In this sub-section, the errors contributing to f_{err} are considered as null. We consider several cases where the sea surface current intensities and the incidence angle vary. Eq (6) is used to estimate the Doppler shift with following values as input:

- $\lambda_0 = {}^{c}\!/_{f_0} = {}^{3e8}\!/_{5.255e9}\,\mathrm{m}$
- $\theta \in [16:1:42]\,\mathrm{degrees}$
- $|\vec{v}| = [0.1, 0.25, 0.5, 1.0, 2.0]\,\mathrm{m/s}.$

The Doppler shift induced is presented on Figure 13a as a function of incidence angle for several sea surface current intensities. For a given sea surface current direction, the Doppler shift increases with incidence angle and sea surface current intensity.

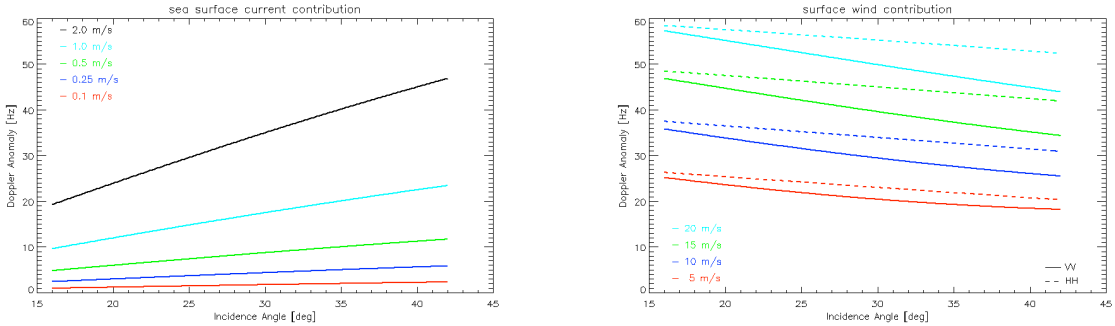

(a) (b)

Figure 13: *Doppler shift anomaly (Hz) a function of incidence angle (°) for several values of (a) sea surface current (Φ_{curr}=0°) and (b) wind speed (Φ_{wind}=0°). In the case of wind, where the polarization plays a role, results for VV are solid lines and while dashed lines represent HH results.*

Symmetrically to the sea surface current, we now consider several cases where the wind speed and incidence angle vary. Eq (7) is used to estimate the expected Doppler shift due to the sea state. The same configuration than in the previous simulation is used for the radar parameters. The wind values considered as input are:

- $|\overrightarrow{u_{10}}| = [5, 10, 15, 20]\,\mathrm{m/s},$
- Φ_{wind}=0°

Both VV and HH configuration are considered. The Doppler shift induced by the sea state is presented in Figure 13b as a function of incidence angle and wind speed. For a given wind direction, the Doppler shift increases with incidence angle and sea surface current intensity. For a given wind situation and incidence angle, the Doppler shift is larger in HH than in VV polarization. From 13 it can therefore be concluded that for a given wind speed, the larger the incidence angle, the larger the sea surface current signature in the Doppler shift. This is further exemplified in Figure 14a for a 7 m/s wind speed in upwind (Φ_{wind}=0°) and various intensity of current (Φ_{curr}=0°). For a 2 m/s current and large incidence angles, the relative contribution can reach up to 70% of the total Doppler anomaly. But this contribution falls below 50% for surface current lower than 1 m/s (no matter the incidence angle). This

indicates that the wind contribution has a major impact on the Doppler shift that cannot be neglected to retrieve absolute values of sea surface current radial velocity. It also indicates that VV polarization would be more adapted to reduce the importance of the wind in the Doppler shift. The same analysis can be done for several wind speeds (from 3 to 20 m/s, Φ_{wind}=0°) and a given magnitude of sea surface current ($|\vec{v}| = 0.25\,\text{m/s}$ and Φ_{curr}=0°). As observed in Figure 14b and c the relative impact of the sea surface current on the Doppler shift decrease when wind speed increases.

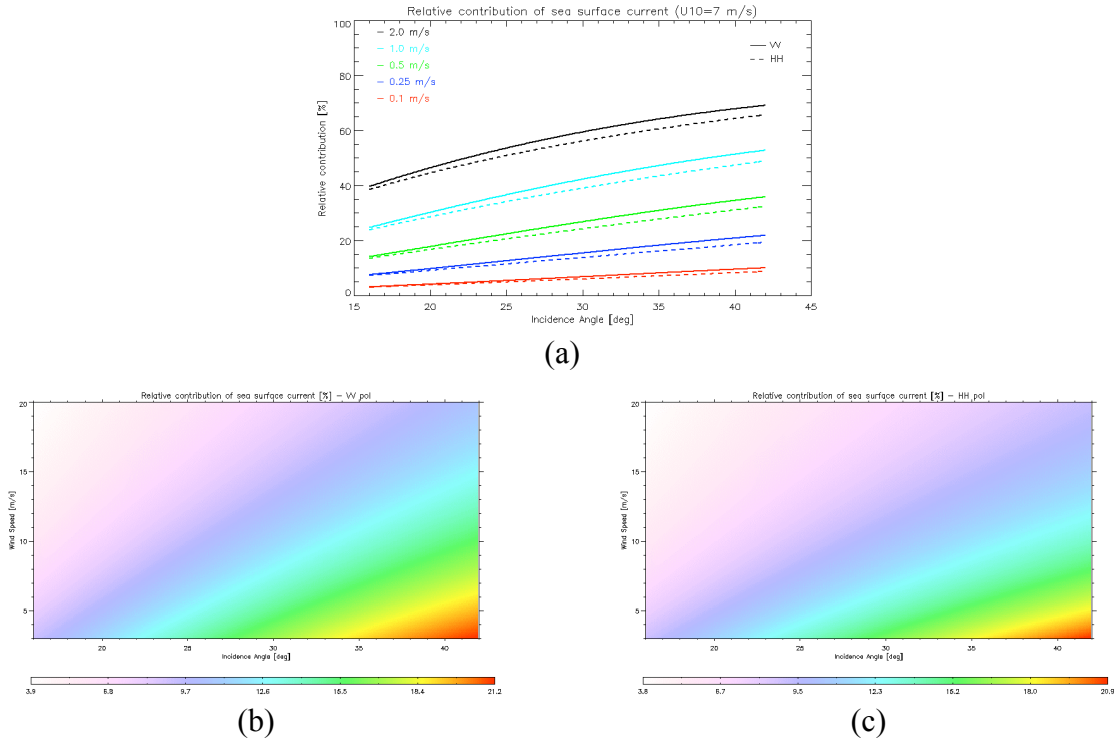

Figure 14: *(a) Relative contribution of the sea surface current as a function of incidence angle (degrees) with respect of polarization (VV is solid line and HH dashed line) and current intensity (color lines) for a 7 m/s wind speed (in upwind direction). (b) Same than (a) but only for VV and different wind speeds for a 25 cm/s sea surface current (Φcurr=0°). (c) Same than (b) but for HH polarization.*

From this analyses the following achievements and findings have been obtained:

- ✓ It appears that the sea state is the major contribution to the geophysical Doppler anomaly. Therefore particular attention has to be paid to take into account properly.
- ✓ The sea state impact is enhanced at HH polarization. VV polarization should be considered in priority to increase the relative impact of the sea surface current on the signal. In addition one could envisage a dual polarization system. Indeed as the signature of the sea surface movement on the Doppler shift is non polarization dependent, a combination of the polarization could be used to get directly the sea state contribution free of current signature. One could then remove the estimated sea state contribution to get the sea surface current.
- ✓ The relative impact of the sea surface current in the geophysical Doppler shift increases with incidence angles. Therefore, the use of larger incidence angles is recommended to decrease the sea state contribution to the geophysical Doppler shift.

The uncertainties in the radial sea surface current velocities estimates can be due to the estimates of the Doppler centroid anomaly (term 1 in Eq. (6)) or the sea state contribution (term 2 in Eq. (6)). The impact of various errors in these two terms for sea surface current radial velocity retrieval from Doppler centroid. Only (VV polarization which seems the most favorable radar configuration) is further considered below.

Doppler centroid estimate and non-geophysical errors. Here we assume that the non-geophysical term in Eq. (7) can introduce errors up to 15 Hz due to an imprecise estimate of f_{Dca}, prediction of f_{Dp}. These errors are assumed to be not taken into account. In the contrary, the sea state effect is assumed perfectly accounted for. The Error on the radial sea surface current induced by the non-geophysical term is:

$$E_1 = \frac{\lambda_0}{2\sin\theta} f_{\text{err}} \qquad \textit{Eq. 9}$$

Error on sea surface current radial velocity is calculated on as a function of f_{err} and θ. Results are presented in Figure 15. For a given error f_{err}, E_1 decreases when incidence angle increases. E_1 can reach values up to 1 m/s for the lower incidence angles and non-geophysical errors greater than 10 Hz.

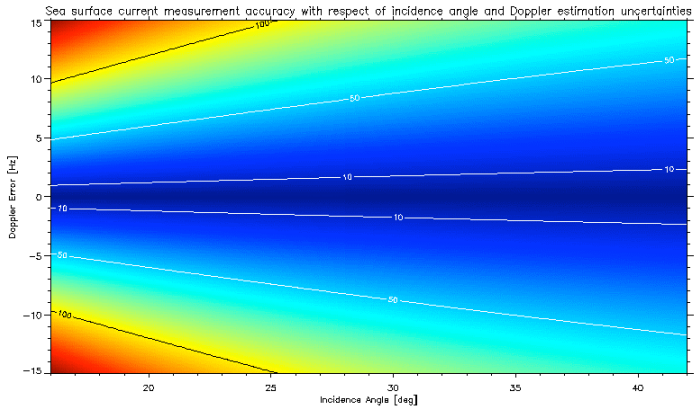

Figure 15: *simulation of Error in cm/s on the sea surface current radial velocity induced by a error in Hz on the Doppler shift anomaly. Impact of this error is presented as a function of incidence angle (x-axis) and Doppler shift error (y-axis).*

Sea state errors. The Doppler shift due to the sea state f_{wind} is given by Eq. (7), where the surface wind vector is assumed to be known. In practice, the information about the wind vector can be erroneous due to a error on wind direction and/or speed. The error on the term 2 is:

$$E_2 = \frac{\lambda_0}{2\sin\theta}\left|\text{CDOP}(\theta,\phi,\text{u}_{10},\text{pol}) - \text{CDOP}(\theta,\phi \pm \Delta\phi,\text{u}_{10} \pm \Delta\text{u}_{10},\text{pol})\right|, \qquad \textit{Eq. 10}$$

where Δu_{10} and $\Delta\phi$ respectively stand for the error on wind speed and direction. To get the required wind vector information for the sea state correction, there is at least two options:

(i) use on ancillary data from an atmospheric model,

(ii) use the scatterometer wind inversion scheme.

Using data from atmospheric model we investigate the general case with errors on wind speed and direction for several incidence angles. The expected errors are calculated as follows:

- Impact of the wind speed: We consider a 7 m/s wind speed in upwind configuration and use it as input of CDOP to get the reference Doppler shift induced by the "true wind" with respect to incidence angle. This reference is then compared to Doppler shift values obtained by introducing error in the wind input: $\Delta u_{10} = [-2:0.1:2]$ m/s and $\Delta\Phi = 0$ degree. Results are presented in Figure 16a.
- Impact of the wind direction: We consider a 7 m/s wind speed in upwind configuration and use it as input of CDOP to get the reference Doppler shift induced by the "true wind" with respect to incidence angle. This reference is then compared to Doppler shift values obtained by introducing error in the wind input: $\Delta u_{10} = 0$ m/s and $\Delta\Phi = [-90:1:90]$ degrees. Results are presented in Figure 16b.

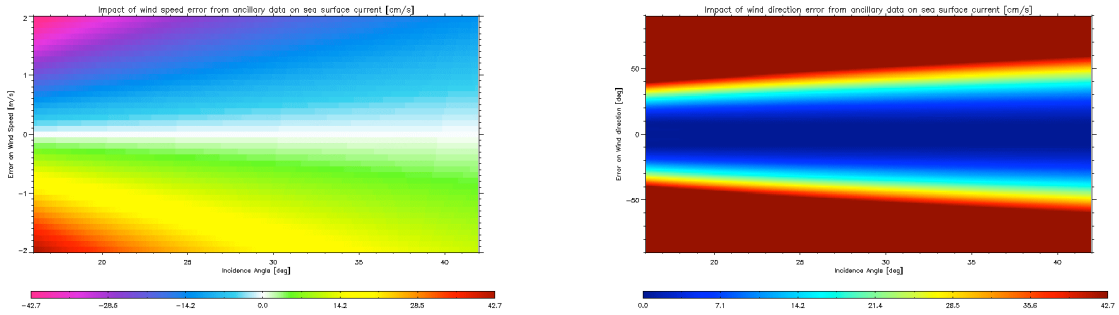

(a) (b)

Figure 16: *Simulation of wind induced errors in cm/s on sea surface current radial velocity using reference wind blowing in an upwind configuration at 7 m/s. Wind errors are caused by inaccuracies in the wind speeds or directions used to correct f_{Dca} from the sea state effect. Panel (a) shows the simulated surface radial velocity error in cm/s (colorbar) as a function of incidence angle (x-axis, in degrees) and wind speed error (y-axis, in m/s) between erroneous and correct winds. Panel (b) shows the simulated surface radial velocity errors in cm/s (colorbar) as a function of incidence angle (x-axis in degrees) and direction difference (y-axis, in degrees)).*

In general, we can conclude that the impact of any error on the wind vector increases with decreasing incidence angle. It was expected. Indeed, from our previous simulations (see Figure 13), we know that for a given sea state, the relative contribution f_{wind} increases with incidence angle. Typically for an error of 1 m/s in the wind speed, the error in the sea surface current radial velocity ranges from 6 cm/s at 42 degrees to 22 cm/s at 16 degrees. For a 2 m/s error in the wind speed, the error on the sea surface current radial velocity ranges from 11 cm/s at 42 degrees to 43 cm/s at 16 degrees. In comparison, for errors in the wind direction larger than 45 degrees we observe that errors on the sea surface current radial velocity are larger than 50 cm/s dropping to around 20 cm/s for incidence angles of 16 and 42 degrees.

Instead of using wind information given by a numerical weather prediction model, the other option would be to use the wind directly retrieved from the scatterometer. In this case, the uncertainties of the scatterometer winds and its impacts on the sea surface current radial velocity estimate have to be addressed. The wind speed, when related to the backscattered signal through standard geophysical model functions such as CMOD (ref.41) cannot be

considered as an absolute speed relative to the Earth (in the contrary of buoy measurements) but as a speed relative to the ocean surface motion. Nevertheless, the wind input required to properly take into account the sea state effect on the geophysical anomaly is the absolute speed relative to the Earth (ref. DR15). In order to investigate the impact of using a non-absolute wind speed relative to Earth on the sea surface current radial velocity estimate, we consider 3 different situations of sea surface current speed (0.5, 1 and 2 m/s). All possible orientations of the current with respect to the antenna are considered. The absolute wind is characterized by a 7 m/s speed and the relative wind speed is given by equation:

$$\tilde{U} = U_{10} - U_{sc}\cos(\phi_w - \phi_c) \qquad \textbf{\textit{Eq. 11}}$$

When the wind and the current are aligned in the same direction, then $\tilde{u} < u_{10}$. When the wind and the current are aligned in the same direction, then $\tilde{u} > u_{10}$. This relationship implies a symmetric behavior for $\tilde{u}$ with respect to $\phi_w - \phi_c$ and a null impact of current on the sea state correction when sea surface current and wind are perpendicular. In practice for the same sea surface current and wind intensity, the rates of attenuation and generation of sea surface waves are not expected to be symmetrical with respect of $\phi_w - \phi_c$. Thus the use of relationship (Eq. 10) is a simplification of the problem. A physically based approach taking into account sea surface current interaction with waves could be used to refine the approach and to take into account these effects. This is further illustrated in Figure 17. When $\tilde{u} > u_{10}$ (resp. $\tilde{u} < u_{10}$), the sea state effect is overestimated (resp. underestimated) and the Doppler shift attributed to the sea surface current underestimated (resp. overestimated). The impact of this error decreases when incidence angle increase and when $\phi_w - \phi_c \to 90°$. If the wind departs from the upwind direction then the impact of this error decreases. In case of 2 m/s sea surface current, the error on the wind can induce error on the sea surface current radial velocity up to 40 cm/s for the lowest incidence angles.

In summary we find that:

- ✓ An error of 1 m/s on the wind speed used as input for the sea state correction lead to an error around 20 cm/s at low incidence angle (16°) and around 5 cm/s for large incidence angles.
- ✓ An error of 45 degrees for the wind direction as input for the sea state correction lead to an error larger than 50 cm/s at low incidence angle (16°) and around 20 cm/s for large incidence angles.
- ✓ The impact of the sea state errors increases with decreasing incidence angle and are more pronounced in HH polarization.

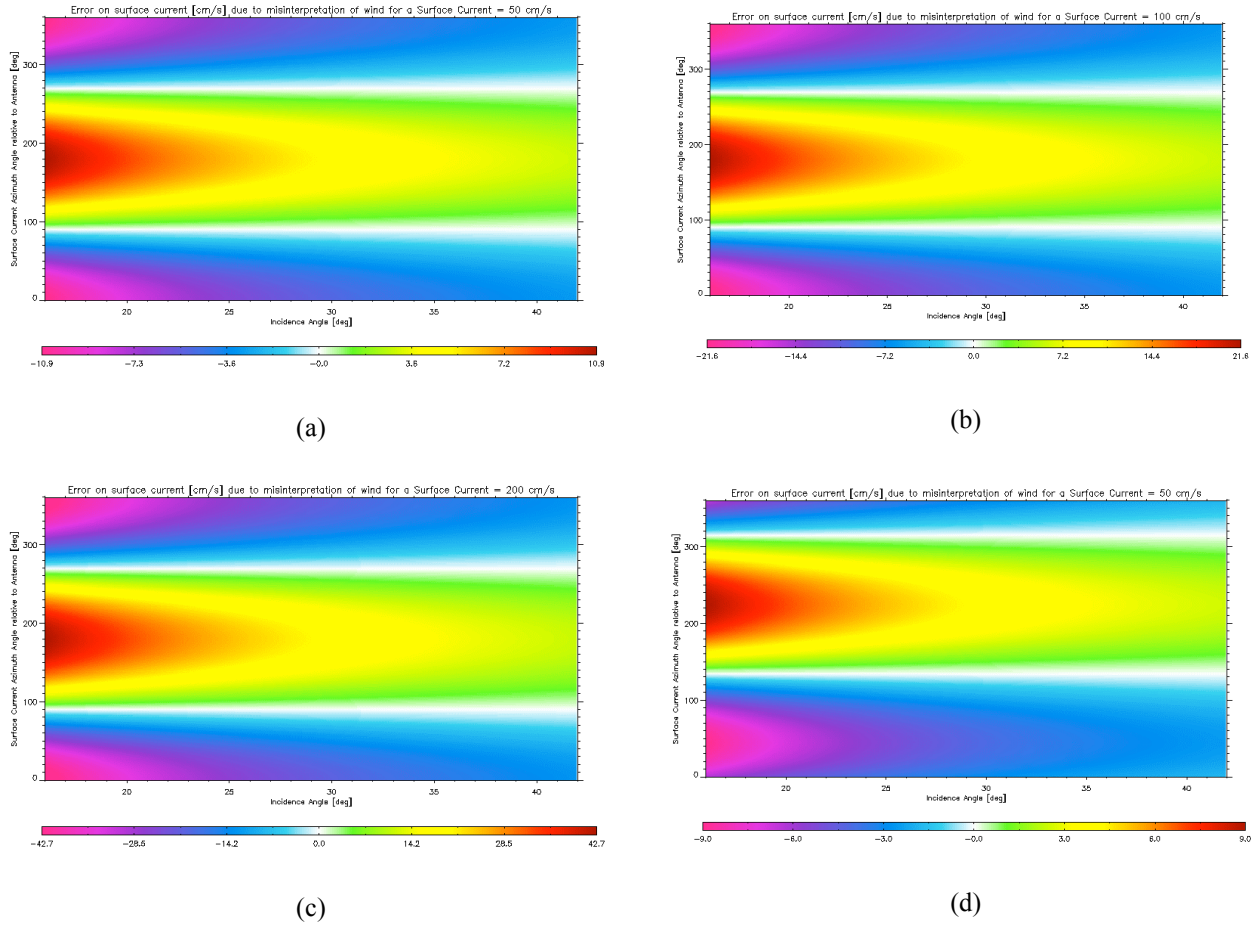

***Figure 17**: Errors (in cm/s) on sea surface current radial velocity when the input wind for the sea state correction is the relative wind speed $\tilde{u}$ instead of the absolute wind speed u_{10} as a function of incidence angle (x-axis in degrees) and azimuth angle between sea surface current and antenna directions (y-axis in degress). When $y = 0$, it means that antenna and current are aligned with current going toward the antenna. For panels (a-c), the wind azimuth angle is upwind meaning that $y = \phi_w - \phi_c$. Panel (a): Sea surface current is 0.5 m/s and wind azimuth angle is upwind. Panel (b): Sea Surface current is 1 m/s and wind azimuth angle is upwind. Panel (c): Sea surface current is 2 m/s and wind azimuth angle is upwind. Panel (d): Sea surface current is 0.5 m/s and wind azimuth angle is 45°. When $y = 45° \Leftrightarrow \phi_w - \phi_c = 0°; y = 225° \Leftrightarrow \phi_w - \phi_c = 180°$ and $y = 135° \Leftrightarrow \phi_w - \phi_c = 90°; y = 315° \Leftrightarrow \phi_w - \phi_c = 270°$.*

TASK 2000: Analyses of the adequacy of the existing scatterometer data for surface current estimation
SUB-TASK 2100 - ANALYSES OF THE ERS-2 AND KUROS SCATTEROMETER SYSTEMS
SUB-TASK 2200 - ANALYSES OF DATA AVAILABILITY AND SELECTION OF DATA

No KUROS data was available for this study. The wind retrieval in current scatterometry is based on combining measured backscatter signals (normalized radar cross sections, NRCS also called sigma0) and empirical model functions describing the expected backscatter signals (Geophysical Model Function, GMF).

These GMF functions are gradually improved as more scatterometer instruments and data become available over the years. GMF functions are unique and differ for different wavelengths and different polarization combinations of transmitted and received signal. The currently most popular scatterometer polarization options are vertical-transmit vertical-receive (VV) and horizontal transmit and horizontal-receive (HH), while cross-polarization GMFs, VH or HV, are being experimented on Synthetic Aperture Radar (SAR) systems [RD7].

The current GMF version for C-band VV (ASCAT) used at KNMI is CMOD5N [RD1, RD2], and for Ku-band VV and HH (OSCAT, HY2A) NSCAT-3 [RD3]. At incidence angles between 20 and 70 degrees, these functions follow a quasi-linear wind speed dependence and basically a double-harmonic wind direction dependence.

To exploit these basic wind vector sensitivies, typical scatterometer instruments implement several incidence and azimuth looking angles (see Figures 18 and 19 for examples).

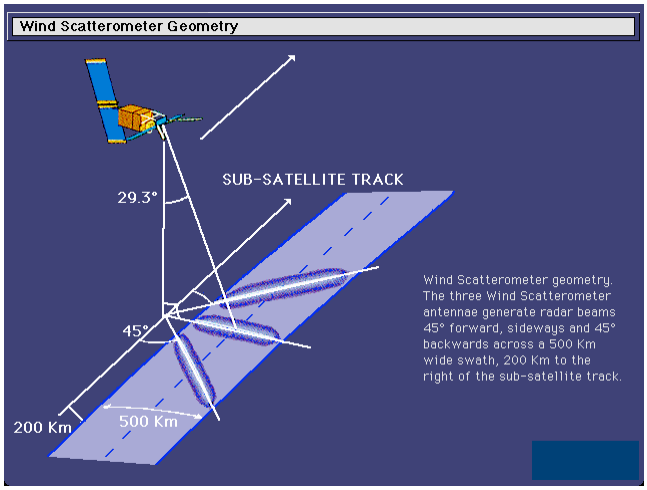

***Figure 38**: example geometry for ERS taken from ESA website*

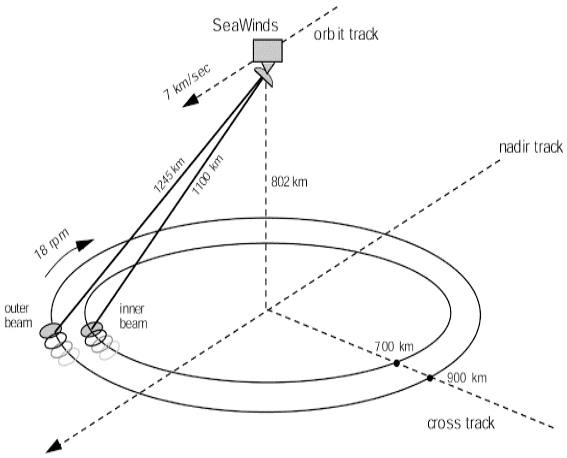

***Figure 19**. example geometry for Quikscat, taken from NSIDC website*

Bayes' theorem states that the probability of states x and y are related as follows:

$$P(x \mid y)P(y) = P(y \mid x)P(x) \qquad \text{(eq. 1.1)}$$

where and $P(y)$ is the prior probability of y and $P(x \mid y)$ the posterior probability of state x for given state y. In retrieval problems x is usually related to some unknown information (state)

that may be obtained from a measurement y. In estimating x, the measurement y is given and the prior $P(y)$ irrelevant, such that:

$$P(x \mid y) \propto P(y \mid x)P(x) \qquad \text{(eq. 1.2)}$$

In case of a normal noise distribution and a known state x, the measurements would be distributed as:

$$P(y \mid x) \propto \exp(-\frac{(y-x)^2}{2\sigma^2}) \qquad \text{(eq. 1.3)}$$

So, for convenience a cost function J may then be defined as:

$$J(x) = -2\ln[P(x \mid y) + P(x)] = \frac{(y-x)^2}{\sigma^2} - 2\ln[P(x)] + c \qquad \text{(eq. 1.4)}$$

The x for which J is minimum represents its most likely state. Usually, the distribution $P(x)$ is much broader than the distribution $P(x \mid y)$ and the domain of x infinite. In such case the prior $P(x)$ may be assumed constant in the retrieval problem, as while x is varied the value $P(x)$ would not change much. It is clear that the constant c does not contribute to the minimization of J. So, when all states x are a priori equally likely, *P(x)* is constant and only the quadratic term remains. We may then use a simplified equation for the retrieval:

$$J(x) = \frac{(y-x)^2}{\sigma^2} \qquad \text{(eq. 1.5)}$$

It is now easy to see that if we have one measurement y to estimate the most likely state x, the minimum J will be obtained for $x = y$. Note that the noise in y is than projected directly onto the retrieved quantity x. As more measurements become available, additional terms may be added to J and the noise contribution to x will be minimized by minimizing J. The simplified equation is traditionally used to construct a maximum likelihood estimator (MLE) function:

$$MLE(w,\phi) = \frac{1}{\langle MLE \rangle} \sum_{i=1}^{N} \frac{\left[\sigma_i^0 - \sigma_{GMF,i}^0(w,\phi)\right]}{\mathrm{var}(\sigma_i^0)} \qquad \text{(eq. 1.6)}$$

in which ω is the wind speed in m/s, ϕ the relative wind direction between the wind vector and the antenna look angle (azimuth) in degrees, σ_i^0 the measured NRCS for antenna i, and $\sigma_{GMF,i}^0(w,\varphi)$ the NRCS following from the GMF for a given wind speed, wind direction and antenna geometry. Note that this may be a different function for each beam in the MLE calculation, depending on wave length, and polarization.

The variance in σ_t^0 may be used as a weight in the summation and is related to the often used κ_p relative noise number using:

$$Kp^2 = \mathrm{var}\left(\sigma^0\right) / \left(\sigma^0\right)^2$$

Note that using κ_p in the denominator has the consequence that a larger estimated backscatter reduces *J*, i.e., the wind estimation becomes non linear and in fact biased. Some scatterometers (e.g., ASCAT) provide a reasonable estimate of the measured backscatter variance, in which case the denominator is determined a priori and the retrieval function linear. Figure 20 shows the MLE as defined in Eq. 1.6 for one, two and three contributing NRCS measurements.

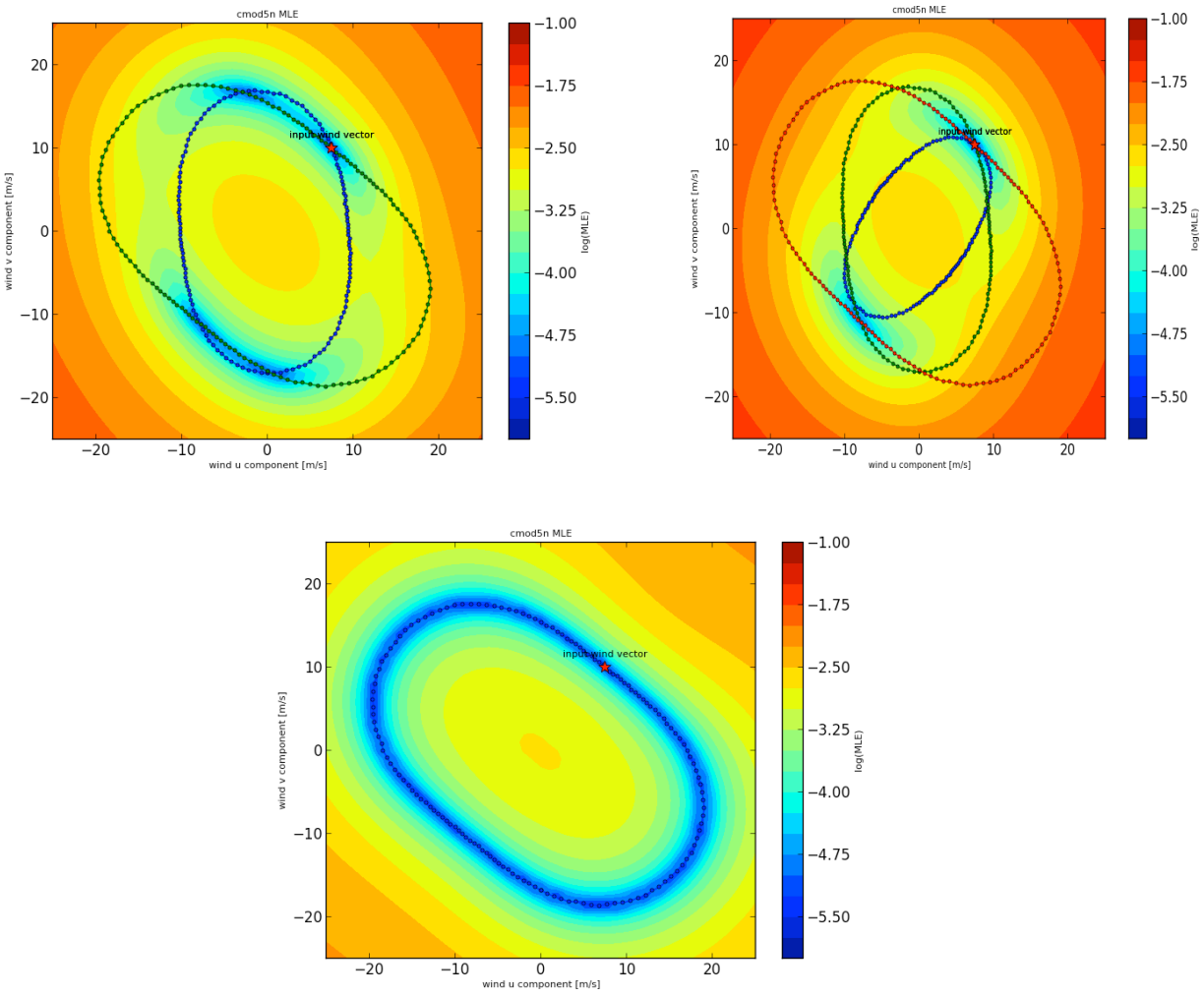

Figure 20: *MLE based on CMOD5N for 1 antenna, 2 antennas and 3 antennas*

Stoffelen noted in [RD8] that the double harmonic dependence of the C-band VV GMF is not perfect, which causes a variable wind vector sensitivity of the retrieval function to the ASCAT measured backscatter triplets. This leads to unwanted peaks and troughs in the retrieved wind direction distribution. Following the Bayes retrieval formalism above, this means that the prior expectation of wind direction $P(x=\phi)$ is not uniform. It turns out that the term $P(x)$ is more important than the noise term $P(y|x)$ in this case. By transforming the measurement space, such that the wind vector sensitivity becomes locally constant and thus $P(\phi)$ may be assumed constant, the ASCAT wind retrieval becomes approximately linear and provides a more uniform wind direction response.

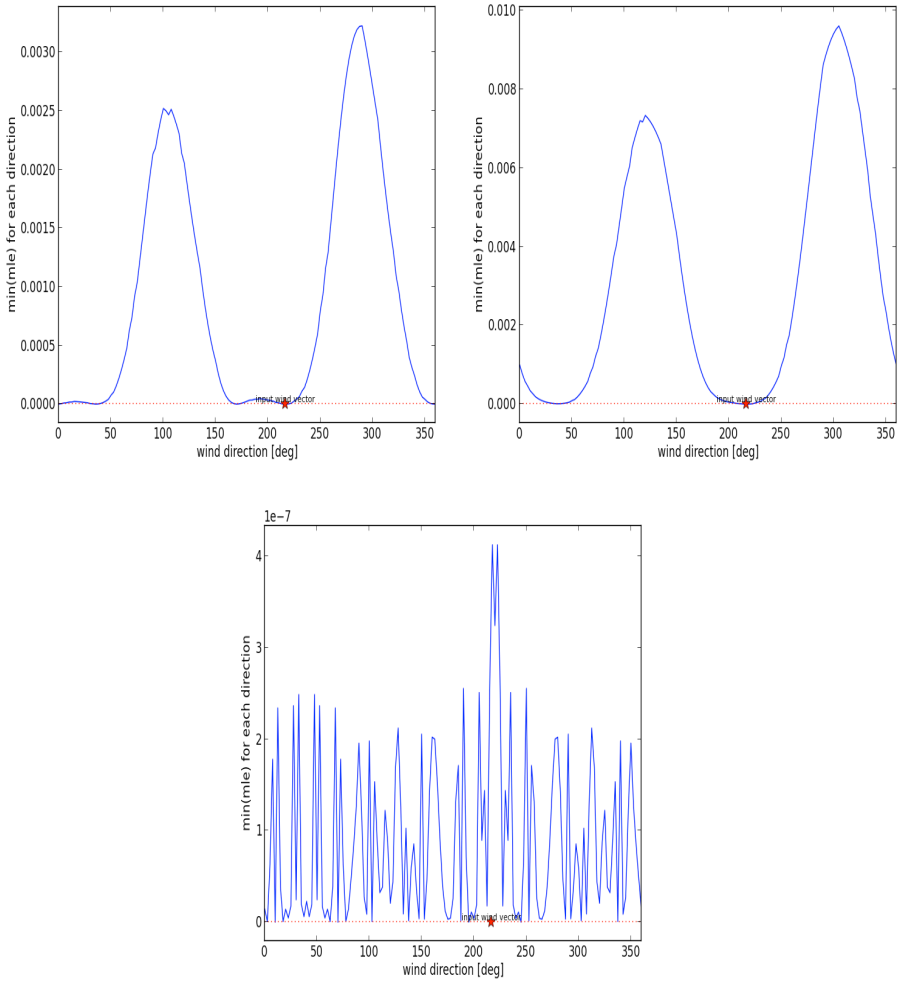

Figure 21: *minimum MLE as function of wind speed, based on CMOD5N, for a simple noiseless simulation case for 1 antenna, 2 antennas and 3 antennas*

Based on the quasi-linear speed dependence of the GMF function an efficient search algorithm is applied to find local MLE minima which represent possible wind vector solutions that would give NRCS signals as close to the measured NRCS as possible (given the constraints imposed by the GMF function). This search algorithm loops over wind directions in steps of 2.5 degree (144 steps) and determines a wind speed that gives a minimum MLE value for that wind direction. For the next direction step the previous result is used as first

guess which makes the search much more efficient. The result is a table of wind speeds giving the local MLE minimum for each wind direction (see Figure 21).

At certain combinations of wind direction and across-track Wind Vector Cell (WVC) rotating pencil-beam scatterometers like HY2A, OSCAT, and previously for QuikScat, are insensitive to the wind vector [RD8]. Following Eq. 1.6 this means that the MLE derivative will be zero and either MLE maxima or minima occur at these positions, irrespective of the real local wind. Portabella shows in [RD9] that the 144 solutions may be used to represent the full wind observation probability density function $p(w,\phi|\sigma^0)$ in data assimilation, maintaining its full statistical properties, including skewness or broadnening of its extremes. So all 144 solutions can be presented as possible wind results to the ambiguity removal algorithm, which mixes the result with prior knowledge of a short range NWP model wind field and its spatial error structure and selects the most likely solution [RD9, RD10]. This is the current method for wind retrieval applied at KNMI for rotating pencil-beam scatterometers.

For more regular and linear retrieval problems, such as for the ASCAT and ERS scatterometers, an additional step is to search along the "valley" of 144 minima to find local minima in MLE. Only the 4 deepest local minima are reported in most cases [RD11]. These are passed on to an ambiguity removal algorithm as mentioned above to determine the posterior most likely wind vector, which in turn is reported as observed wind vector. Examples for 1, 2 and 3 beam systems are given in Figure 21. Note that a system with only one antenna (left plot, similar to the usual SAR systems) finds zero MLE for all wind directions, and only constrains the wind speed for a given wind direction or vice versa [RD9]. The jumping lines here are caused by numerical rounding errors in the minimum search routine and have no physical significance.

[RD11] investigated spurious ASCAT and ERS local minima under certain conditions near the peaks of the MLE function in Figure 21 (3 antenna case) with high MLE and therefore extremely low probability. AWDP has been modified to reject such solutions, but this version has not bee used here.

Applying ambiguity removal implies mixing the quality of the scatterometer measurement with the quality of the NWP model. To study performance of a new system like Dopscat the characteristics of the (prior) NWP forecast quality can be taken into account locally rather than through a full-blown 2DVAR. Within this study techniques have been chosen to avoid use of the ambiguity removal using NWP data, such as selecting the solution with a direction closest to the input vector of a simulation, or the more elaborate FOM method (as discussed in section 0). Ambiguity removal is locally (on WVC basis) implemented in a simplified manner.

A new pair of GMF functions describing the expected Doppler shift in [Hz] for a given wind speed, wind direction and instrument geometry and polarization was provided by CLS [RD6]. These where determined by applying a neural network fitting procedure to a SAR test data set [RD13]. A few concerns remain with the derivation of these initial GMFs, notably:

1. CDOP has been derived for ~5-8 km pixel ASAR and 6-hourly ECMWF collocations; the spatial and temporal collocation specification; spatial and temporal collocation distance and representation with respect to ASCAT may be improved, where small improvement is expected; [RD12] collocated the 25-km ASCAT and ERS products and found 0.5 m/s wind component differences around the diagonal, i.e., very good

correspondence; On the other hand, the spatial representation error of local (buoy) winds for a 25-km ASCAT WVC is about 1 m/s; in addition, ECMWF fields lack about 1 m/s variability in the wind components as compared to ASCAT 25-km WVCs [RD10]; therefore, after aggregation of ASAR data on ASCAT scales, less noise will appear in the ECMWF collocation data set used for CDOP derivation; also, ECMWF winds may be time interpolated to improve quality;

2. [RD14] contains the derivation of the CMOD4 GMF, which chapter suggests several considerations on the GMF "learning" cost function; non-linear parameters, relative noise specifications, sampling of the fitting domain and noise are all addressed; for example, wind direction sampling at the higher winds can be rather irregular and non-uniform and this may seriously bias the GMF estimation; these considerations should also be applied to the CDOP GMF derivations as they have proven to be successful; in addition, lower noise by improved spatio-temporal collocation (see 1.) would reduce these fitting errors;
3. The CDOP GMF derivation may be extended with statistical analyses against ASCAT QC parameters, flags and perhaps interpolated ECMWF winds, ASAR incidence angle and polarization in order to better understand the overall statistical residuals;
4. The derived GMFs should make physical sense in terms of speed dependency and upwind and crosswind wind direction symmetries;

However, for this study, we assume these preliminary functions to be correct, and ignore the possibility that they contain fitting or conceptual errors. The signals based on these Doppler GMF's have been added to the wind inversion software in a similar way as the other antenna back scatter signals, i.e. the square of the difference between measured and predicted value has been added to the summation in the MLE definition in eq. 1.6. Example figures for MLE based on a single Doppler signal from one antenna are given in Figures 22 and 23.

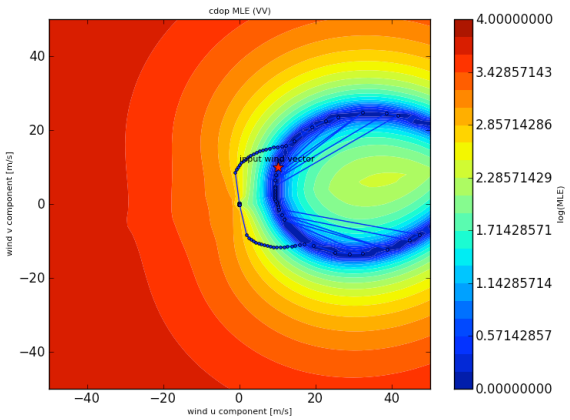

***Figure 22**: MLE based on CDOP VV*

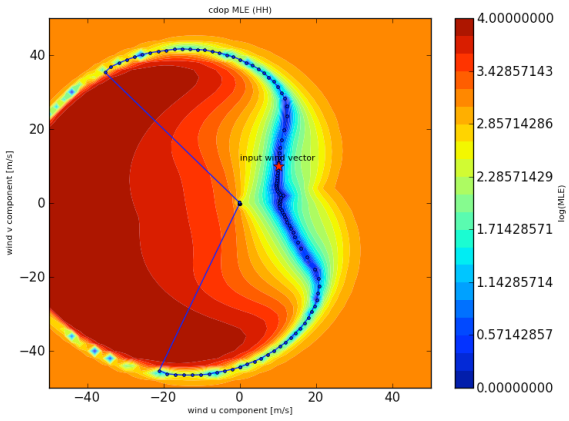

***Figure 23**: MLE based on CDOP HH*

The key difference is that these signals measure a different physical property (frequency shift in [Hz] in stead of back-scatter) and may thus generate numbers of an entirely different order of magnitude. To compensate for this a weight parameter has been added to the software, and the square difference of the Doppler signals is divided by this weight before being added to the MLE sum. Since the numerical values where not known in advance a wide range of values was tried varying over several orders of magnitude. This is further discussed later.

An example MLE plot in which back scatter and Doppler signals are combined is given in Figure 24. At first sight it is already clear that the Doppler signal has a severe impact on the shape of the MLE function and the found local minima.

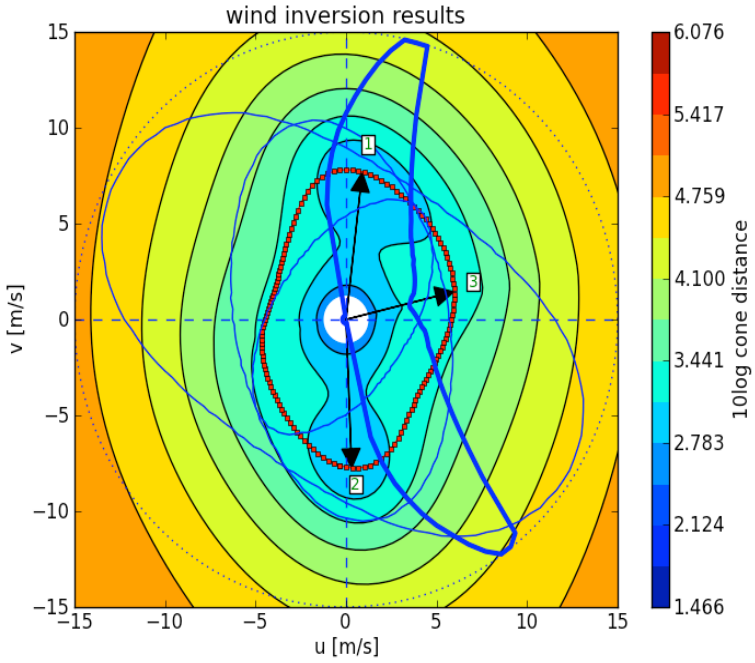

***Figure 24**: MLE for dopscat on midbeam*

We noted above that the GMF plays a determining role in defining backscatter retrieval functions and procedures. Since Doppler signals are not quasi-linear in wind speed, but rather in along line-of-sight wind component, we may expect incompatibilities in retrieval function and procedure. In particular, the local minima of the MLE will not represent the full wind observation probability density function $p(w,\phi|\sigma^0)$ and the strategy of finding minima along the wind speed dimension for each wind direction may be flawed. Once the Doppler GMF is accurately determined, the wind retrieval strategy may be refined. Moreover, since Doppler measurement noise is expected to be constant, no non-linearities are expected due to the denominator in Eq. 1.6.

Definition of Figure of Merit (FOM) numbers. To enable assessment of the quality of a given instrument, independent from the quality of a NWP model (which is needed for the usual ambiguity removal step) the figure of merit method was applied as described in [RD4]. First a distribution of wind retrieval solutions is collected from many simulations with the same input wind vector but different noise realizations taken from a Gaussian distribution (Monte Carlo method). This probability density function (PDF) is denoted as $P_{obs}(v'|v'_{+true})$ and contains all results reported by the wind inversion software for a given input wind vector (which usually gives 2, 3 or 4 local solutions). If the simulator generates more solutions, the chance is larger to find a solution close to the truth (input wind vector), which in turn may result in too optimistic performance numbers for some FOM definitions. To compensate for this a weight of $1/n_{sol}$ was applied during construction of this PDF. The prior knowledge usually imported by using neighboring and NWP data in the ambiguity removal step is simulated by defining a background truth PDF denoted as:

$$P_{NWP}(\mathbf{v}-\mathbf{v}_{true}) = \frac{1}{2\pi\sigma^2_{nbvr}}\exp\left(\frac{(\mathbf{v}-\mathbf{v}_{true})^2}{2\sigma 2_{nbvr}}\right)$$

(eq. 1.7)

and is normalized to have an integral of 1. From these two PDF functions a posterior PDF is constructed like this:

$$P_{acc}(\mathbf{v}|\mathbf{v}_{true}) = P_{obs}(\mathbf{v}|\mathbf{v}_{true}) \times P_{NWP}(\mathbf{v}-\mathbf{v}_{true})$$

(eq. 1.8)

which represents the posterior wind PDF that normally result after ambiguity removal. A "rejected" PDF is constructed from the remaining wind solutions:

$$P_{rej}(\mathbf{v}|\mathbf{v}_{true}) = P_{obs}(\mathbf{v}|\mathbf{v}_{true}) \times [\max(P_{NWP}) - P_{NWP}(\mathbf{v}-\mathbf{v}_{true})]$$

(eq. 1.9)

From these PDF definitions a general figure of merit is defined like this:

$$RMS_{obs} = \sqrt{\int\int [f(\mathbf{v}) - f(\mathbf{v}_{true})]^2 P_{acc}(\mathbf{v}|\mathbf{v}_{true})\,d\mathbf{v}}$$

(eq. 2.0)

$$RMS_{NWP} = \sqrt{\int\int [f(\mathbf{v}) - f(\mathbf{v}_{true})]^2 P_{NWP}(\mathbf{v}|\mathbf{v}_{true})\,d\mathbf{v}}$$

(eq. 2.1)

$$FOM_f = \frac{RMS_{obs}}{RMS_{NWP}}$$

(eq. 2.2)

The integrals in equations 5.4 and 5.5 above are performed over the relevant parts of the wind vector (u,v) domain, based on a binning of 251x251 cells using a range for the u,v components ranging from -2 to +2 times the wind speed of the input wind vector used by the simulation. This should ensure that all non-zero parts of the different PDF functions are covered by the chosen grid. Example PDF results for ASCAT are shown in Figure 25.

These equations can be applied to several properties of the wind vector using different definitions of the operator x, for example (taking u and v the 2 components of **v**):

- $f(\mathbf{v}) = \mathbf{v}$ results in the FOM for the wind vector difference
- $f(\mathbf{v}) = |\mathbf{v}|$ results in the FOM for the wind speed difference
- $f(\mathbf{v}) = \arctan\left(v/u\right)$ results in the FOM for the wind direction difference
- $f(\mathbf{v}) = u$ results in the FOM for the zonal component difference
- $f(\mathbf{v}) = v$ results in the FOM for the meridional component difference

Finally a special FOM is defined to extract information on the amount and distribution of ambiguities generated by the selected instrument. This accounts for the fact that multiple ambiguities close to the truth (input) wind are very detrimental for the overall quality of the wind retrievals, since they are not easily discriminated using prior NWP knowledge. On the other hand ambiguities far away from the truth should not cause any penalty because they are easily identified using prior knowledge. The following ambiguity FOM has these properties:

$$FOM_{AMBI} = \frac{\int P_{rej}\left(\mathbf{v}|\mathbf{v}_{true}\right)d\mathbf{v}}{\int P_{acc}\left(\mathbf{v}|\mathbf{v}_{true}\right)d\mathbf{v}} \qquad \text{(eq. 2.3)}$$

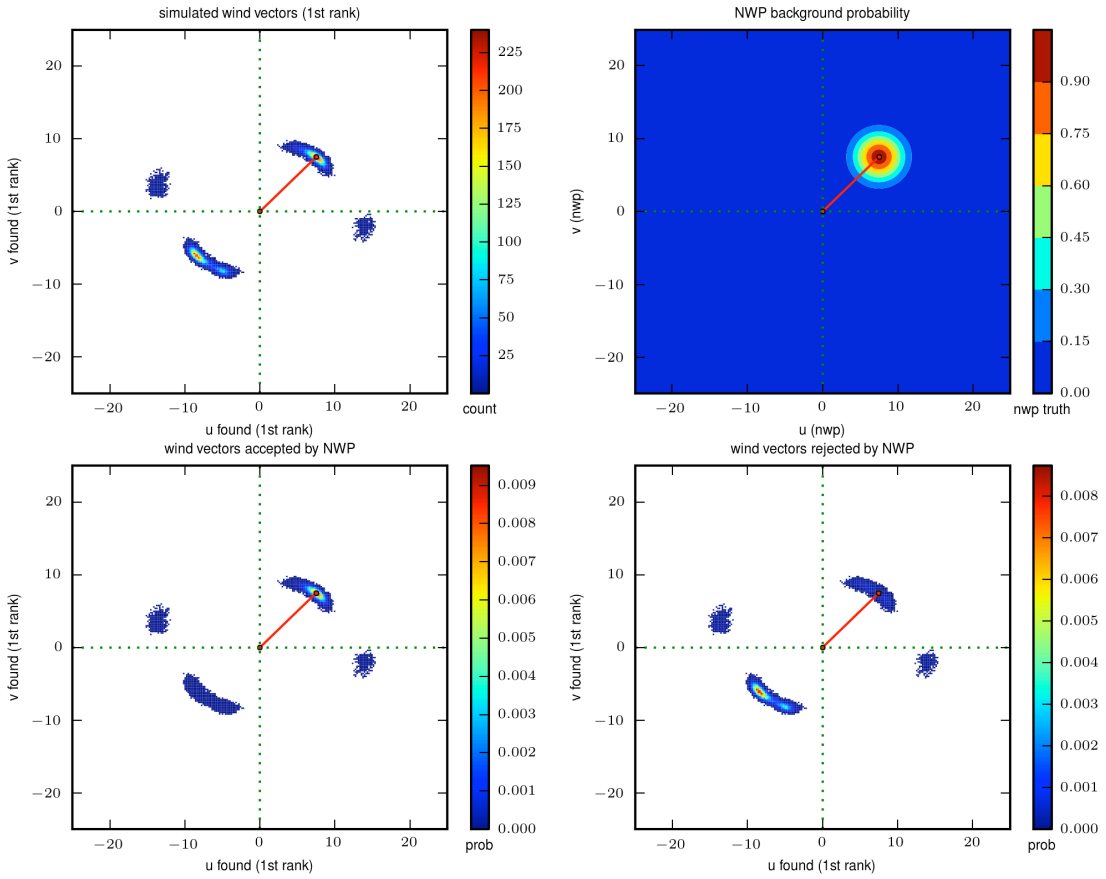

Figure 25: *Example PDF functions from an ASCAT simulation*

Definition of climate weighted FOM: The FOM numbers defined in the above section are valid for a single given input wind vector. From experience we know that the results vary strongly with input wind speed and direction. For comparisons between different scatterometer systems, or between different WVC's for the same system, it is convenient to construct a single FOM independent of wind speed and direction. To achieve this the results are integrated over many different wind speeds and wind directions. This is done numerically

by stepping over wind directions from 0 to 350 degrees with steps of 10 degrees, and over wind speeds from 3 to 16 m/s in steps of 1 m/s. In this summation a weight is introduced that mimics the occurrence of winds in reality on the globe. For this weight a Weibull distribution *G* was used, defined by:

$$G = \frac{p2}{p1}\left(\frac{w}{p1}\right)^{p2-1} \times \exp\left[-\left(\frac{w}{p1}\right)^{p2}\right] \qquad \text{(eq. 2.4)}$$

in which only the wind speed w occurs. In reality the real wind distribution differs because of the trade winds, but this is ignored in this study. The shape parameters used here are p1=10 and p2=2.2. Note that the shape is similar to the Rayleigh distribution, but only for p2=2 it is identical. In that case the width of the Rayleigh distribution is

$$\sigma = p1/\sqrt{2} = 7.07$$

This simulation system does 3 nested loops over the 2D wind vector domain! The inner loop does wind retrieval, the center loop calculates the FOM numbers for a given input wind vector, and finally the outer loop performs a scan to calculate Weibull-weighted climate-averaged FOM numbers. Thanks to the fact that the inner loop is coded in Fortran and optimized to use a smart search for local minima, and the center loop uses optimized masked 2D arrays, the run time to generate FOM results for a full swath at a chosen instrument geometry is reasonable and only about an hour on the hardware available to us.

TASK 3000: Case studies using selected data sets for extraction of surface current information

SUB-TASK 3100 - CASE STUDIES USING SCATTEROMETER DATA OR SIMULATED DATA

ERS2 collocations with ECMWF ERA40 model winds For this work package we have provided collocated wind results for the 3 cycles of ERS data processed by ARESYS. Inputs were binary matlab data files holding latitude, longitude and date, time values. Based on these we extracted 10 meter surface wind components (u and v), the land sea mask, and the sea surface temperature (to allow for ice screening) at the requested locations and times from the ERA40 reprocessed model data stored in the ECMWF MARS archive. We retrieved the data on a regular 0.5x0.5 degree lat,lon grid (note that this already implies an interpolation performed by the MARS system) and applied linear interpolation between 2 forecast times (closest before and closest after the requested time). No analysis fields where used, only 3, 6, 9, 12 and 15 hour forecasts based on model runs from 0 and 12 UTC. This choice was made because it is a known feature of analysis fields to contain small scale atmospheric features that do not propagate in time during evolution of the model (i.e. they are damped). Avoiding these fields makes the quality of the overall data set more constant.

An example of the retrieved data for cycle 10 is given in Figure 26 below. This shows the absolute CDOP values for the ERS mid beam derived from the collocated wind fields, binned and averaged over 145x145 latitude-longitude cells. Clearly patterns related to climatology of the atmosphere are visible.

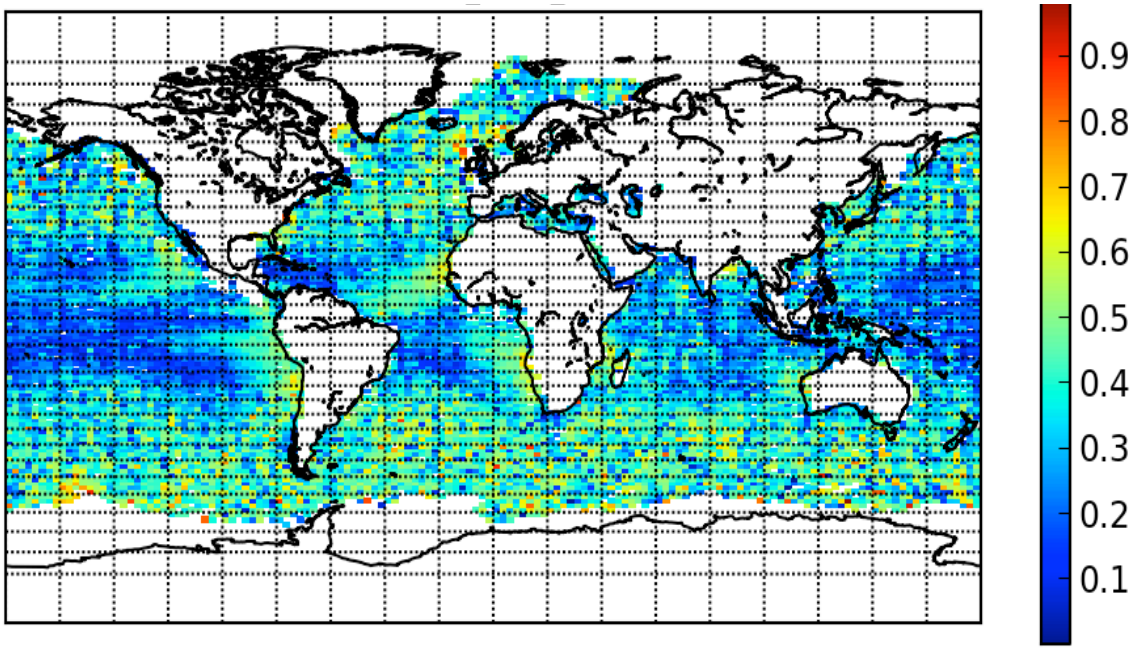

Figure 26: *Absolute CDOP values for the ERS mid beam for cycle 10, based on collocated ECMWF 10 m wind fields and averaged over 145x145 lat,lon cells.*

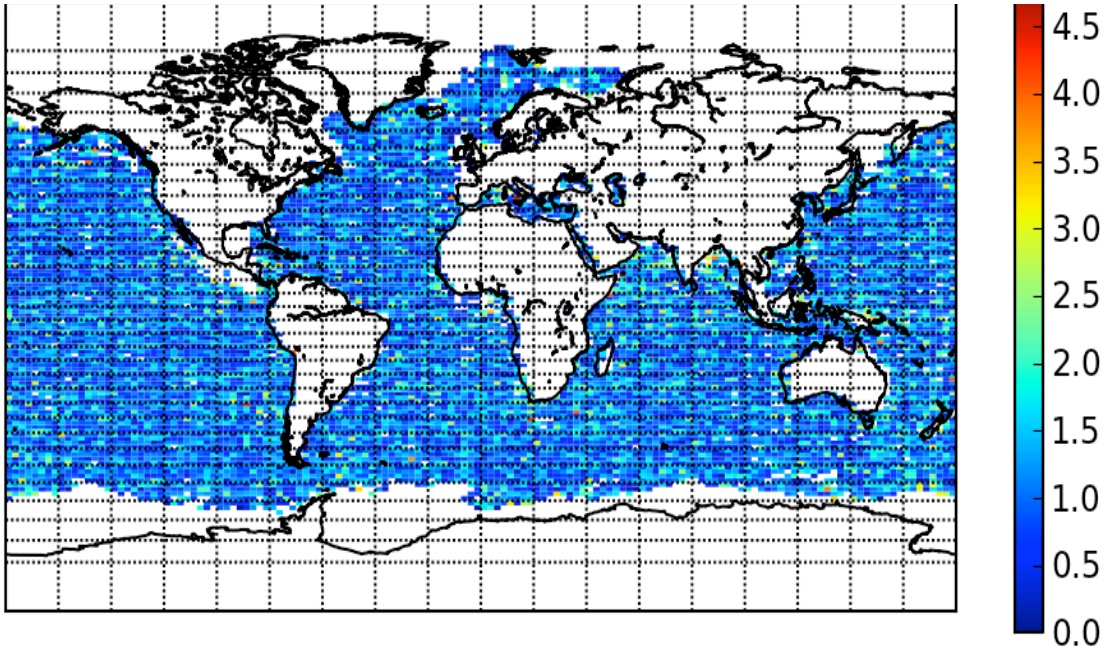

Figure 27: *Absolute DC values for the ERS mid beam for cycle 10, as retrieved by ARESYS and averaged over 145x145 lat,lon cells.*

If this is compared with the absolute Doppler Centroid (DC) data as retrieved by ARESYS, binned and averaged in the same way (see figure 10), no clear patterns are seen at all. This confirms the result by ARESYS (see below) that no clear correlation is present.

Processing of CLS simulation results. Based on the simulation results provided by CLS, KNMI performed the standard ERS/ASCAT type wind retrieval and reported on the result. Some pre-processing was needed before the standard wind retrieval software could be used, since CLS reported the complex signals on a 2D high resolution grid for each antenna (128x1755 azimuth x range elements for the mid beam, 128x8001 elements for the fore and aft beam). The applied steps are:

- use the down chirped data *rgc_az_signal_down,* take the square of it, and determine the mean of the 128 azimuth locations to obtain a 1D array. Then apply the gain factor by dividing the signal array by the square of gain_rg. Do the same for the rgc_az_noisy_signal_down array, which should contain the same information, now also including geophysical noise.
- use the proj4 library to calculate the antenna azimuth direction w.r.t. north, and the lat, lon values from the provided x,y,z location data
- split the data in 25 km range bins along a line perpendicular to the satellite track
- take WVC averages of the relevant parameters such as sigma0 (with and without noise), incidence angle, azimuth angle w.r.t north.
- insert the results in the KNMI inversion software and retrieve the calculated wind vectors
- calculate azimuth angle between input wind and antenna pointing angle, and calculate the cmod5n function for verification purposes.
- plot the results and generate output files to be reported back to CLS

This processing was performed on 64 data sets provided by CLS generated by the final version of their simulator. As discussed later 2 parameters where varied:

- SNR was varied over 17, 20, 23 and 26 dB
- Demodulation Error rate was varied over 0, 1e-5, 1e-4 and 1e-3

For each of these 16 cases, 4 different realizations of the simulation, based on different random seeds, where provided. Unfortunately, the results from this procedure still raise some concerns, and we suspect still some unresolved bugs are present in this software chain. The main issue is that addition of the geophysical noise term seems to add bias to the retrieved wind result, but does not change the stdev. of the error in the wind result significantly. An example of such a result is given in Figure 28. This may be due to the fact that CLS applied the parametrization (see eq. nn) for this noise term not on WVC scale, but at much smaller scales. In this case unsampled WVC wind variability is larger and so should this noise term be as well. This should thus underestimate geophysical noise effects and not cause the offsets displayed in Figure 11. Yet another problem may be the repeated use of the same random seed or random sequence for this noise contribution.

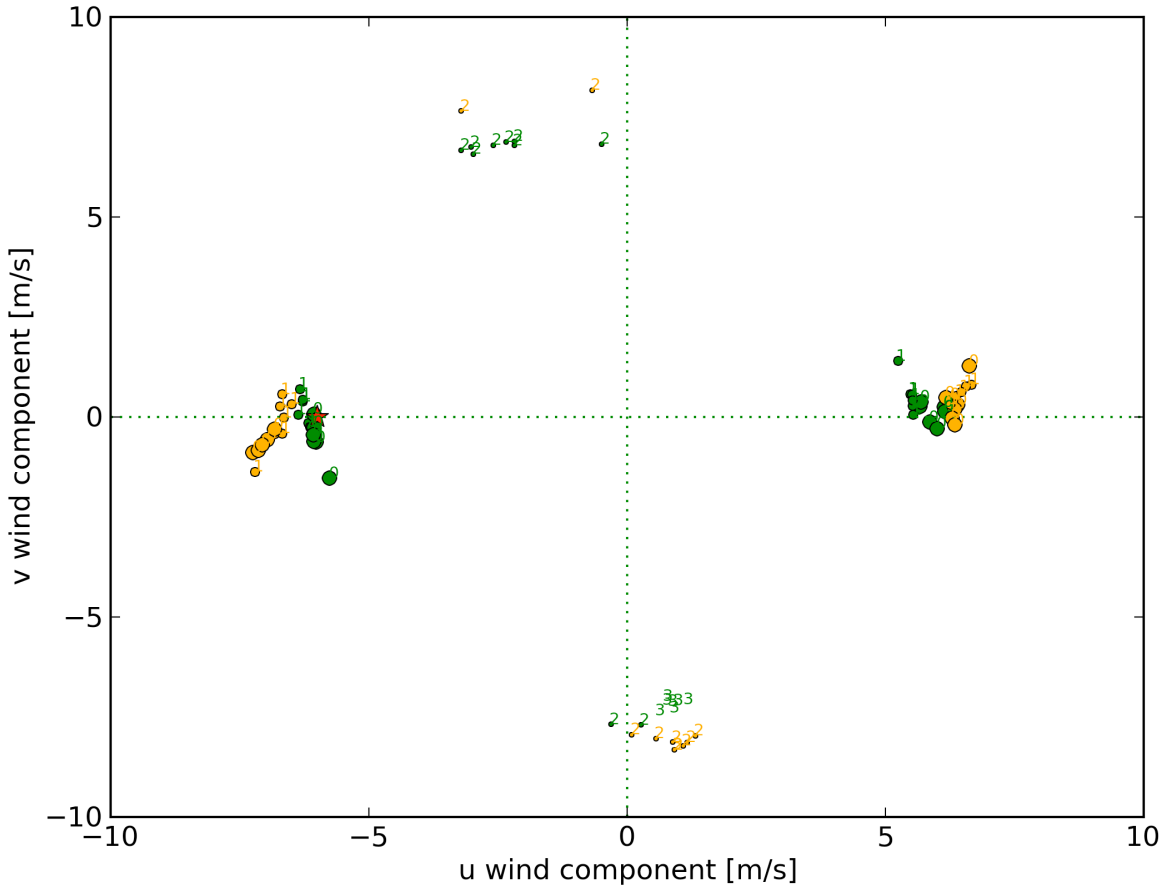

Figure 28: *wind retrieval result for the 12 WVC's of one case (SNR 17dB, DemodErr 1e-3, file of 21-Apr-2013). Yellow dots are including geophysical noise, green dots are without this noise term. The input wind is given by the red star. The numbers printed for each solution give their rank. A rank of 0 means that solution has the lowest MLE value, and has the highest probability to be the correct one.*

Figure 28 clearly shows that adding geophysical noise only adds wind speed, and does not change much in the spread of the points. This same unanticipated effect is seen for all other simulation results as shown in Figure 29. This result clearly shows that the addition of bias is a systematic effect. It is reproducible over the 4 realizations simulated for each combination of input parameters. It also clearly increases for increasing distance to nadir. In addition, a smaller systematic bias is seen for both wind direction and wind speed, even for the cases without geophysical noise. This was further investigated by recalculating the wind retrievals using the clean signals without any instrument noise. These show this smaller bias as well, as can be seen in Figures 30 and 31. In addition is it clear that the Demodulation Error rate has no effect on the wind retrieval results at all.

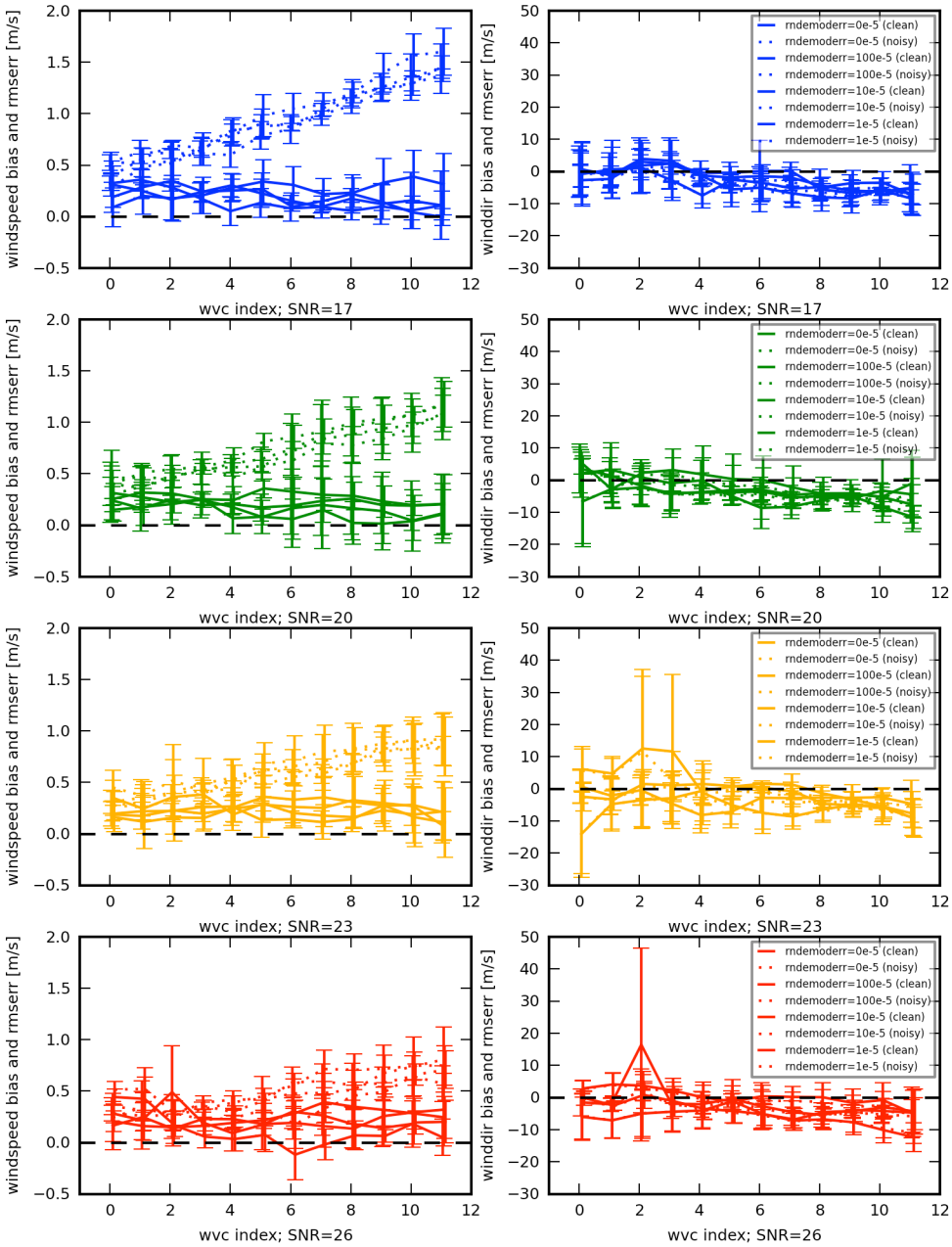

***Figure 29**: Overview of stdev and bias of all simulation results for wind speed (left panels) and wind direction (right panels)*

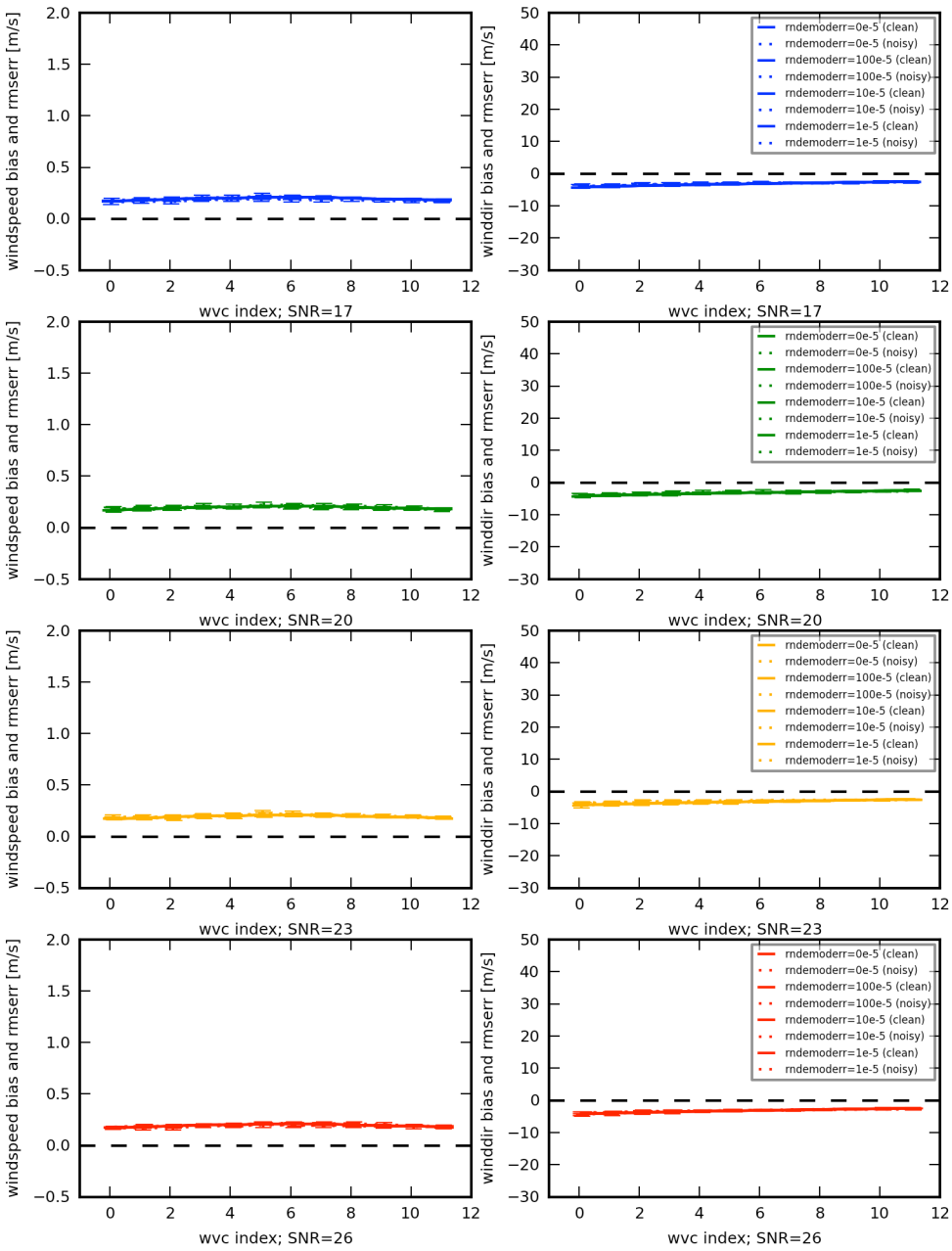

Figure 30: *Similar plot for all simulation results, now based on the clean noiseless signals that also are provided in the datafiles.*

From these noiseless results, it is clear that a smaller bug must exist that causes small (0.2 m/s and -3 degree biases) for all test cases and all locations. In a first attempt to find the problem, the sigma0 values and the geophysical noise where plotted against each other in Figure 32. This clearly shows that this error does not behave as expected. It was expected that a noise term behaves symmetric, i.e. adds and subtracts to the signal with the same occurrence frequency. However, it seems the current implementation of the geophysical noise only adds to the sigma0 signal, which in turn explains why we primarily see an increase in wind speed in our wind retrieval results. Within the current project there was no time left to do any more debugging. Therefore, it must be noted that these are still preliminary results which should be carefully reviewed and probably recalculated, before they can be used as input to other studies or to draw conclusions from them.

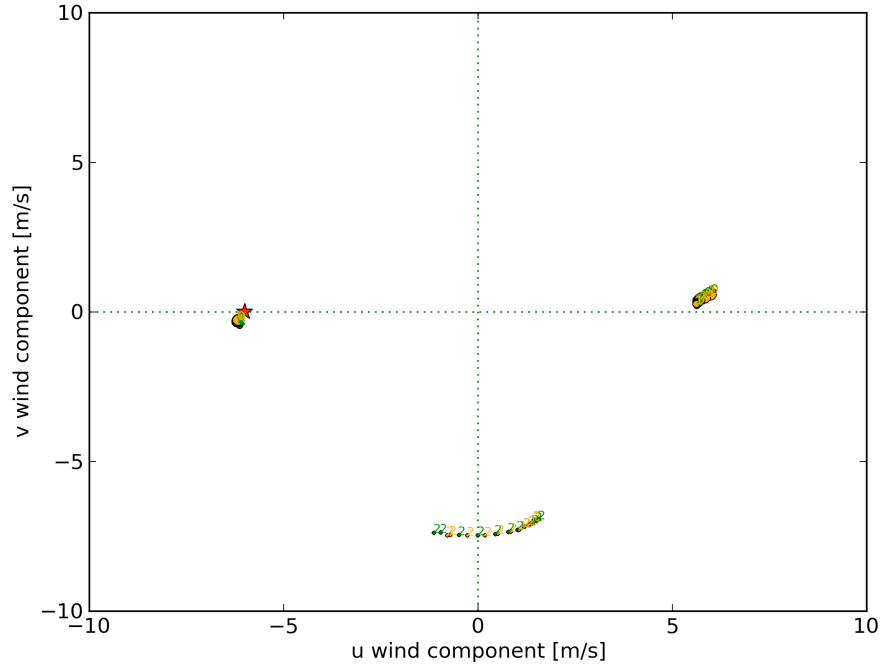

Figure 31: *Wind retrieval result for one example simulation without any noise (SNR 17dB, DemodErr 1e-3, file of 21-Apr-2013).*

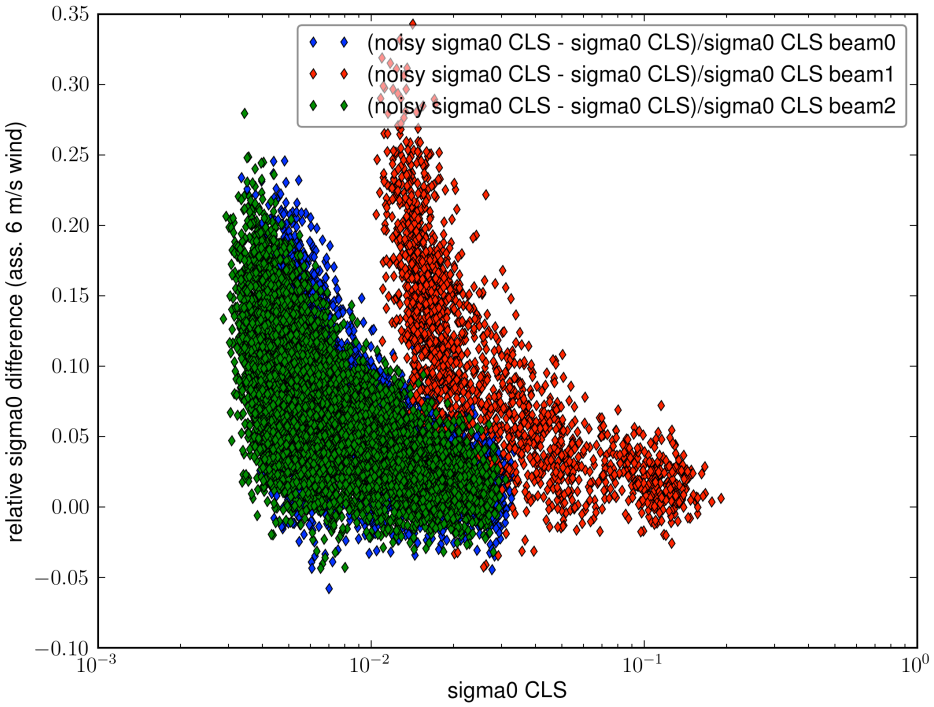

Figure 32. *Relative geophysical error plotted against sigma0*

Doppler estimation from WS raw data

The Doppler shift affecting the signal poses a problem for the reception, since the received signal could fall outside the on-board filters bandwidth [RD16]. This was particularly true for the signals received by the after/fore antennas which, due to the squinted geometry, were affected by a very high Doppler shift (up to 50 kHz). For this reason the received signal underwent an on-board demodulation step. The demodulation was orbit position dependent. For the mid antenna all the received echoes were shifted of the same frequency, since the across-track Doppler shift variation was reduced. On the contrary the after/fore antenna demodulation was also range dependent, to cope with the strong across-track variation of the Doppler shifts. The on-board demodulation step must be considered during the Doppler shift estimation process, in order to not introduce biases in the obtained results.

The raw data generated by the wide swath (WS) mode were disseminated in Level-0 products called AMI Wind Calibration data (EWIC) [RD15]. This product contains one AMI wind scatterometer and one General Header Source Packet. The General Header is the one just preceding the first frame of Instrument Data. Figure 33 shows the structure of the Level-0 EWIC data. Several WS acquisitions are concatenated to form the product, the general rule is to aggregate all the acquisitions from a passage over the North Pole to following one (about 6000 seconds).

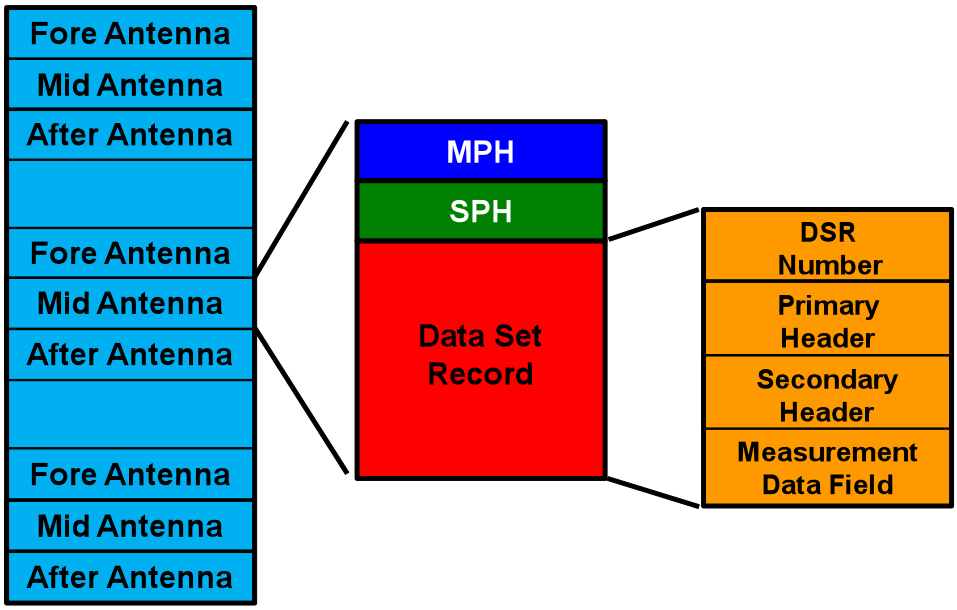

Figure 33. *Level-0 AMI Wind Calibration products structure. Several WS acquisitions are concatenated to form the product.*

The antenna acquisitions are stored in packets with a length of 7860 bytes. The structure of each packet is the following:

- Main Product Header: containing generic information on the product
- Specific Product Header containing ancillary data not relevant for the Doppler estimation processing
- Data Set Record containing some metadata and the scatterometer measures (echoes + calibration)

Each Data Set Record presents the following structure:

- Data Set Record Number
- Primary Header (6 bytes): allowing the identification of the packet and of the antenna.
- Secondary Header (62 bytes): containing the timing information and the Doppler compensation information. This information is particularly important for the Doppler shift estimation process.
- Measurement Data Field (7792 bytes): containing the echoes and the calibration pulses. The samples are represented as complex numbers (1 byte for I and 1 byte for Q channel).

As mentioned before, the fact that the EWIC data are complex represents the fundamental reason for their exploitation within the DOPSCAT project. The WS antennas transmitted rectangular pulses with a fixed length resulting in a sinc shaped spectrum with a bandwidth of 14.3 kHz for the mid antenna and a bandwidth of 7.7 kHz for the fore/after antennas. Figure 34 shows the along track and across track spectra of a WS acquisition performed with the fore antenna on the 4th April 1996. The very flat along-track spectrum is due to the very reduced sampling frequency, the expected sinc shape can be observed for the across-track spectrum. For comparison the across-track spectrum of a mid-antenna acquisition is also shown (red line). The different shape is due to the different characteristics of the transmitted pulse.

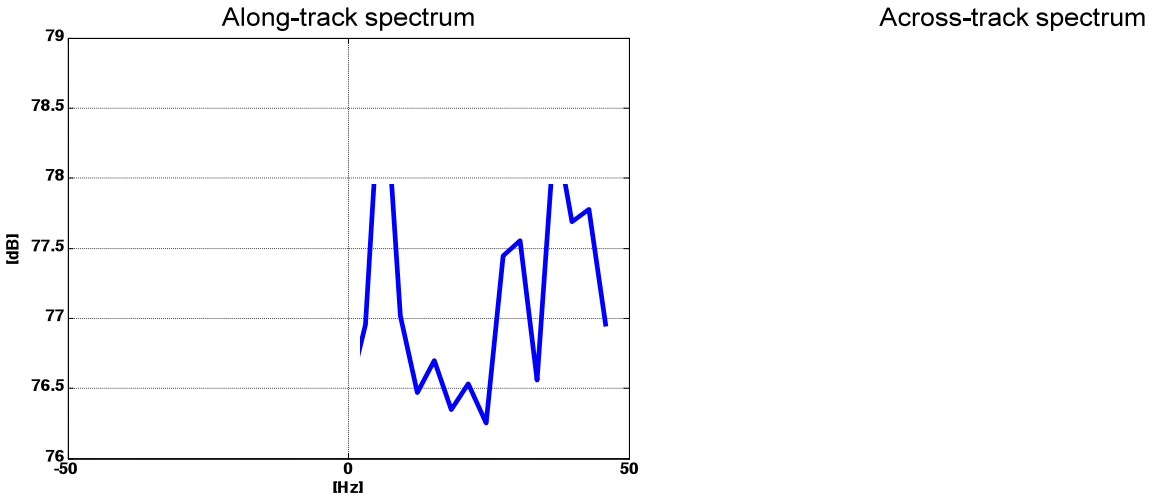

Figure 34. *Along (on the left) and across (on the right) track spectra of the WS data of a fore antenna acquisition. The along track spectrum is very flat due to the very reduced sampling frequency. The across track spectrum shows the expected sinc shape (Fourier transform of a rectangular pulse). For comparison*

The SAR techniques used for the Doppler shift estimation look for the peak in the azimuth (along-track) spectrum. For the WS data this is clearly not possible, since the along-track spectrum is totally flat. However the across-track spectrum presents a well-defined peak, allowing to apply to the scatterometer raw data SAR-like techniques for the Doppler shift estimation. The following sections describe the different Doppler estimation techniques tested during the activity. The techniques have as common input the raw data, intended as the complex signal of a single antenna acquisition. The common output is a single Doppler shift representative of the whole considered swath. Due to the very reduced number of the across-track samples (72 for the mid antenna or 118 for the fore/after antennas), it is not possible to have more than one estimate per swath.

Peak detection method: The peak detection technique is a very simple spectral technique, directly looking for the peak of the across-track spectrum. Figure 35 shows the flow chart of the Doppler estimation processing. The following processing steps are foreseen:

- Spectrum computation: the along-track spectrum for each of the 32 lines of the acquisition is calculated through an FFT. The obtained spectra are then incoherently averaged (sum of the power spectra) to improve the accuracy.
- Coarse peak detection: the sample with the maximum absolute value within the obtained average spectrum is retrieved. The position of the maximum is returned.
- High-resolution spectrum computation: the high resolution spectrum around the frequency of the previously retrieved maximum is calculated through a Chirp-Z Transform. The CZT is the z-transform of a given signal along a spiral contour. In this case the spiral contour is the portion of the unitary circle around the coarse peak detected at the previous step. Again the spectrum is calculated for each of the 32 lines of the acquisition. The obtained spectra are then incoherently averaged to improve the accuracy.
- Fine peak detection: the obtained high resolution spectrum is fitted with a 2^{nd} order polynomial. The position of the maximum is obtained calculating analytically the position of the vertex of the parabola.

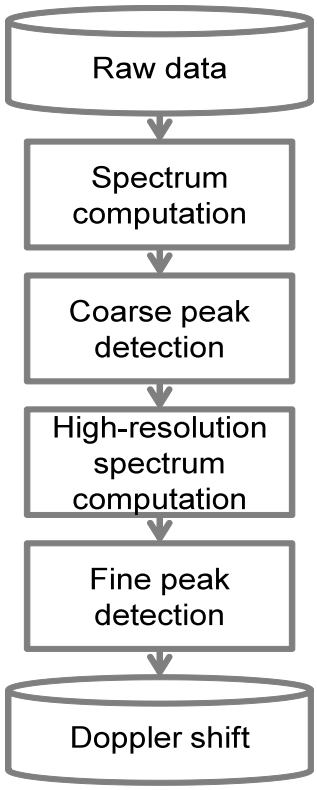

Figure 35. *Flow chart of the peak detection technique used for the Doppler shift estimation.*

The technique is very simple but inaccurate due to the noise affecting the received signal and to the reduced number of available samples. For this reason no thorough analyses were performed with this technique.

Adjacent Cross-Correlation Coefficient method: The Adjacent Cross-Correlation Coefficient (ACCC) technique looks, as the previous method, for the peak of the signal spectrum, but in an indirect way. This estimator is based on the properties of the power spectral density of the scatterometer signal. It uses the Fourier relationship between the power spectrum $S(f)$ and the auto-correlation function $s(\tau)$ of the data. In particular, the phase gradient of the auto-correlation around zero lag results to be proportional to the frequency

location of the maximum of the spectral density function (i.e. the searched Doppler shift). This gradient may be estimated by calculating the phases of $s(1)$, $s(2) \ldots s(N-1)$. As the value of $s(1)$, the first sample of the auto-correlation, has the highest signal-to-noise ratio, it's the best option for the current algorithm. The method was proposed by Madsen and is often used in SAR processing to estimate the Doppler Centroid [RD17]. The returned Doppler shift value is ambiguous, i.e. it is wrapped between $-f_s/2$ and $f_s/2$. This is usually a problem for SAR data but not for the considered WS data, since the across-track sampling frequency (30 kHz) is high enough for avoiding spectrum aliasing.
Figure 36 shows the flow chart of the Doppler estimation processing. The following processing steps are foreseen:

- Autocorrelation function computation: the autocorrelation function is calculated for each of the 32 lines of the acquisition. The autocorrelation function is calculated in the time domain and only the first sample is retrieved.
- Coherent averaging: the first lag of the autocorrelation functions calculated at the previous step are coherently averaged. Since the phase information is exploited the average results in a coherent summation of the complex samples.
- Phase to frequency conversion: the phase of the calculated first sample of the autocorrelation function $s(1)$ can be directly converted into the position of the maximum of the signal power spectrum as:

$$f_{data} = \frac{\angle s(1)}{2\pi} f_S \tag{3.1}$$

where f_S is the across-track sampling frequency (30 kHz for all the scatterometer antennas).

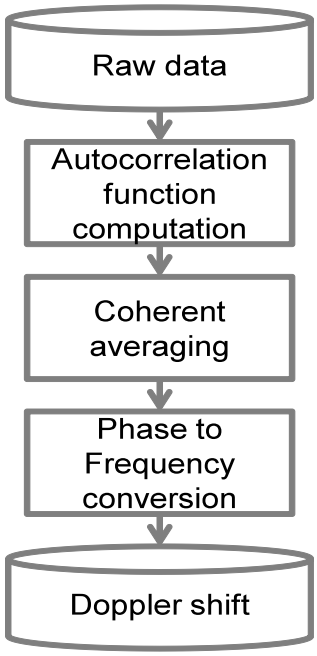

Figure 36. *Flow chart of the peak detection technique used for the Doppler shift estimation.*

This method is very simple and allows a very good estimation accuracy, especially for the acquisitions over uniform regions such as Rain Forest or open ocean. It is to be noticed that,

unlike SAR, the returned Doppler shift frequency does not correspond exactly to the Doppler shift affecting the center of the estimation block (the whole WS antenna swath in this case). This is due to the fact that the signal spectrum formation process is not symmetric: several pulse replicas are summed with different Doppler shifts and weights (see next sections for more details). This has to be considered when the reference Doppler function is obtained from the sensor geometry. In this case the simplicity of the method is counterbalanced by the reference Doppler function calculation complexity. The plot on the left of Figure 37 shows the comparison between the mid-range Doppler shift and the corrected Doppler shift considering the ERS-2 nominal attitude. The plot on the right shows the difference between the two functions, which is up to 30 Hz for some orbital points (before and after Antarctic): this is a not negligible bias for the considered global ocean surface current mapping application. The difference is compared with the bias between the ACCC and the MLS estimates over the same EWIC products. Since the bias is originated by the fact that the MLS method considers the signal spectrum formation process to estimate the shifts, a similar trend for the bias and the theoretical difference is expected. Indeed a correlation between the two functions can be noticed, even though they do not fully agree due to the inaccuracies in the spectrum modeling (e.g. bad attitude information).

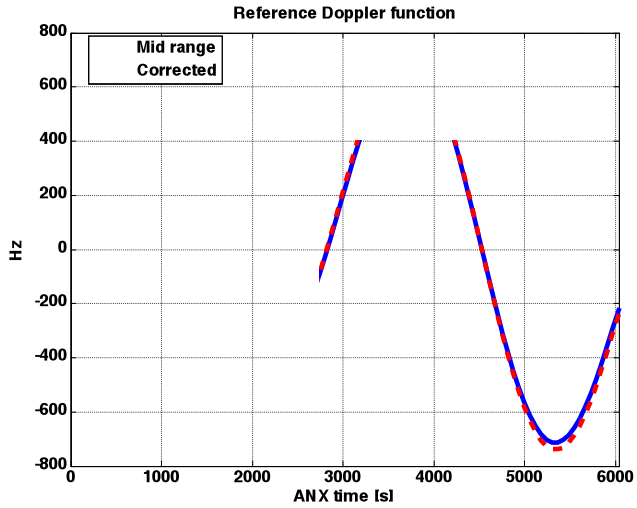

Figure 37. *The plot on the left compares the reference Doppler function calculated considering the Doppler shift at mid-range (blue line) with the reference Doppler function calculated considering the signal spectrum formation process (red dashed line). The plot on the right shows the difference between the two functions (red line) compared with the bias between ACCC and MLS estimates (blue dots).*

Minimum Least Squares method: The Minimum Least Squares (MLS) estimation technique looks for the Doppler shift minimizing the least square error between the calculated and the modeled across-track spectrum. The method requires as input, along with the raw data, the sensor orbit and attitude information in order to perform a better modeling of the spectrum.

Figure 38 shows the flow chart of the MLS Doppler estimation processing:

- Spectrum computation: the along-track spectrum for each of the 32 lines of the acquisition is calculated through an FFT. The obtained spectra are then incoherently averaged (sum of the power spectra) to improve the accuracy.
- Spectrum modeling: this is the key point of the present technique. The expected along-track spectrum is calculated according to the defined spectrum model. The complexity of the model is a trade-off between the desired accuracy and the computational cost of the

technique. Figure 39 shows that the final shape of the along-track spectrum is determined by the super-imposition of the pulse replicas with different Doppler shifts and weights.

- The Doppler shifts depend on the range delay of each replica and can be predicted if the sensor acquisition geometry is known. The on-board demodulation shall also be considered, particularly for the fore/after antennas for which the demodulation is range dependent.
- The weight of each replica depends on several factors:
- Spreading losses
- Antenna pattern weighting
- Ground reflectivity (including incidence angle dependency)
- The shape of the spectrum is finally determined by the on board anti-aliasing filtering through which the signal undergoes.
- This step is somehow similar to the calculation of the Doppler Reference function for the ACCC method described in the previous section.

- MLS shift estimation: this step looks for the Doppler shift minimizing the quadratic difference between the calculated spectrum and the model. In the minimization process also the spectrum gain is refined. Since the model is not linear the iterative Gauss-Newton method is exploited for the minimization process. According to the estimation theory, the MLS estimator is equivalent to Maximum Likelihood Estimator, which is the theoretical optimum estimator, in presence of uniform Gaussian noise (all the estimates have the same Standard Deviation). Here the spectrum samples present different Standard Deviation due to the speckle noise (which is multiplicative) but the minimization is performed in a logarithmic domain so that the noise becomes additive and with all the noise samples have the same standard deviation.

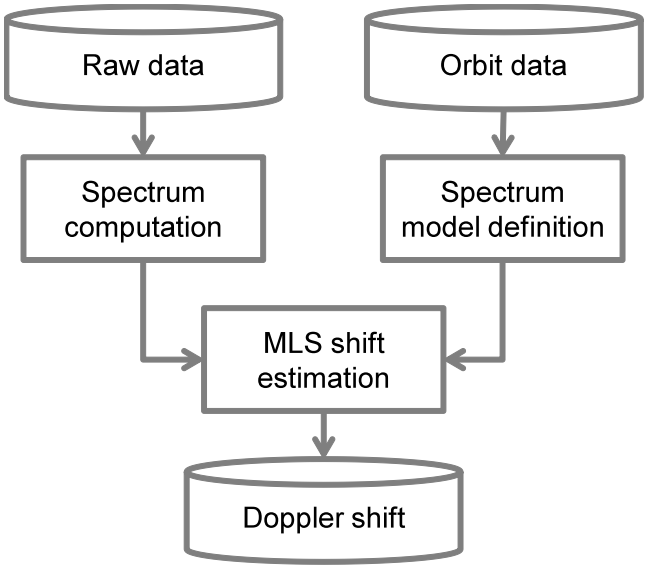

***Figure 38**. Flow chart of the MLS estimation technique used for the Doppler shift estimation.*

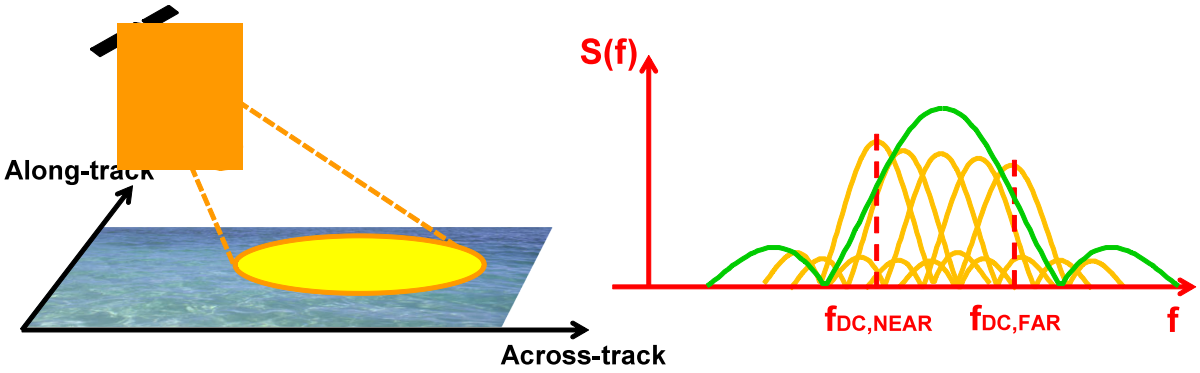

Figure 39. *The along-track spectrum shape depends on the super-imposition of the pulse replicas with different Doppler shifts and weights.*

The method accuracy strongly depends on the capability to correctly model the signal spectrum. Furthermore, if a good modeling is performed, no Doppler reference function is required, since the spectrum model is already shifted of the expected quantity. For the present analysis, the usage of the sensor nominal attitude allows to perform the shift estimation, but a reference Doppler function is required to retrieve the "geophysical" Doppler contribution.

Doppler estimation algorithms comparison: The proposed algorithms present different performances due to the different strategies implemented to retrieve the Doppler spectral shift affecting the raw scatterometer data. Figure 40 shows a comparison of the estimation accuracy of the proposed methods. The scatter plot on the left represents the Doppler shift estimates, obtained from the same EWIC product, as a function of the ANX time. The histogram on the right represents the distribution of the estimates, after removing the ANX dependent average value. As expected the MLS method, which is the theoretical optimum method, shows the better estimation accuracy, even though the accuracy of the ACCC method is quite close to it.

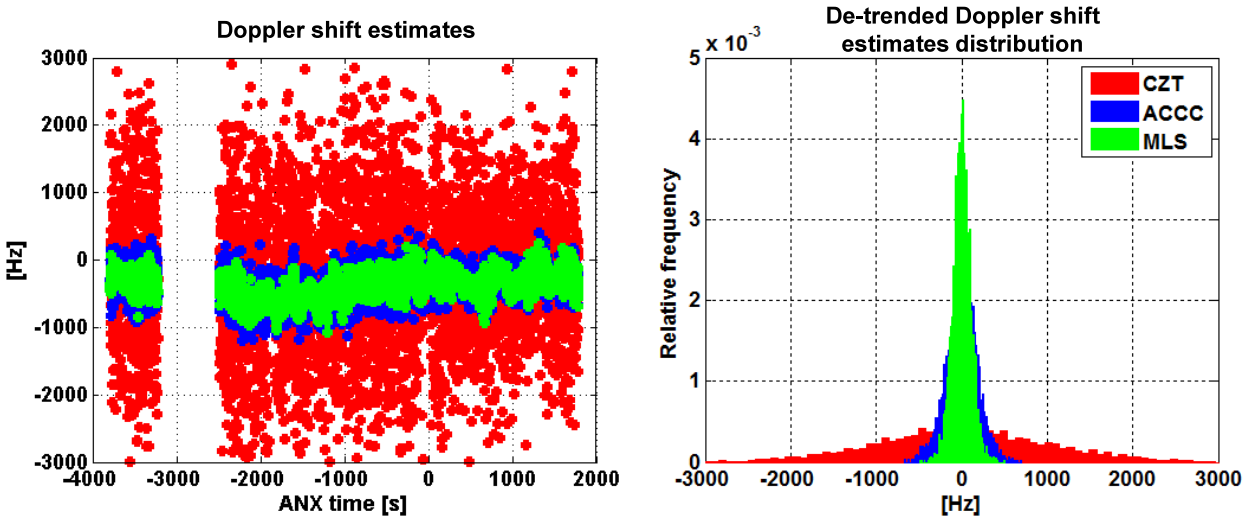

Figure 40. *The scatter plot on the left represents the Doppler shifts estimated with the 3 methods as a function of the ANX time. The histogram on the right represents their distribution after average subtraction.*

The obtained accuracy value can be compared to the theoretical accuracy value, retrieved exploiting the Cramer-Rao bound. Bamler calculated this accuracy limit for several SAR

Doppler Centroid estimation techniques, but the analysis can be easily extended to the proposed techniques, which directly derive from SAR methods. The theoretic Cramer-Rao bound, representing the minimum achievable estimation variance σ^2_{EST}, can be expressed as:

$$\sigma^2_{EST} = \frac{\Delta f}{M} \frac{\int [A(f)B(f)]^2 df}{\left[\int A(f)B'(f)df\right]^2} \tag{3.2}$$

where:

- Δf is the spectrum sampling frequency (ratio between the signal sampling step f_s and the number of samples)
- M is the number of averaged spectra
- $A(f)$ is the signal spectrum model
- $B(f)$ is the kernel function associated to the Doppler shift estimation method. Indeed, Bamler showed that each Doppler estimation process is equivalent to look for the zero in the cross-correlation function between the signal spectrum and the corresponding kernel function. A "good" kernel function is one averaging over many spectrum samples (to keep the variance low) and, on the other hand, allowing for a high discrimination power by generating a large slope of the cross-correlation function. Figure 41 shows the comparison between the kernel functions associated to the ACCC and MLS Doppler estimation methods.

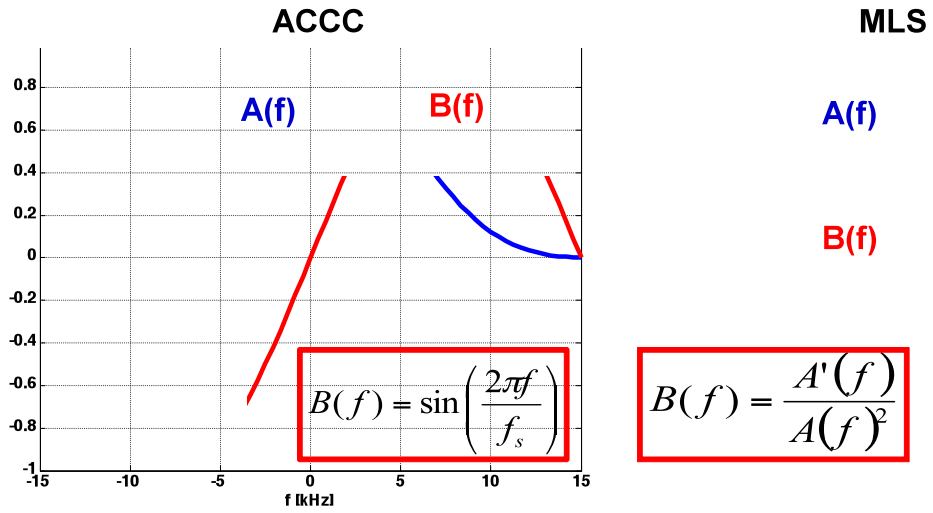

Figure 41. *Comparison of the kernel functions of the ACCC and MLS Doppler shift estimation methods*

By numerically integrating Eq. (3.2) it is possible to calculate the theoretical estimation accuracy for the proposed ACCC and MLS methods (the peak detection method is no longer considered due to its reduce accuracy).

Table 3.1 lists the statistics of the Doppler estimates represented in the histogram of 0. The standard deviation of the ACCC and MLS methods is compared to the theoretical Cramer-Rap bound. The difference between the two values is originated by the non-idealities in the acquired data, such as the noise and the non-uniformity of the acquisition region.

Method	μ [Hz]	σ [Hz]	Cramer-Rao bound [HZ]
Peak detection	14.662	1034.067	N.A.
ACC	0.479	179.868	143.1
MLS	0.162	107.229	63.0

Table 3.1. *Estimation techniques Doppler estimates statistic and comparison with the Cramer-Rao bound*

Table 3.2 resumes the main features of each of the proposed estimation methods, focusing in particular on the advantages and drawbacks of each method.

Method	PRO	CONS
Peak detection	• No need of orbital and attitude information	• Very low accuracy • Need of Doppler reference function
ACC	• No need of orbital and attitude information • Low computational cost	• Not the optimum estimator • Need of Doppler reference function
MLS	• Theoretical optimum estimator • No need of Doppler reference function	• Need of orbital and attitude information • Complicated modeling • High computational cost

Table 3.2. *Comparison between the different Doppler estimation techniques.*

According to the estimation methods features, listed in the previous table, the following data analyses have been performed:

- 3 full cycles of EWIC data have been processed exploiting the ACCC method. This is the best estimation method for the trade-off between complexity and accuracy and allows to perform a valid feasibility assessment of the global ocean surface current mapping using scatterometer data. The bias affecting the method is removed by considering as reference Doppler function the average Doppler shift of all the still land WS acquisitions of the cycle (see Section Table 3.3 for more details).
- A subset of products of one of the cycles has been processed exploiting the MLS method. This is the method allowing to obtain the best estimation accuracy and hence the best candidate for the global ocean surface current mapping using scatterometer data. Its high computational cost is partly compensated by the fact that if the spectrum model is accurate enough (this should not be a problem for new generation sensors) no reference Doppler function is required, since the Doppler shift is obtained w.r.t. the expected signal spectrum position. For the present analysis, due to the poor modeling, the average Doppler shift of the considered still land WS acquisitions of the cycle was used as reference Doppler function.

Doppler estimation over EWIC data results

The results showed in the present section have been obtained analyzing the mid antenna acquisitions only. The after/fore antennas are strongly impacted by the very low accuracy of the available attitude information. Indeed for such antennas, due to their squinted acquisition geometry, a mispointing error of few hundredths degrees can result in several kHz of Doppler shift. Furthermore, it was very complicated to extract from the data the information related to the on-board demodulation, not allowing a correct modeling of the received signal spectrum. For these reasons the after and fore antenna acquisitions are not mentioned in the prosecution of the document.

Test datasets description: The ERS- 2 sensor followed a sun-synchronous near circular polar orbit with a repetition cycle of 35 days. The nodal period was about 6036 s, resulting in 501 orbits per cycle. After the 35 days the orbits repeat the same pattern and for this reason the cycle has been selected has basis for the present analysis. The following tables lists the features of the 3 full EWIC cycles processed within the framework of the DOPSCAT project.

Cycle	Start	Stop	EWIC products	Data size	Processing time (ACCC)
10	25th March 1996	29th April 1996	465	50.0 GB	~7 days
13	8th July 1996	12th August 1996	271	27.2 GB	~5 days
14	13th August 1996	16th September 1996	464	55.6 GB	~8 days

Table 3.3. *Comparison between the different Doppler estimation techniques.*

The indicated processing time is referred to the time required to process all the EWIC products of the cycle with a MATLAB® implementation of the ACCC algorithm over a 32 bit Pentium® Dual-Core CPU E5200 @2.50 GHz system with 2 GB of RAM memory (only one core of the processor was actually used).

Reference Doppler function definition: The reference Doppler function, i.e. the "geometrical" Doppler shift to be subtracted to retrieve the "geophysical contribution", should be calculated, for each WS acquisition, considering the ERS-2 orbit information and the sensor steering law. However, due to the poor steering accuracy of the sensor, this was not possible and a different approach has been considered. In particular the cycle average Doppler shift as a function of the Ascending Node Crossing time has been considered. In order to obtain a non-biased Doppler reference only the still land acquisitions have been considered during the averaging operation. The plot on the left of Figure 42 shows the obtained reference Doppler functions, for the processed EWIC cycles, as a function of the ANX time. The jumps in the Doppler reference functions are originated by the changes of the demodulation frequency applied on board to the received signal. The gaps in the functions are originated by the fact that no still lands are present for a particular ANX time. This is the case of the Arctic region (around 1500 s) and of the gap between South America an Antarctic (around 4000 s for descending orbits and around 5000 s for ascending orbits). The trend of the estimates is quite similar but a residual difference, originated by the poor ERS-2 attitude control capability, can be noticed. The difference is represented in the plot on the right: the maximum difference, between cycle 13 and 10, is around 100 Hz.

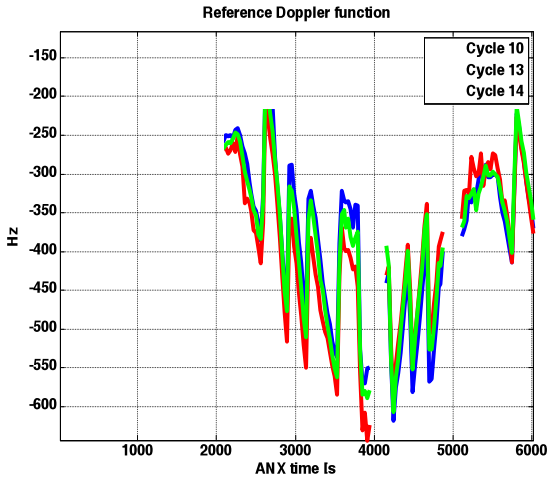

Figure 42. *The image on the left represents the Reference Doppler functions calculated for the three EWIC cycles as a function of the ANX time. The image on the right represents the difference between the different pairs of functions.*

DC estimation results: The results showed in the present section have been obtained following the processing illustrated in Figure 38. The averaging step was performed considering an along track step of about 30 seconds, corresponding to a resolution of about 250 km. The final Doppler shift estimates have then a resolution of 400 X 250 km. This is a very coarse resolution, but it is originated by the originally very reduced sampling of the WS. Figure 43 to Figure 45 show the obtained Doppler shifts calculated for the considered ERS-2 cycles: two plots, one for ascending and one for descending orbits, are represented for each cycle. The peak to peak variation of the estimates is quite large (about 500 Hz) but regions with an uniform Doppler shift, especially above still land (e.g. South America), can be noticed.

Table 3.4 shows the statistics of the estimated Doppler shifts. The statistics are separated per cycle, orbit direction and scene content (sea or land). The overall estimation accuracy is a bit higher than 150 Hz (3σ value). It is interesting to note that the average value of sea and land acquisitions is always slightly different and the accuracy of the sea estimates is always slightly higher. This could indicate the presence of a geophysical signal in the observed data.

	Cycle 10			Cycle 13			Cycle 14		
	N	μ [Hz]	3σ [Hz]	N	μ [Hz]	3σ [Hz]	N	μ [Hz]	3σ [Hz]
Global	61088	12.046	164.3	33251	14.262	165.4	68255	8.818	159.4
Ascending	32925	17.698	164.3	17608	11.161	158.0	36806	10.295	152.8
Descending	28163	5.439	162.1	15643	17.751	172.8	31449	7.090	166.7
Sea	38875	10.924	167.4	20160	16.231	167.6	41706	7.867	162.3
Land	22213	14.010	158.7	13091	11.229	161.5	26549	10.314	154.7

Table 3.4. *Statistics of the Doppler centroid estimates*

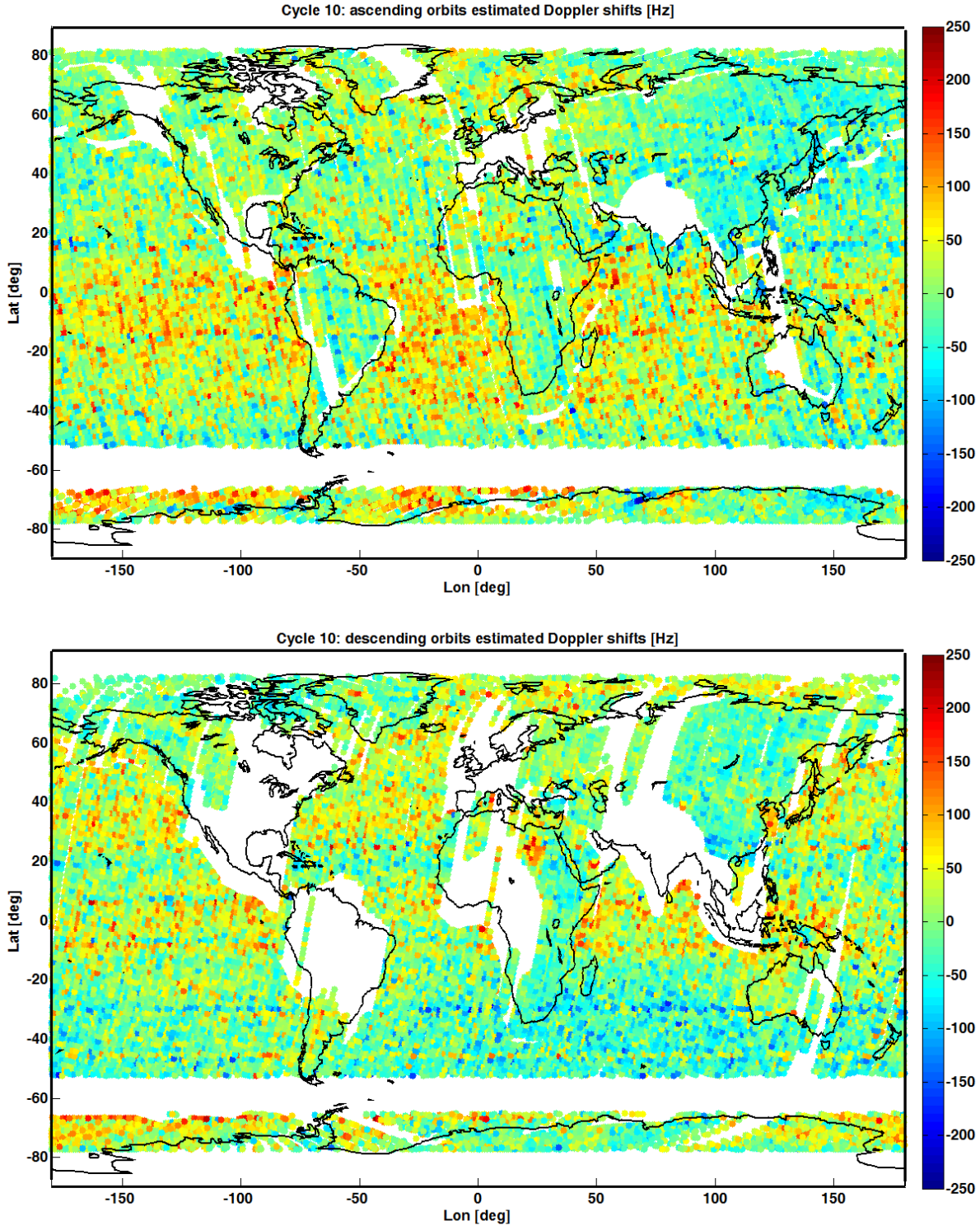

Figure 43. *Doppler shifts estimated from the EWIC products belonging to ERS-2 cycle 10. The figure on the top represents the ascending orbits, while the figure on the bottom represents the descending orbits.*

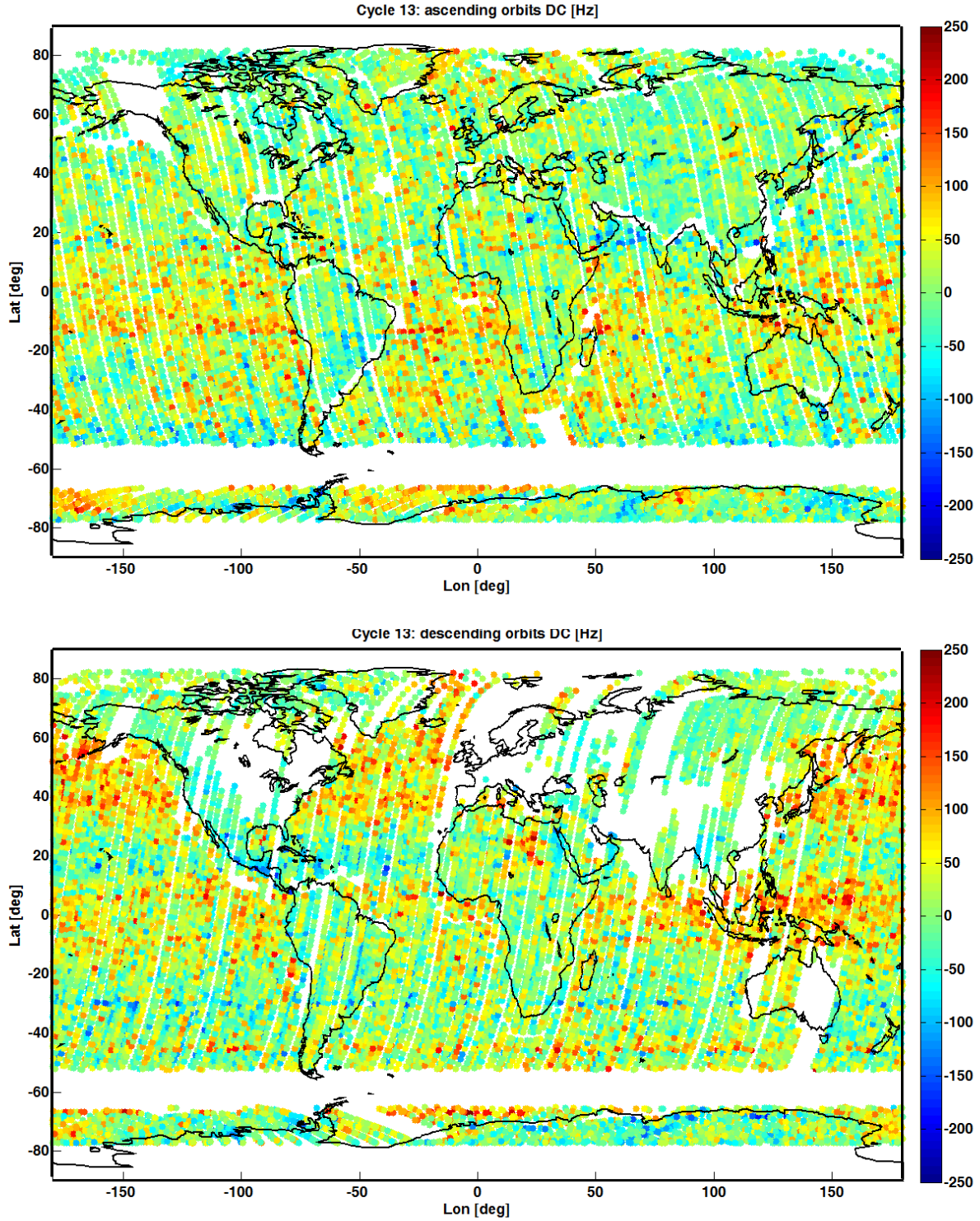

Figure 44. *Doppler shifts estimated from the EWIC products belonging to ERS-2 cycle 13. The figure on the top represents the ascending orbits, while the figure on the bottom represents the descending orbits.*

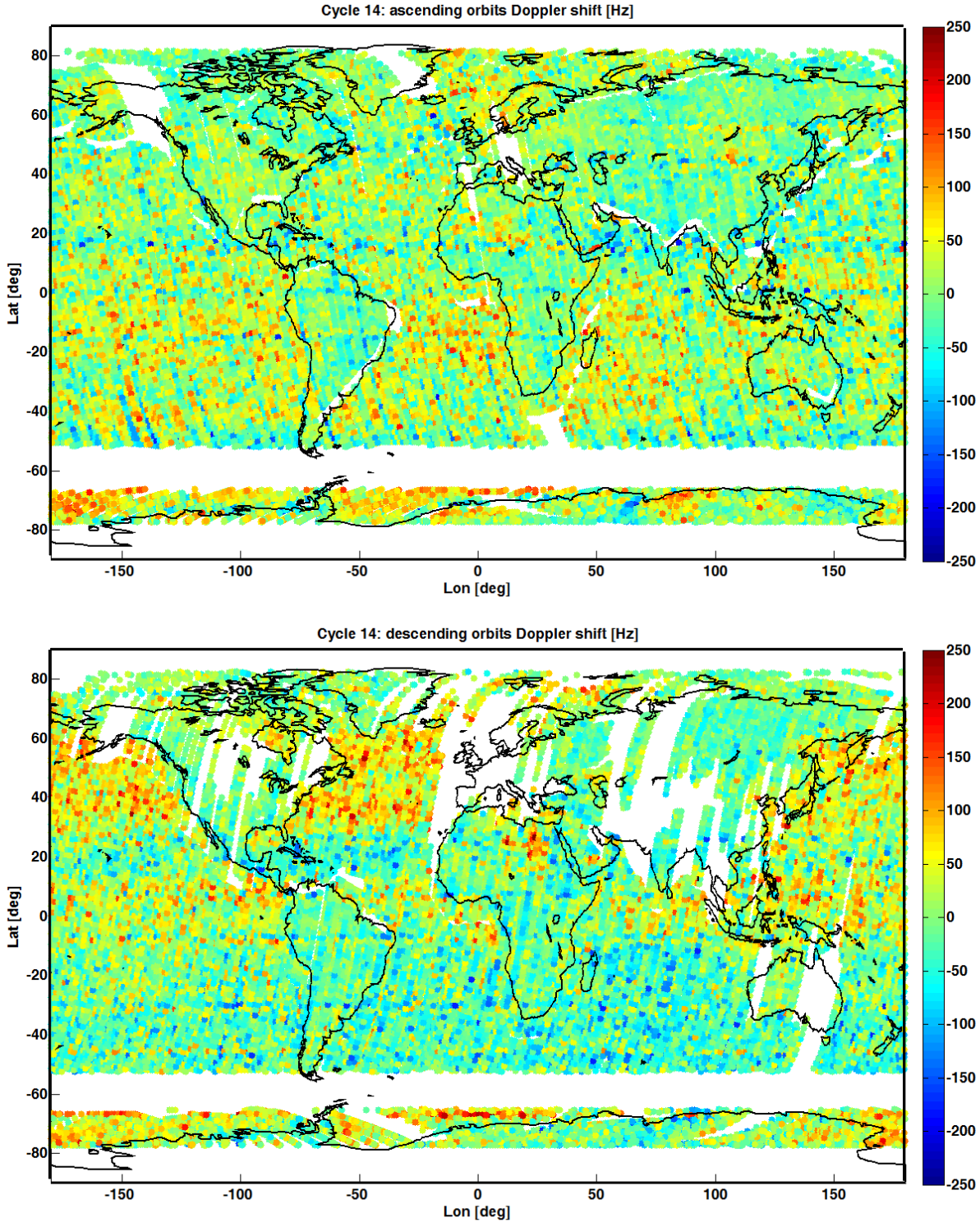

Figure 45. *Doppler shifts estimated from the EWIC products belonging to ERS-2 cycle 14. The figure on the top represents the ascending orbits, while the figure on the bottom represents the descending orbits.*

The ocean currents are not the only element to introduce a Doppler shift in the observed signal: also the interaction between winds and ocean surface can generate a Doppler shift. The Doppler shifts calculated from the data were then corrected for the wind induced contribution, calculated exploiting the empirical model CDOP, which provides the wind dependent Doppler shift from the wind speed and direction with respect to the antenna look direction [RD13] [RD6] (considering a pointing normal to the velocity direction and an incidence angle of 30 degrees). Figure 46 represents the Doppler corrections to be applied, according to CDOP model, to account for wind induced Doppler shifts during EWIC cycle 10. Please note that the represented shifts are of an order of magnitude lower than the Doppler shift estimates represented in the previous figures.

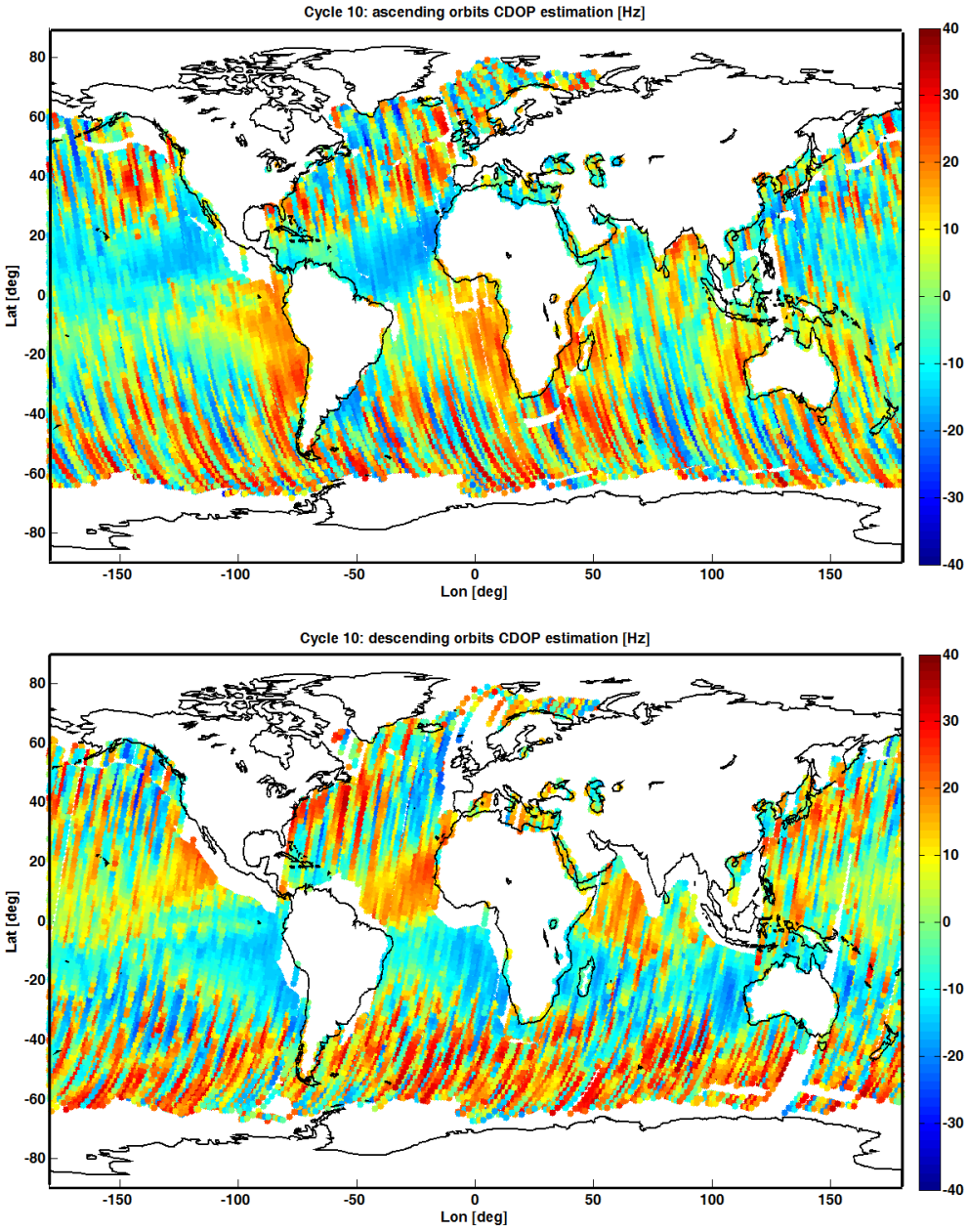

Figure 46. *Wind induced Doppler shifts estimated exploiting the CDOP model. Still land and ice values have been removed.*

Figure 47 shows the Doppler shifts of the 3 EWIC cycles, re-gridded over a regular 1 degree by 1 degree latitude/longitude grid (this means that the resolution cells are bigger near the Equator and smaller near the Poles). The CDOP contribution has been removed prior the averaging operation. The operation was meant to highlight those "geophysical" contributions not dependent on the period of the year. Again the shifts are quite noisy but uniform regions all around the world can be clearly noticed.

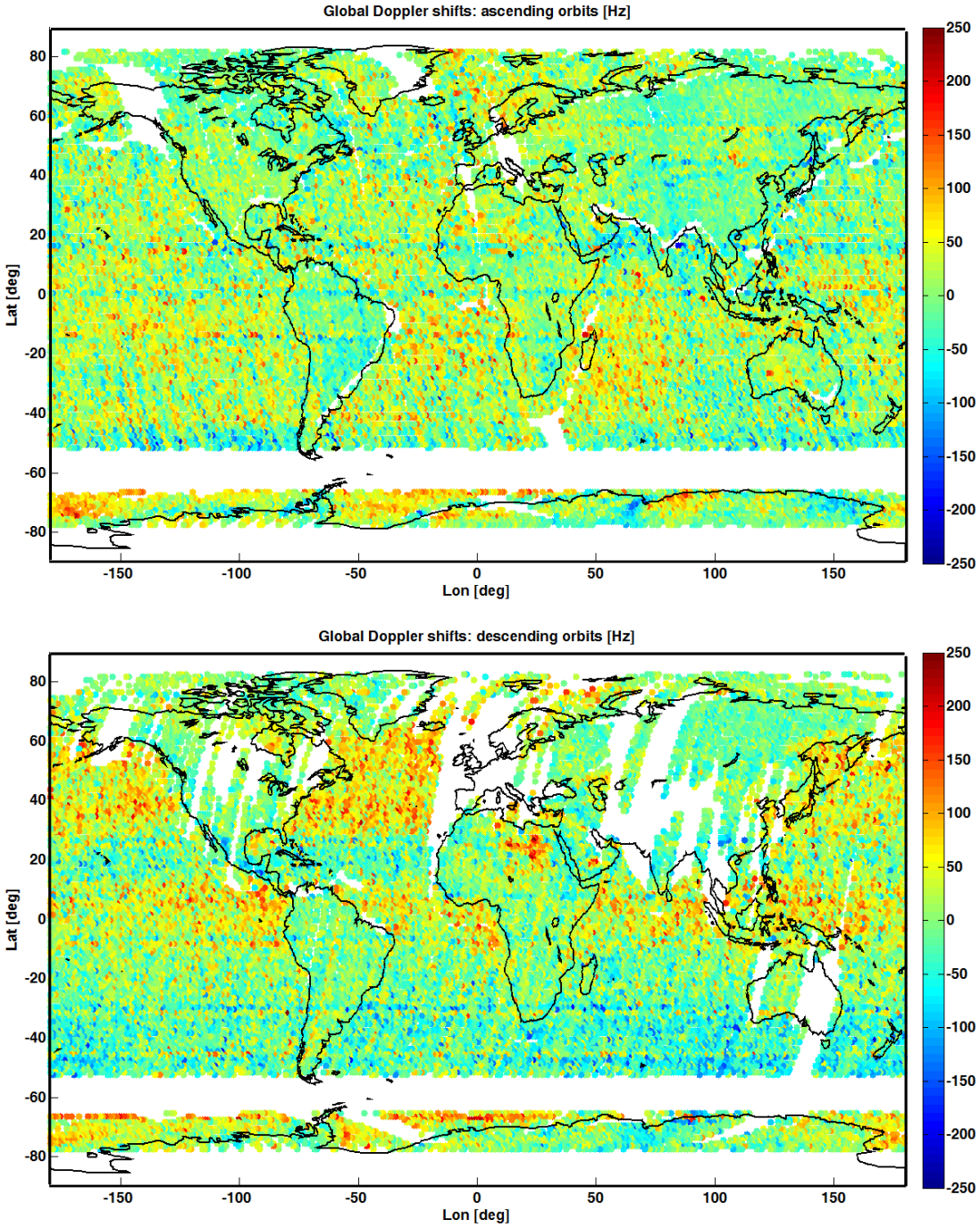

Figure 47. *Corrected Doppler shifts re-gridded over a regular 1 degree by 1 degree latitude/longitude grid. The image on top is for ascending orbits while the image on the bottom is for descending orbits.*

Figure 48 shows, finally, the Doppler shift estimates performed over a portion of the EWIC cycle 13 with the MLS estimation method. As expected the method allows to obtain a better estimation accuracy. The standard deviation (3σ) of the estimates is around 130 Hz, whereas for the ACCC it was around 160 Hz. The reduced WS sampling does not allow to go under the limit of the 100 Hz for the estimation accuracy.

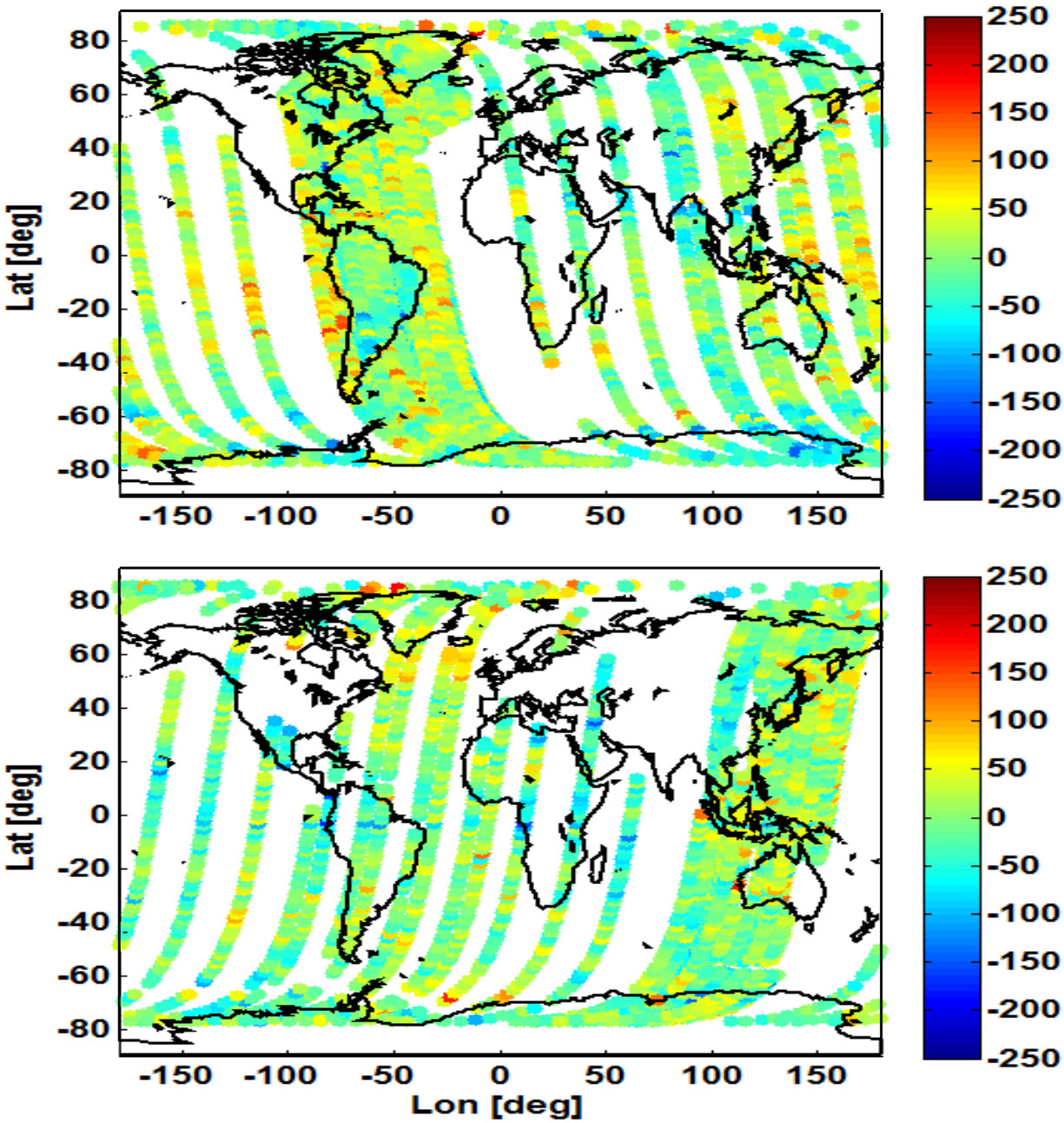

Figure 48. *Doppler shifts estimated from a subset of the EWIC products belonging to ERS-2 cycle 13 with the MLS method. The figure on the top represents the ascending orbits, while the figure on the bottom represents the descending orbits.*

TASK 4000: Provision of recommendation for future scatterometer development

SUB-TASK 4100 - ELABORATION OF CONCEPT IDEA FOR COMBINED WIND FIELD AND SURFACE CURRENT SCATTEROMETER

Monte Carlo simulations

To further study the concept of a scatterometer that combines back-scatter and Doppler information, a separate simulation was performed at KNMI, independent of the CLS simulations. This was based on software available at KNMI that was developed for the earlier rfscat ESA study [RD5]. To allow this the following changes where implemented:

- simple geometry calculations for ASCAT and QuikScat where added, using the method described in section 3;
- the software was interfaced to the new CDOP function to allow generation of simulated Doppler signals. A constant relative noise was simulated, based on a constant Kp value similar to what is done for the back scatter signals;
- the software was interfaced to our genscat modules, to allow wind inversion using combined backscatter and Doppler signals, using the method described in section 3;
- subroutines where implemented to calculate the many Figure-of-Merit numbers, as discussed in section 3.

Using this simulator several simple and more complex tests where done for reference geometries (ASCAT and QuikScat), and for new geometries (ASCAT with added Doppler capability on one or more antennas).

As a first test the ASCAT geometry was simulated as shown in Figure 49. The main parameters used are: Kp=5%, #winds=25.000, WVC index=10 (so distance to nadir of 586 km), WVC size=25 km, input u,v from Gaussian distribution with half width of 5.5 m/s. The result clearly shows the 180 degree ambiguity typically found for scatterometer instruments with this antenna configuration. In addition clearly some extra (3rd and 4th) wind solutions are visible as clouds of dots in between the diagonal lines. For ASCAT geometry these clearly are very symmetric when mirrored along the u or v axis. Figure 50 shows a second comparable simulation result, now using a typical QuikScat geometry. All input settings for the simulator have been kept constant, but since QuikScat also observes the nadir region, the WVC with index 10 is much closer to nadir than for the ASCAT case (distance to nadir is 250 km), so uses limited diversity in azimuth angles.

Altogether the result shows multiple solutions, but the 180 degrees ambiguity does not dominate the possible wind solutions, other angles occur more often for this geometry. In addition the solution clouds clearly are asymmetric for mirroring along the u or v axis. Also a line of solutions at v=0 can be seen, which typically is caused by insensitivity of the system for this specific wind direction.

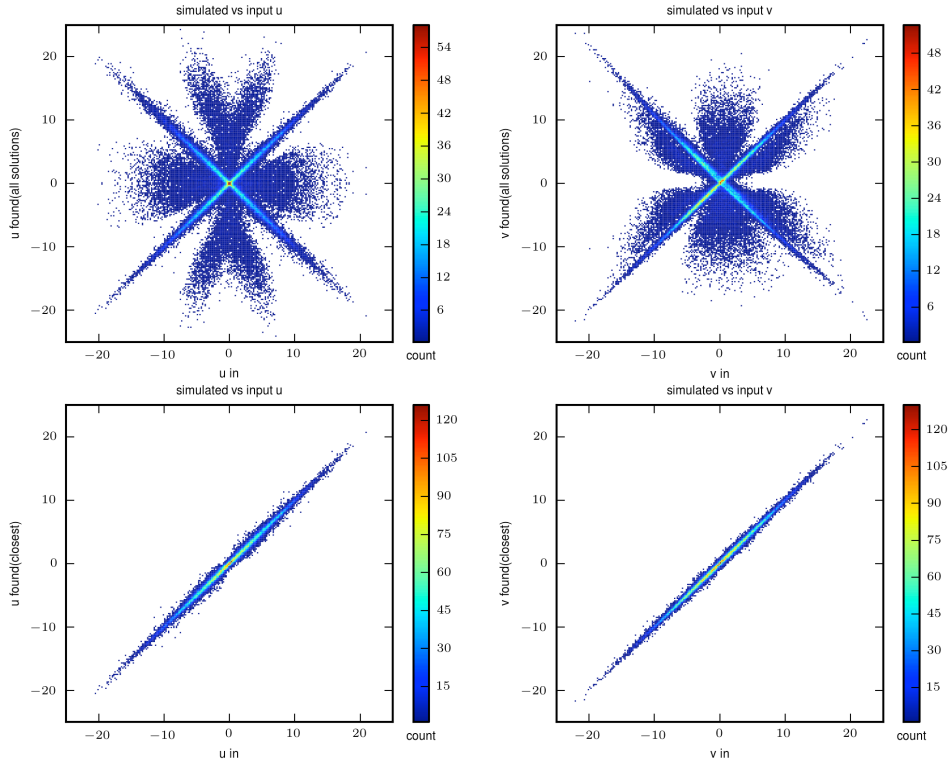

Figure 49: *Basic simulation result showing input and retrieved wind components u (left panels) and v (right panels) for the ASCAT geometry. The upper panels show all found wind results. The lower panels show only the wind results with direction closest to the input wind vector.*

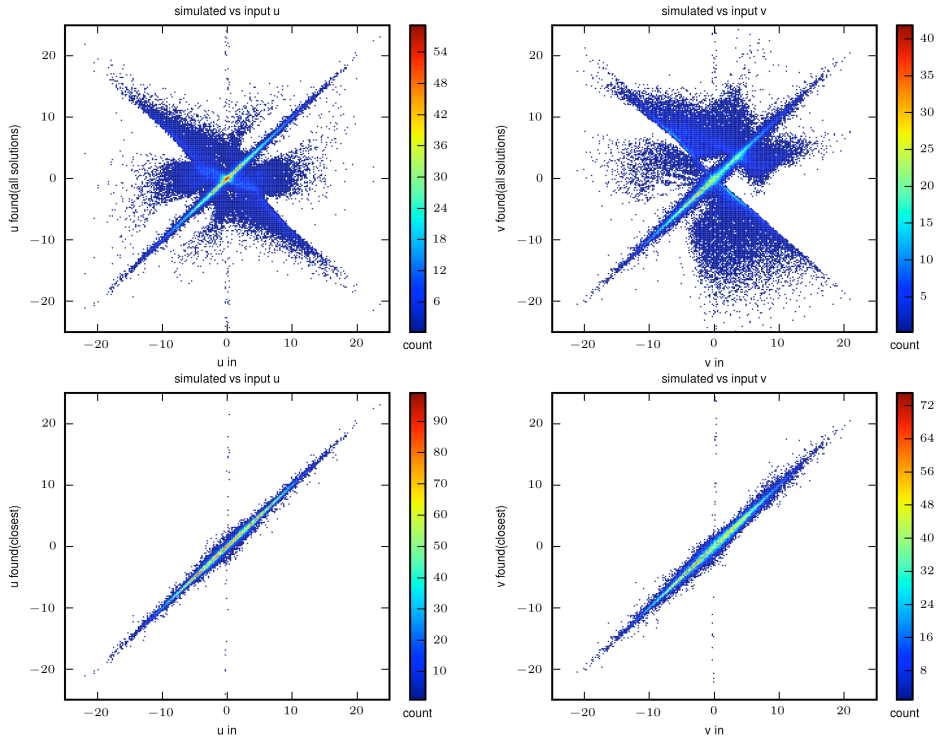

Figure 50. *Comparable simulation results as shown in Figure 49, but now for Quickscat configuration.*

As a next step simulations where done by adding Doppler signal to the mid beam of the ASCAT geometry. This was simulated without ocean current, and with an added ocean current of 0.5 m/s along the v component. Results are shown in Figures 51, 52 and 53. Changes are clearly seen in the distribution of the additional solutions. The clouds of solutions change their shape, additional line shaped clouds appear, and introducing ocean current make these clouds asymmetric. These plots can be created for each WVC along the swath and clearly contain a huge amount of interesting information, but interpretation of them is difficult, and comparing the wind result quality between different systems is not obvious at all. This was solved by implementing the Figure-of-Merit calculations that where explained in section 2.

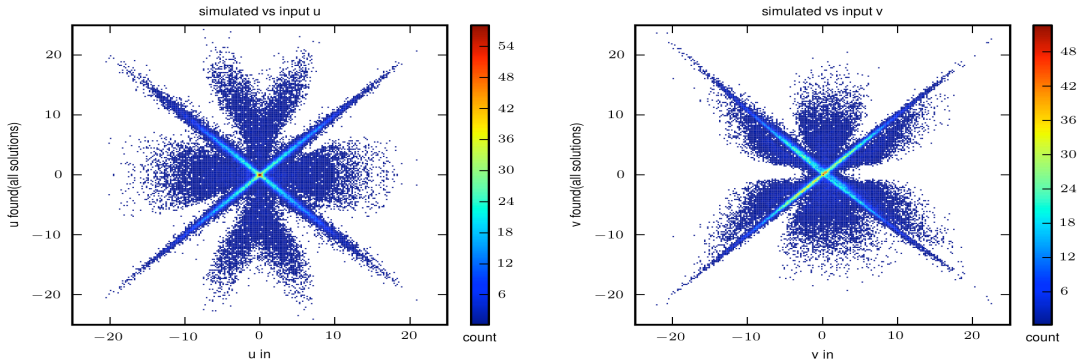

Figure 51: *ASCAT geometry for reference (same as in Figure 49)*

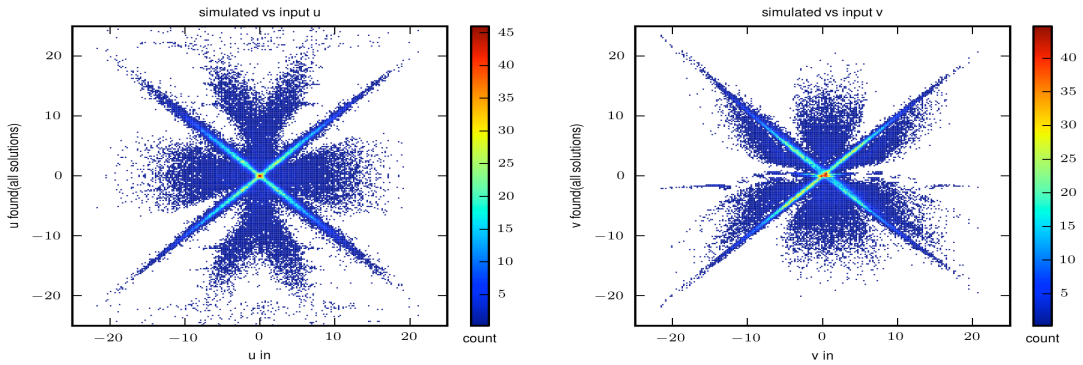

Figure 52: *ASCAT geometry with Doppler capability added to the mid beam*

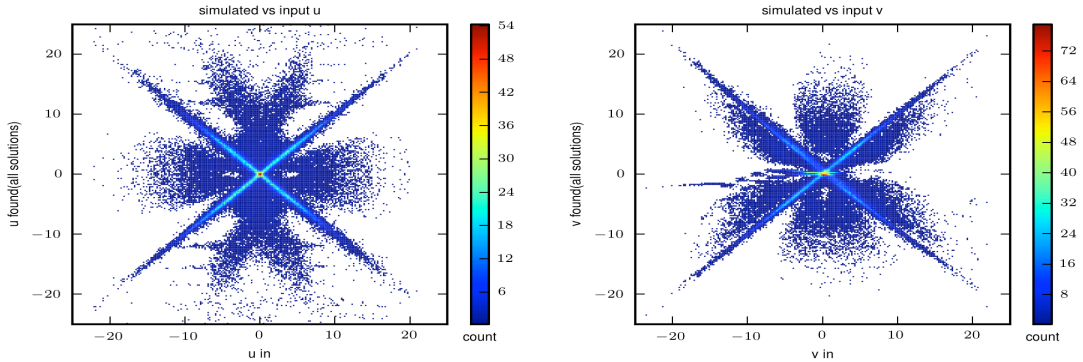

Figure 53: *Same as in Figure 52, but now an ocean current of 0.5 m/s was added*

Figure of Merit results: To condense the simulation results presented above the Figure-of-Merit (FOM) method was used as explained in section 2. Based on 250 simulations to determine the observed wind vector distribution for a given input wind vector, the scan result over the u,v domain for an ASCAT simulation is shown in Figure 54. This again reveals a large amount of detail on the studied system, and is suitable for relative comparisons between different systems. For overall performance assessment these results are condensed into a single number using the Weibull integration method explained in section 0.

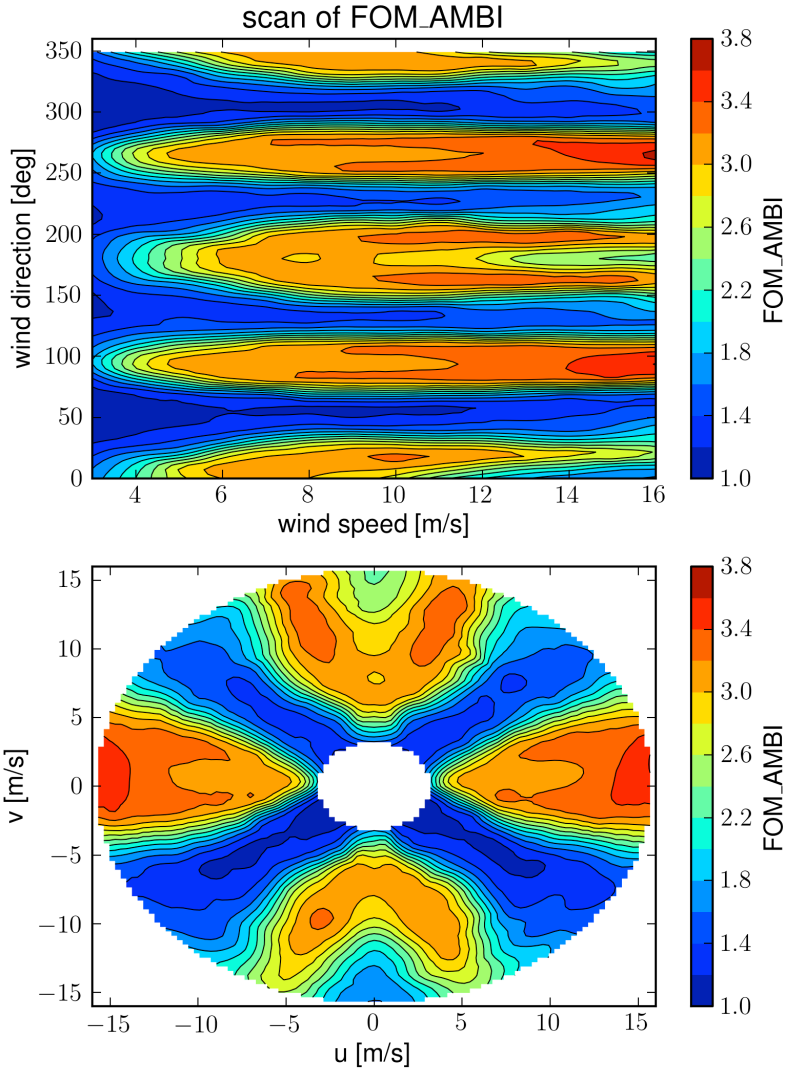

Figure 54: *AMBI FOM for an ASCAT geometry*

This results in nice simple performance curves as a function of swath position, as is shown in Figure 55 for the ASCAT simulation and in Figure 56 for the Quickscat simulation. The 2 composite figures shows 8 distinct simulations for 8 different noise (Kp) settings. The upper left panel gives the VRMS FOM, the upper right plot the AMBI FOM, the lower left plot the wind speed FOM and the lower right panel the wind direction FOM. Closer to zero is a better result for all these FOM performance numbers. Clearly the wind direction FOM displays only noise, which is caused by the nice symmetry of the ASCAT results. From the AMBI FOM it is clear that noise has a significant impact on the shape of the curves as well. For low noise

levels, measurements close to nadir have better quality than measurements further away, but for high noise levels the situation is clearly reversed.

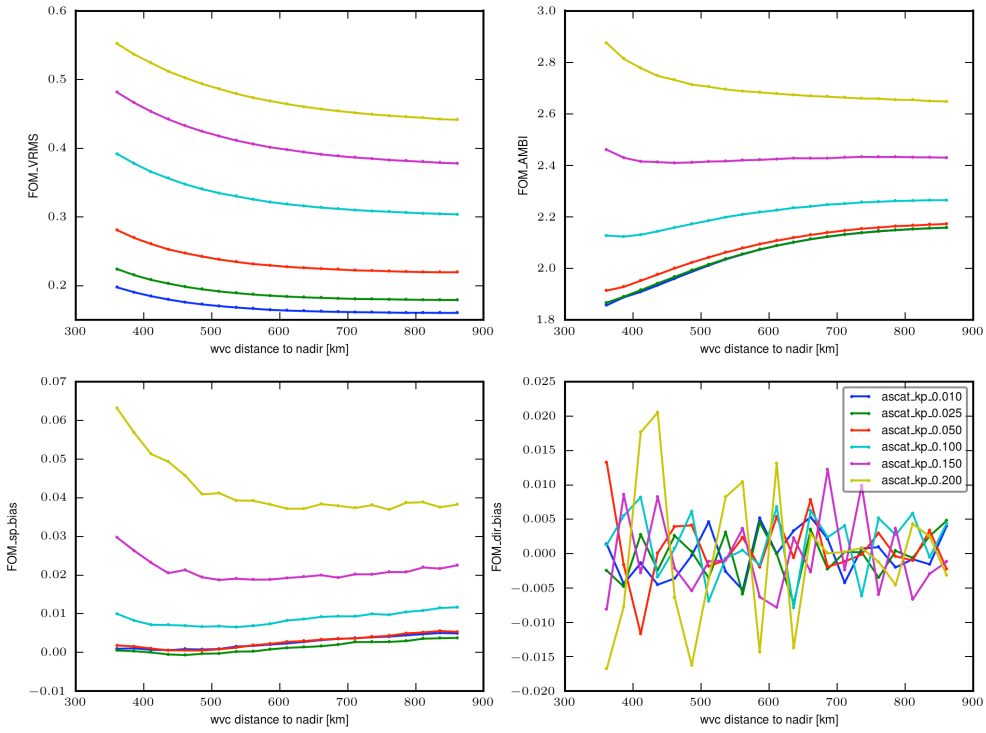

Figure 55: *FOM results for an ASCAT simulation for a range of Kp values.*

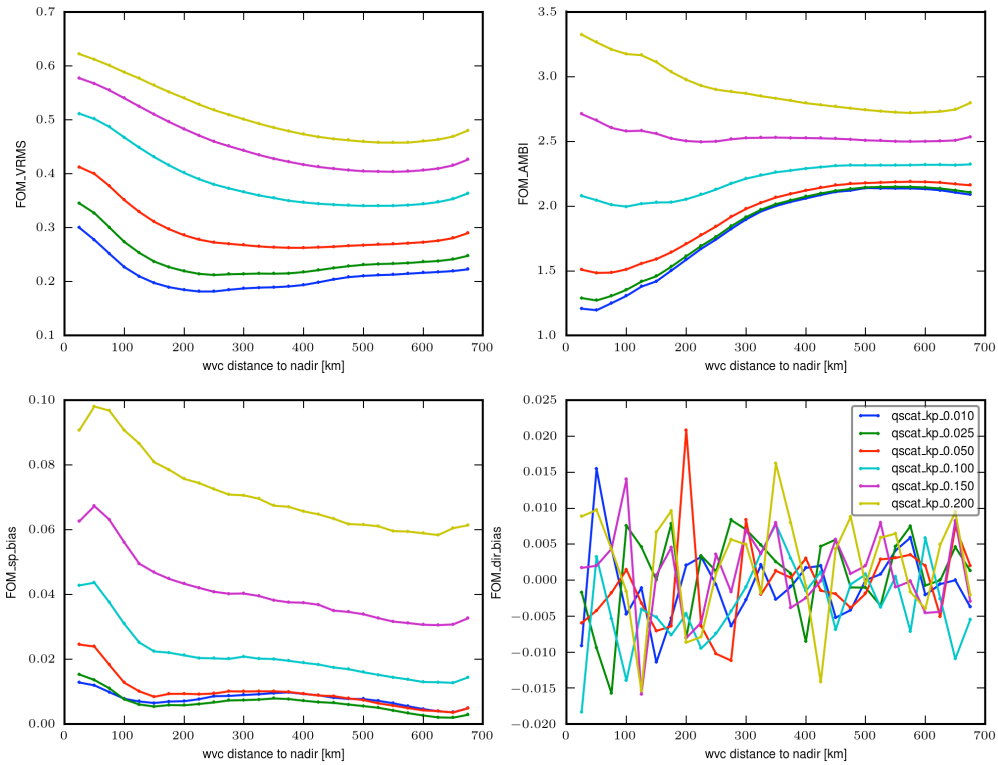

Figure 56*: FOM results for an QuikScat simulation for a range of Kp values.*

A first Dopscat simulation result is shown in Figure 57. This simulation used ASCAT geometry with Doppler capability added to the mid-beam and Kp=10%. In order to study the effect of the weight used to combine the backscatter and Doppler information in the wind retrieval routine, a scan over 7 orders of magnitude for this setting was performed (inverse of weight was varied from $1x10^2$ up to $1x10^8$). Clearly the smallest 4 values give unwanted high FOM numbers for 3 out of 4 performance scores.

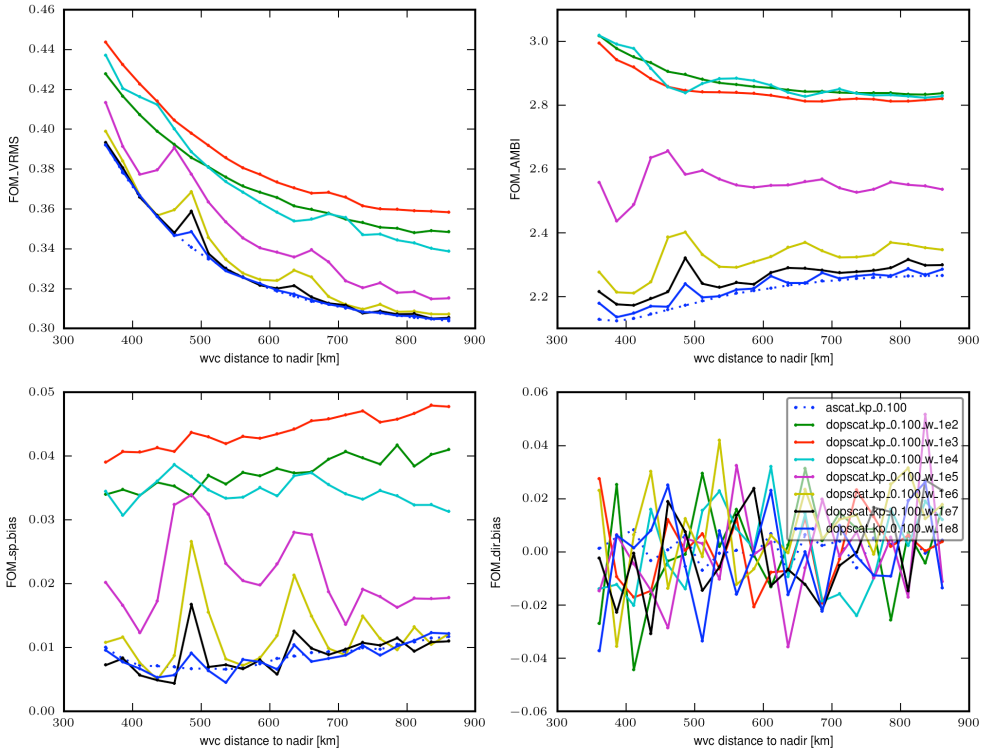

Figure 57: *FOM results for a Dopscat simulation based on adding Doppler capability to the ASCAT mid beam for Kp=10% and a range of weight values. For reference the ASCAT result for Kp=10% has been added (blue dotted line).*

For actual use during comparison of different systems a weight of $1x10^6$ was chosen (shown as the light green line), which results in clear changes from the ASCAT curve at certain WVC's only. The merit of a Doppler dominated retrieval is clearly lower than the merit of a backscatter dominated one. Moreover, from these results it also is very clear that there is no weight setting that results in significantly better performance than the original ASCAT geometry. This is a sign that the retrieval procedure is suboptimal and may be improved, once CDOP GMF and noise characteristics of a prospective instrument become clearer.

A next simulation result shows the case of two Doppler signals added to the ASCAT geometry, at the fore and aft beam (see Figure 58). The results are similar for the 4 smallest values of the inverted weight. However the remaining results are clearly better. The changes around 500 and 650 km are much less pronounced and the FOM curves seem much smoother. This can be attributed to the fact that this system has perpendicular Doppler measurements, and thus samples both Doppler components leading to much more regular results. Again the ASCAT result is over plotted and no setting for the weight was found that improves upon the ASCAT performance (except maybe for the wind speed FOM, although it is not obvious that the difference is significant here).

As a third test case a system was simulated based on ASCAT with Doppler capability added to all 3 beams. The result if shown in Figure 59. The results fall in between the 1 and 2 antenna Doppler results shown in Figures 57 and 58. In addition the AMBI FOM seems to be improved for the lowest 2 values of the inverse weight, but since the speed bias and VRMS FOMs are still very bad for these settings it is assumed that this is more a coincidence rather then real improvement of the system. Finally the simulation results are inter-compared in Figure 60.

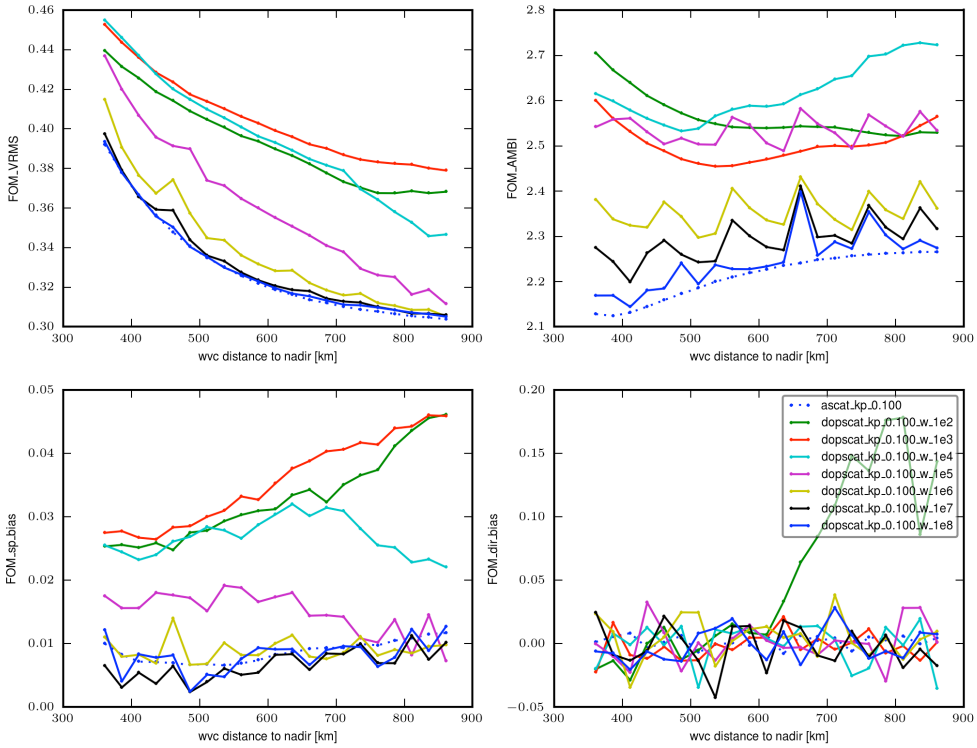

Figure 58: *FOM results for a Dopscat simulation based on adding Doppler capability to the ASCAT fore and aft beam for Kp=10% and a range of weight values. For reference the ASCAT result for Kp=10% has been added (blue dotted line).*

All simulations where done using Kp=10%. The 3 different Dopscat cases use an inverse weight of $1x10^6$. The purple line shows the QuikScat result extending to nadir, the dotted blue line shows the ASCAT result. The other 3 lines show the 3 different Doppler systems. Clearly the results depend very much on the chosen FOM performance indicator. For quikScat the VRMS and wind speed FOM's show poor performance near nadir and these have most practical relevance, but the AMBI FOM shows improved performance near nadir, compared to the outer swath performance of the same instrument. The ASCAT and Dopscat instruments have better VRMS performance in the outer swath and similar performance for the AMBI FOM in the outer swath compared to the QuikScat instrument. Again it is very clear that none of the Dopscat cases outperforms the ASCAT instrument, regardless of the FOM chosen. As indicated earlier in this report, a more optimal retrieval procedure may improve combined Doppler and backscatter results. Recall from earlier sections that optimal retrieval procedures require established sensitivity information from an improved CDOP GMF and geometry and noise characteristics of a prospective instrument.

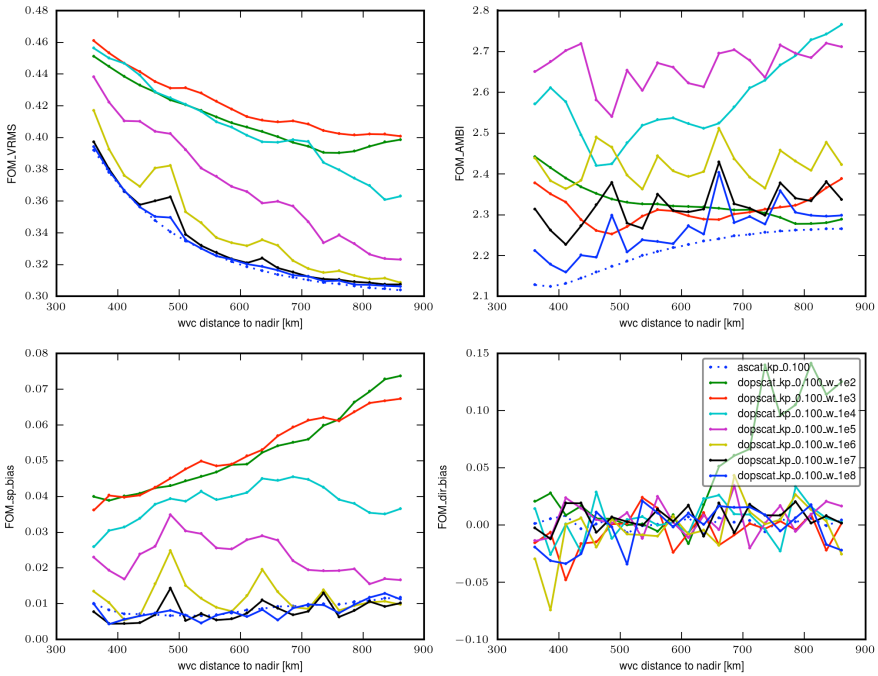

Figure 59: *FOM results for a Dopscat simulation based on adding Doppler capability to all the ASCAT beams for Kp=10% and a range of weight values. For reference the ASCAT result for Kp=10% has been added (blue dotted line).*

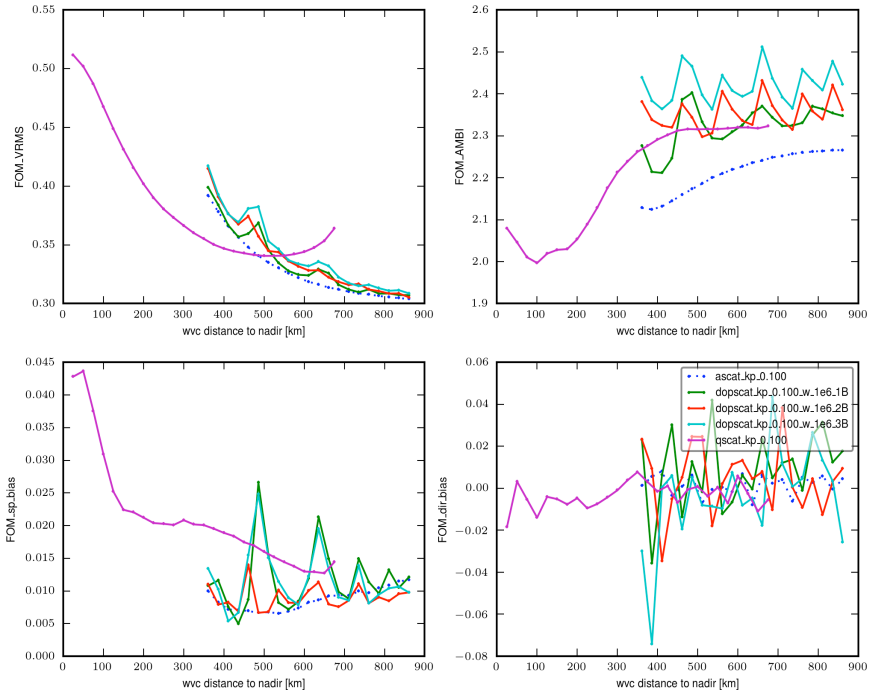

Figure 60*: FOM results for different instrument configurations all using Kp=10%. For all Dopscat cases using a weight of was used.*

Doppler estimation on simulated data: the dual-chirp concept

The results on the EWIC products, presented in the previous section, showed that the non-optimal ERS-2 Wind Scatterometer acquisition parameters did not allow to obtain a Doppler estimation accuracy better than 100 Hz. Furthermore the Doppler estimates were obtained at a very coarse resolution of 250 km along-track and 400 km across-track. The Doppler shift estimator developed for the ERS Wind Scatterometer data exploited the fact that rectangular monochromatic pulses were transmitted. The received range spectrum presented a clear peak allowing the Doppler shift estimation. On the contrary new Scatterometers transmit LFM pulses in order to reduce the emitted peak power and increase across-track resolution. Unfortunately no data from LFM sensors were available for the study and an ad-hoc simulator was implemented by CLS to cope with this problem [RD18]. The methods and results proposed in the next sections are always referred to the simulated data generated with CLS simulator.

The Doppler shift estimation over LFM data is very complicated because the Doppler shift is usually very reduced w.r.t. the system bandwidth and the pulse spectrum is very flat. Furthermore LFM pulses are affected by the so called range-Doppler coupling effect: after pulse compression Doppler shifts and time delays effects cannot be distinguished, making the Doppler shift estimation over standard scatterometer data more complicated. However the range-Doppler coupling effect can be exploited for Doppler estimation, as proposed for instance in [RD19] by exploiting the fact that its effects are opposite for chirps with opposite rates. For this reason we propose a system transmitting dual-chirps (i.e. the sum of two chirps with opposite rate). The Doppler estimation will be performed by measuring the relative shift between the two obtained range compressed images.

Pulse radar ambiguity function: In pulsed radar signal processing, an ambiguity function is a two-dimensional function of time delay and Doppler frequency showing the distortion of a returned pulse due to the receiver matched filter and to the Doppler shift of the return from a moving target. The ambiguity function is determined only by the properties of the pulse and the matched filter and it is defined as [RD20]:

$$\chi(\tau, f) = \int_{-\infty}^{+\infty} s(t)s^*(t+\tau)e^{-j2\pi f t}dt \qquad (4.1)$$

where s is the transmitted pulse τ is the delay and f is the Doppler shift.

A constant envelope LFM pulse has an ambiguity function skewed in the delay-Doppler plane. Slight Doppler mismatches for the LFM pulse do not change the general shape of the pulse and reduce the amplitude very little, but they do appear to shift the pulse in time. Thus, an uncompensated Doppler shift changes the target's apparent range; this phenomenon is called range-Doppler coupling. The ambiguity function of LFM pulses with opposite chirp rates are skewed in opposite direction, meaning that the introduced delay has an opposite sign. While one return is delayed the other one is anticipated of the same quantity. Figure 61 shows the ambiguity function for two LFM pulses with opposite rates.

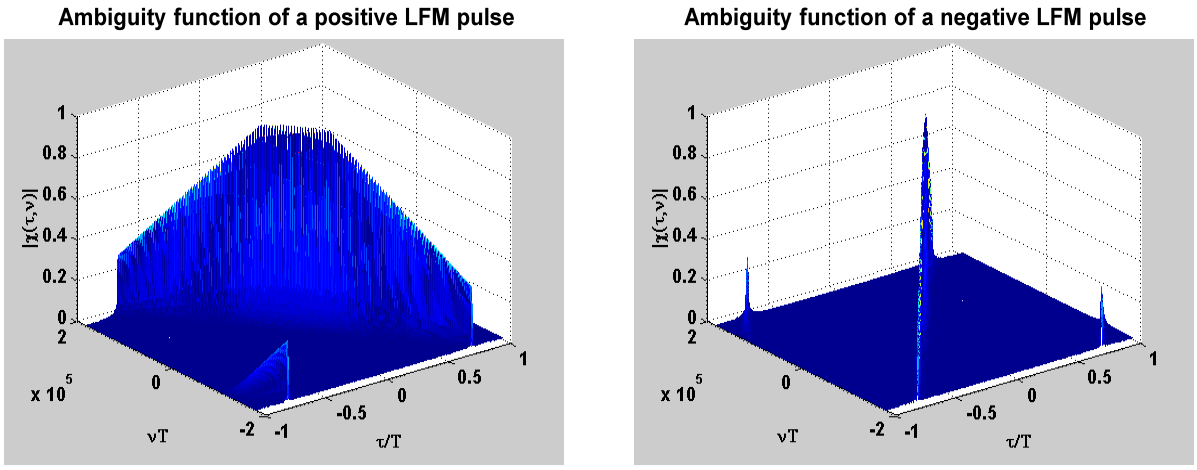

Figure 61. *Ambiguity functions for two LFM pulses with opposite rates. The functions are skewed in opposite directions*

The introduced delay is proportional to the Doppler shift f and inversely proportional to the chirp rate K_p :

$$\tau = \frac{f}{K_p} \tag{4.2}$$

Figure 62 shows the relative time delay between two LFM pulses with opposite rates subjected to a common Doppler shift. By estimating the delay and inverting equation (4.2) it is possible to retrieve the Doppler shift affecting the received data.

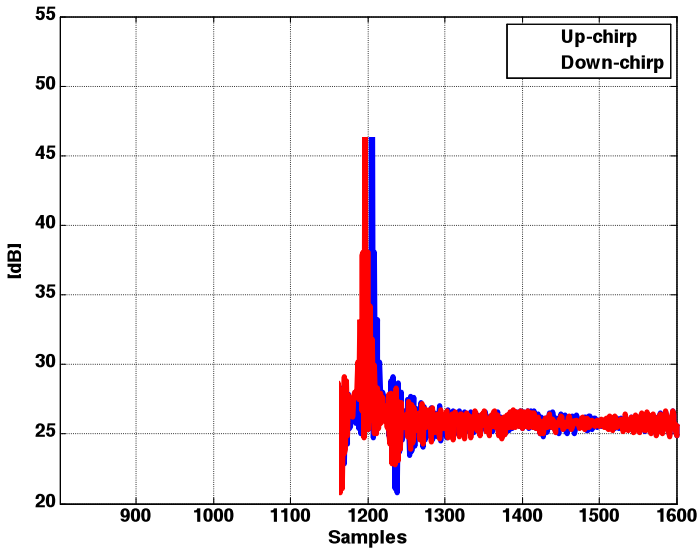

Figure 62. *Relative shift between two LFM pulses with opposite rates subjected to a common Doppler shift*

Doppler estimation algorithm: The proposed Doppler estimation algorithm exploits the above mentioned range-Doppler coupling effect to retrieve the Doppler shift affecting the received Scatterometer data. The concept is very simple, instead of the standard LFM pulse, the sum of two LFM pulses with opposite rates will be transmitted. The processing scheme for the received raw data is illustrated in Figure 63.

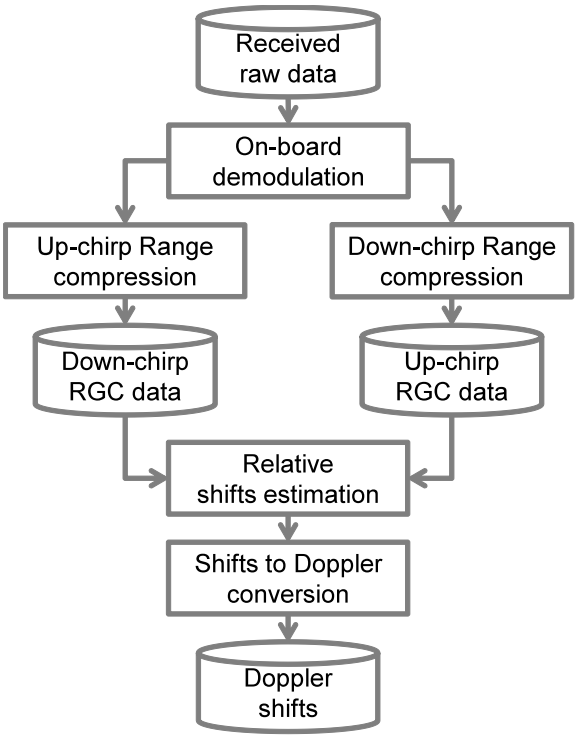

Figure 63. *Dual-chirp Doppler estimation algorithm flow-chart*

The following processing steps are performed:

1. On-board demodulation: this step is required, as for ERS-2 Scatterometer (see Section 3.1), to cope with the huge Doppler shift affecting the Scatterometer squinted beams which, if not compensated, would translate the received data outside the receiving filters bandwidth.
2. Range compression: the received raw data are range-compressed with both the chirps (up and down) and two different range compressed images are obtained. The received raw data from a single point target in the scene can be modeled as:

$$s(t) = g(t - t_o)\exp(j2\pi f_D t) + n(t) \tag{4.3}$$

where t_0 is the actual delay of the target, f_D is the Doppler shift affecting the target, $g(t)$ is the transmitted waveform (sum of up and down LFM chirps with opposite rates) and $n(t)$ is the AWGN. In the equation we have neglected the complex amplitude of the target and the attenuation factor, which are ineffective to our purposes.
After range compression with matched filters the following signals are obtained:

$$\begin{aligned} s_{UP}(t) &= \mathrm{sinc}\left[B(t - t_0 - \tau_D)\right] + w_{DOWN}(t) + n_{UP}(t) \\ s_{DOWN}(t) &= \mathrm{sinc}\left[B(t - t_0 + \tau_D)\right] + w_{UP}(t) + n_{DOWN}(t) \end{aligned} \tag{4.4}$$

where B is the bandwidth of the considered chirp, τ_D is the Doppler induced delay (opposite in the two cases), $w_{DOWN}(t)$ and $w_{UP}(t)$ are the interference signals originated by the presence of the opposite chirp in the transmitted waveform and $n_{UP}(t)$ and $n_{DOWN}(t)$ are the effect of the noise convolution with the matched filters. It can be proven and is intuitive that the interference signal is again a LFM chirp with double rate w.r.t. to the originally transmitted pulse. The extension to the distributed case is then straightforward: the obtained signals will be the integral over the whole acquired scene of the signals in the previous equation.

3. Relative shift estimation: the principle of the proposed Doppler estimation method is to measure the relative delay between the obtained up and down signals and readily convert this delay into a Doppler shift value. This operation is performed according to the well-known cross correlation technique which is used, for instance, for the coregistration of interferometric SAR images. The two signals obtained with the range compression operation are detected and the cross-correlation is computed in the frequency domain. The relative shift is given by the location of the maximum of the cross-correlation function. To increase the accuracy of the estimation process an oversampling of a factor 8 in the frequency domain can be applied. Figure 64 shows a very simple example of the technique: on the left two delayed pulses are shown while on the right the cross-correlation with the maximum located at the value of the relative delay is represented.
4. Shifts to Doppler conversion: the estimated delay values are converted into Doppler shifts according to:

$$f = 2\tau K_p \tag{4.5}$$

directly derived from Equation (4.2), where the 2 factor accounts for the fact that both the chirps are affected by the same delay in opposite directions.

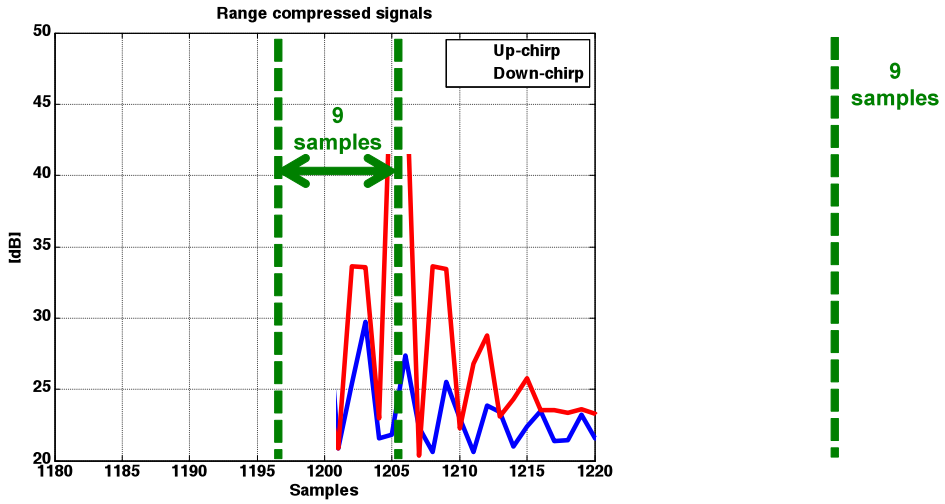

Figure 64. *Cross-correlation function (on the right) of two delayed pulses. The peak is located exactly at the relative shift between the two pulses.*

The whole acquired image can be divided into blocks in order to obtain along and across track variant Doppler shift estimates with the desired resolution and accuracy.

Doppler estimation results on simulated data: This section presents the main results obtained applying the proposed Doppler estimation technique on Wind Scatterometer simulated datasets. Each dataset consisted in 3 right-looking beams of an ASCAT-like scatterometer. 64 datasets have been produced by CLS for the Doppler estimation technique validation. The reference scenario was always the same with different conditions of SNR and on-board Doppler demodulation errors.

The following figures show the results obtained for 16 of the datasets for the squinted beams (after beam in Figure 65 and fore beam in Figure 66). No plots were generated for the mid beam since only a couple of estimates along range were possible due to the reduced across-

track beam size w.r.t. the squinted beams. For each beam all the along-track estimates (128 along-track lines per beam) have been averaged to increase the estimation accuracy and obtain an across-track dependent vector of Doppler estimates. The four plots represent different SNR values whereas the colors represent different on-board Doppler demodulation errors. The black line is the expected geophysical Doppler shift.

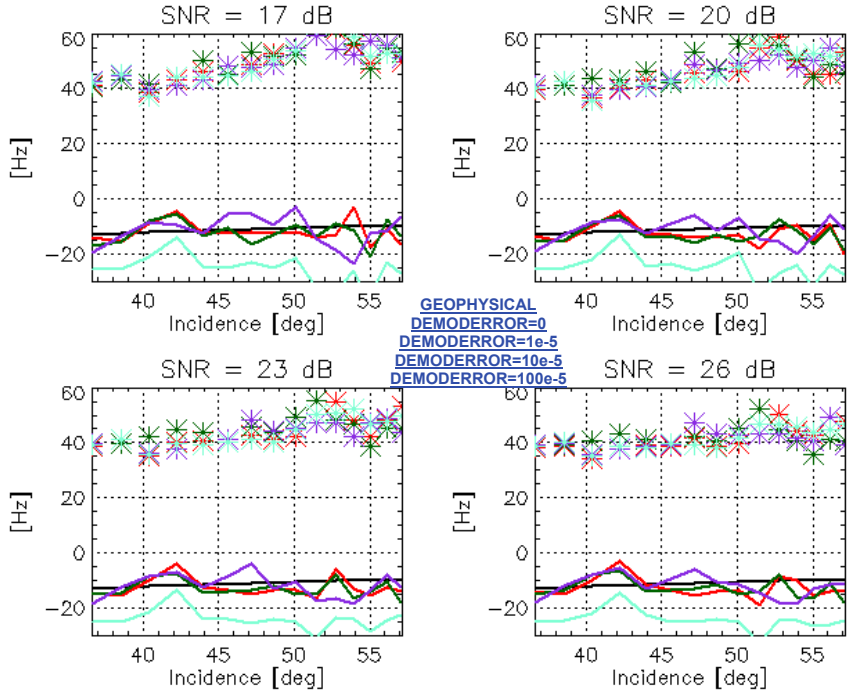

Figure 65. *Doppler shifts estimation results for different conditions of SNR and on-board Doppler demodulation errors for the after beam.*

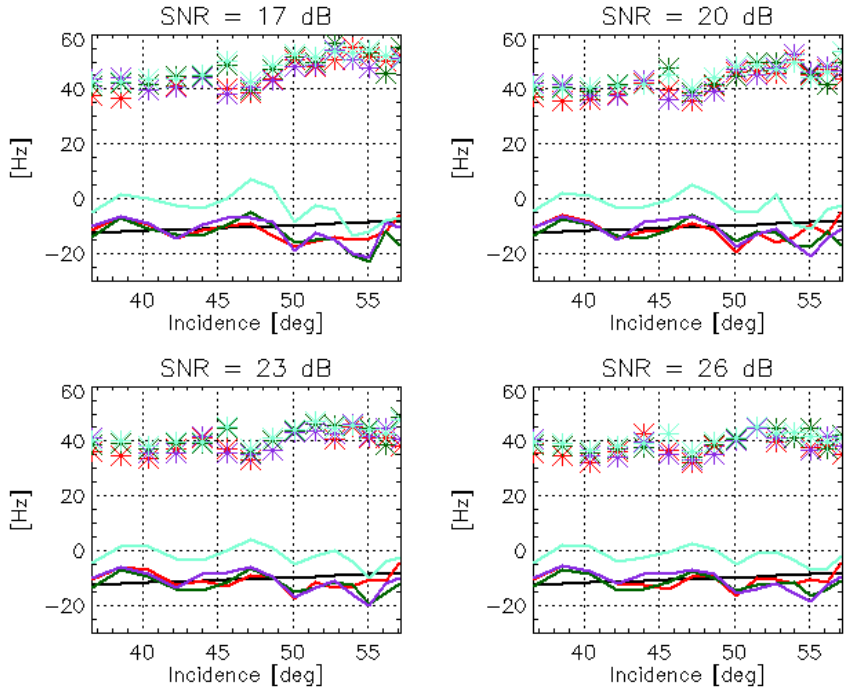

Figure 66. *Doppler shifts estimation results for different conditions of SNR and on-board Doppler demodulation errors for the fore beam.*

The results clearly show that, as expected, there is a clear correlation between the SNR and the Doppler estimation accuracy. For high SNR an estimation accuracy around 40 Hz is obtained. This value could be further improved by increasing the across-track estimation window size. This in turn would results in a coarser resolution of the across-track estimates. Another possibility could be to average several estimates in time (e.g. passages of the scatterometer over the same region in different days). This would improve the accuracy at price of a coarser time resolution in the estimates. The on-board Doppler demodulation error has also a direct impact on the quality of the Doppler shifts estimates. In particular at the increase of the error value a bias in the estimates is introduced (as can be noticed by the light blue line in the plots). It is interesting to note that the bias has opposite sign for the fore and after beams. Figure 67 shows two scatter plots representing the Doppler estimates bias and accuracy dependency on SNR. As described above the accuracy is strongly dependent on SNR whereas the bias is more affected by the on-board Doppler demodulation error.

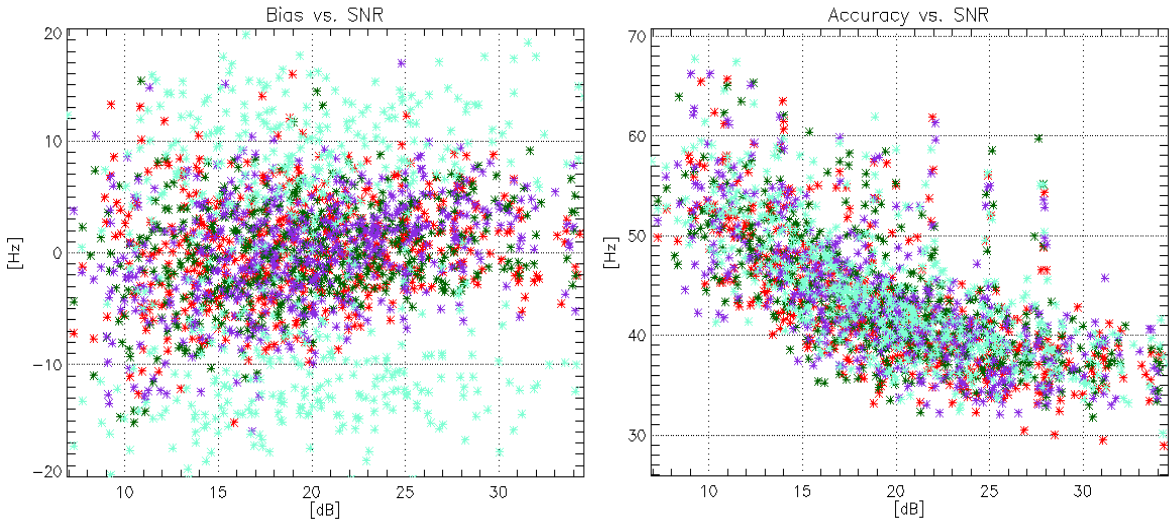

Figure 67. *Scatter plots of Doppler estimates bias and accuracy w.r.t. the SNR. The different colors represent different on-board Doppler demodulation errors.*

Dual-chirp concept trade-offs: The results presented in the previous section have been obtained transmitting the sum of two fully overlapped (both in time and frequency) chirps. This solution allows to maximize the correlation between the received up and down signals, since the scene imaged by the two chirps is exactly the same. Nevertheless this approach is non-optimal from a transmission system point of view since the obtained transmitted wave form presents a very quickly time-varying amplitude, which could be a problem for on board amplifiers. Indeed the transmitted signal is:

$$g(t) = \exp\left(j2\pi K_p t^2\right) + \exp\left(-j2\pi K_p t^2\right) = 2\cos\left(2\pi K_p t^2\right) \quad -\frac{T_s}{2} < t < \frac{T_s}{2} \qquad (4.6)$$

where T_s is the pulse duration Figure 68 shows the amplitude of the sum of two chirps with opposite rates (blue line). The green and red lines represent the unwrapped phase of the chirps (axis on the right of the plot). Please note that the transmitted signal is purely real since the phase of the two pulses always compensate each other. The problem related on the board amplifiers could be solved by transmitting the chirps in time division:

$$g(t)=\begin{cases}\exp\left(j2\pi K_p\left(t+\frac{T_s}{4}\right)^2\right) & -\frac{T_s}{2}<t<0\\ \exp\left(-j2\pi K_p\left(t-\frac{T_s}{4}\right)^2\right) & 0<t<\frac{T_s}{2}\end{cases} \tag{4.7}$$

where T_s is again the pulse duration but each pulse occupies only half of the transmitted wave form. This means that for fixed pulse duration and chirp rates the bandwidth of the system would be halved. In this case the transmitted waveform would have constant amplitude.

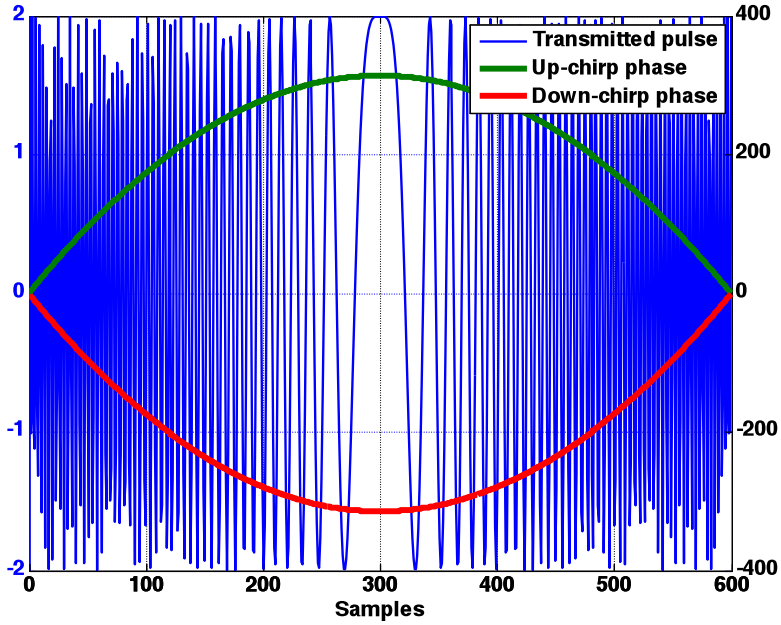

Figure 68. *Transmitted waveform in case of fully overlapped chirps and unwrapped phase of the single pulses.*

The main issue related to this approach would be that the two chirps would see two slightly different ground scenes, reducing the performances of the cross-correlation technique. This would not be a problem at all for scenes with coherence times much higher than the pulse length (e.g. land scenes), but for ocean scenes the impacts on the Doppler estimation accuracy should be assessed. A possible solution would be to reduce as much as possible the pulse duration and, at the same time, increase the chirp rate to maintain the system bandwidth fixed. This solution would have of course an impact on the estimation accuracy. Indeed from eq. (4.2) to increase estimation accuracy we would like to maximize the effects of the Doppler shifts in terms of delay. This is possible only by reducing the chirp rate which is at the denominator of the equation. This means that the system parameters shall be selected very carefully in order to make the proposed Doppler estimation technique effective.

Sub-Task 4200: Conclusion and Recommendation.

From the ERS collocation results presented in section 3 it was revealed that no correlation exist between the model data and the ERS Doppler information (provided by ARESYS). Moreover, from the wind retrievals performed on the CLS simulation results presented in section 3 it is concluded that:

- A clear and significant bias up to 2 m/s in wind speed is found, which increases with decreasing SNR, while at the same time the rms error of the wind speed difference does not change. It is suspected that the problem is related to the addition of the geophysical noise term in the CLS simulator, because the signals without geophysical noise do not display this bias;

- A much smaller bias in both wind speed (up to 0.2 m/s) and wind direction (up to 3 deg) is observed even when a clean signal without any noise is processed. The reason for this problem is not yet clear and needs more debugging effort;

- The demodulation error rate has no relation to the retrieved wind quality at all.

From the Monte-Carlo simulation results presented in section 0 the following conclusions and recommendations can be noted:

- Assuming a value for the relative noise (Kp) it is possible to calculate Figure-of-Merit numbers that allow comparing overall performance for different scatterometer instrument configurations;

- From comparing different systems, it is clear that adding Doppler capability to the fore and aft beam, and thus sampling two perpendicular Doppler components, gives the best performance results;

- No configuration was found in which adding Doppler information improves upon the ASCAT instrument performance;

- It is recommended that a weight of $1x10^{-6}$ or less should be used when combining backscatter and Doppler information in the same MLE;

- It is also clear that this first simple MLE implementation is probably not optimal; more research is needed to investigate if the results may still be improved. The Doppler GMF sensitivity, the Doppler instrument geometry and the measurement noise characteristics are at interplay in defining an optimal Bayesian retrieval procedure. Given the different non-linearity of the sensitivities of backscatter and Doppler measurements to wind speed and direction, it is probably favorable to define separated backscatter and Doppler retrievals, which are subsequently optimally combined in the geophysical domain (of wind and ocean current vectors);

- Finally, the CDOP functions itself do not seem optimal to us yet. The current definitions allow two positive wind speed solutions for a given wind direction as result of a given input Doppler shift for the VV case. Similarly, they also allow a positive and a negative wind solution for a given wind direction as result of a given Doppler

shift for the HH case. It seems unlikely that these conditions are real, so we expect further refinement of these fitted GMF functions will be possible. Clearly more verification and validation work is needed here.

Furthermore, the investigation and definition of new algorithms for the accurate retrieval of the Doppler Information from scatterometer data focused on two different kind of datasets:

- Raw data (although rather limited) from the Wind Scatterometer on board of the ERS-2 sensor (EWIC). The sensor was selected since it was the only one providing complex data on-ground (the Doppler shift estimation is embedded in the phase of the data);

- Simulated scatterometer data generated by CLS.

Three different Doppler shift estimation methods were developed for the EWIC data:

- Peak detection: directly looking for the position of the maximum of the received across-track signal spectrum;

- Adjacent Cross Correlation Coefficient: indirectly looking for the position of the maximum of the received signal spectrum, by considering the across-track auto-correlation function of the received signal;

- Minimum Least Squares: looking for the shift minimizing the quadratic difference between the received across-track signal spectrum and the signal spectrum model, calculated considering the acquisition geometry and the on board processing (demodulation and anti-aliasing filtering).

The ACCC and the MLS showed better accuracy and were selected for the prosecution of the analysis. In particular the ACCC, which has a very reduced computational cost, was exploited to perform the Doppler shift estimation over three full EWIC cycles (#10, 13 and 14). Due to the poor knowledge of the sensor attitude, the Doppler reference function, to be subtracted from the estimates to isolate the "geophysical" contribution, was defined as the average of each cycle for the land acquisitions. The Doppler shift estimates were averaged to obtain a resolution of about 250 km for the along-track direction and 400 km for the across-track direction. The obtained results present an estimation accuracy (3σ) of about 160 Hz, which is far too high to allow a correct global ocean surface current mapping. The reduced accuracy is due to both the very reduced sampling of the considered data and to the very poor sensor steering accuracy, resulting in a very unstable attitude Doppler contribution. In comparison, the theoretical achievable accuracy estimation (considering Cramer-Rao bound) is around 100 Hz with the considered signal sampling.

A subset of the data belonging to the three cycles was finally analyzed with the MLS algorithm, which is the most accurate but the most computationally demanding too. As expected the obtained accuracy (3σ), about 130 Hz, was slightly lower than the one obtained with the ACCC method. However it is clear that it is not possible to go under an accuracy of 100 Hz for the Wind Scatterometer ERS-2 data.

In conclusion, the performed analysis, aimed at assessing the feasibility investigation of global ocean surface current mapping using the ERS-2 Wind Scatterometer data, has shown

that it is indeed possible to retrieve the Doppler information from the scatterometer data. However, due to the data characteristics (very reduced sampling and very poor attitude information) it is not possible to achieve the desired estimation accuracy (e.g. <10 Hz) as detailed in section 1. Consequently, the feasibility study was then continued by exploiting the simulated datasets (provided by CLS).

The proposed Doppler estimation technique foresees the transmission of a dual-chirp (sum of LFM chirps with opposite rates) and exploits the range-Doppler coupling effect: LFM chirps with opposite rates are delayed in opposite directions by a common Doppler shift. Through the estimation of the relative delay between the two range compressed signals it is then possible to retrieve the Doppler shift affecting the acquisition. The relative time delay can be estimated with the standard cross-correlation technique, used for instance in SAR interferometry for the coregistration of the images.

The results obtained over the simulated datasets (provided by CLS) showed that an accuracy of about 40 Hz at an across-track resolution of about 25 km can be achieved for a single pass of the scatterometer and with good SNR levels. In particular it was shown that the estimation accuracy strongly depends on the SNR level and on the desired across-track resolution, e.g. by increasing the estimation window size (reducing the spatial resolution) it is possible to improve the accuracy. Furthermore it was noticed that errors in the on-board Doppler demodulation process can bias the Doppler shift estimates.

Finally, regarding the dual-chirp concept the best approach from a systemic point of view could be the transmission of two juxtaposed opposite chirps. This would allow to maintain the transmitted power constant for the whole transmitted waveform, unlike the case of transmitting the sum of the opposite chirps. In so doing, the pulse duration, moreover, should be lower than the sea surface decorrelation time in order to perform the cross-correlation over correlated scenes.

Altogether the study has shown that the technical implementation of Doppler shift anomaly retrievals from scatterometry is feasible, and a simulator has been developed and made available to ESA. In conclusion it is therefore recommended that this DOPSCAT study could be extended with further investigation and analyses, including further testing of the proposed dual-chirp concept over simulated and, preferably, real scatterometer data.

TASK 5000: Project coordination and management

The DOPSCAT study kicked-off after the successful negotiation meeting held at ESTEC on 29 October 2010, with NERSC (Norway) as the coordinator and CLS (France), KNMI (the Netherlands), IFREMER (France), ARESYS (Italy) and TAS (France) as project partners. The corresponding study team is listed in Table 5.1.

Partner Institute	Key Team Member
NERSC	J.A. Johannessen, K.-F. Dagestad
CLS	F. Collard, Pierre Fabry, Romain Housson
KNMI	A. Stoffelen, J. de Kloe
IFREMER	B. Chapron
ARESYS	A. Recchia
TAS	J. Richard, Vivien Enjolras

The project meeting plan is given in Table 5.2.

Date	Place	Meeting
15 March 2011	ESA-ESTEC	1st Progress Meeting
20 October 2011	ESA-ESTEC	2nd Progress Meeting
3 May 2012	ESA-ESTEC	3rd Progress Meeting
30 May 2013	ESA-ESTEC	Final Meeting

Table 5.2: *Meeting schedule.*

The project was originally planned to terminate by the end of January 2012. However, due to unforeseen delays in acquiring the EWICS data and a much more demanding task in developing and testing the scatterometer Doppler anomaly simulator a request for a no-cost extension was approved by ESA after the 3rd progress meeting at ESA-ESTEC on 3 May 2012. Following this a refined DOPSCAT timeline plan was submitted to ESA on 29 May 2012. This indicated a termination of the project in January 2013. However, further delays were encountered and the final meeting took place at ESA-ESTEC on 30 May 2013. Here, it was agreed that the final report would be delivered in early July 2013.

References Documents:

[RD1] Verspeek, J.A., A. Stoffelen, M. Portabella, H. Bonekamp, C. Anderson en J. Figa, *Validation and calibration of ASCAT using CMOD5.n* IEEE Transactions on Geoscience and Remote Sensing, 2010, 48, 1, 386-395, doi:10.1109/TGRS.2009.2027896.
see: http://www.knmi.nl/publications/fulltexts/tgrsjverspeek2027896proof.pdf

[RD2] Verhoef, A., M. Portabella, A. Stoffelen en H. Hersbach, *CMOD5.n - the CMOD5 GMF for neutral winds* Document extern project: 2008, SAF/OSI/CDOP/KNMI/TEC/TN/165, EUMETSAT, 2008.
see: http://www.knmi.nl/publications/fulltexts/cmod5_neutral_winds_1.0.pdf

[RD3] Verhoef, Anton, and Ad Stoffelen, KNMI, Ocean and Sea Ice SAF, Technical Note, SAF/OSI/CDOP2/KNMI/TEC/RP/196, OSCAT winds validation report , Product OSI-105, Version 1.0, August 2012.
see: http://www.knmi.nl/publications/fulltexts/oscat_validation_1.0.pdf

[RD4] Lin, C.C., M. Betto, M. Belmonte-Rivas, A. Stoffelen en J. de Kloe, *EPS-SG Windscatterometer Concept Tradeoffs and Wind Retrieval Performance Assessment* IEEE Transactions on Geoscience and Remote Sensing, 2012, 50, 7, 2458-2472, doi:10.1109/TGRS.2011.2180393.
see: http://www.knmi.nl/publications/fulltexts/tgrslin2180393x_4.pdf

[RD5] Lin, C., A. Stoffelen, J. de Kloe, V. Wissmann, S. Bartha and H. Schulte, *Wind retrieval capability of rotating, range-gated, fan-beam spaceborn scatterometer* SPIE conference, 2002.
see: http://www.knmi.nl/publications/fulltexts/rfscat_spie.pdf

[RD6] Mouche, Alexis A., Fabrice Collard, Bertrand Chapron, Knut-Frode Dagestad, Gilles Guitton, Johnny A. Johannessen, Vincent Kerbaol, and Morten Wergeland Hansen, On the Use of Doppler Shift for Sea Surface Wind Retrieval From SAR, IEEE Transactions on Geoscience and Remote Sensing, doi: 10.1109/TGRS.2011.2174998.

[**RD7**] Zadelhoff, G. van, A. Stoffelen, P. Vachon en J. Wolfe, *Cross polarization measurements on the ASCAT second generation*, SAF/OSI/CDOP/KNMI/TEC/RP/193, OSI-SAF, 2012.
See abstract: http://www.knmi.nl/publicaties/showAbstract.php?id=9516

[**RD8**] Stoffelen, A. en M. Portabella, *On Bayesian Scatterometer Wind Inversion* IEEE Transactions on Geoscience and Remote Sensing, 2006, 44, 6, 1523-1533, doi:10.1109/TGRS.2005.862502.
see: http://www.knmi.nl/publications/fulltexts/inversion_paper_ieee_final_form.pdf

[**RD9**] Portabella, M. en A. Stoffelen, *A probabilistic approach for SeaWinds data assimilation* Quart. J. Royal Meteor. Soc., 2004, 130, 596, 127-159, doi:10.1256/qj.02.205.
see: http://www.knmi.nl/publications/fulltexts/mss_paper_final_form.pdf

[**RD10**] Vogelzang, J., A. Stoffelen, A. Verhoef, J. de Vries en H. Bonekamp, *Validation of two-dimensional variational ambiguity removal on SeaWinds scatterometer data* J. Atm. Oceanic Technol., 7, 2009, 26, 1229-1245,
See: http://www.knmi.nl/publications/fulltexts/tdvpaper_draft5.pdf

[**RD11**] Lin, W., M. Portabella, A. Stoffelen en A. Verhoef, *On the characteristics of ASCAT wind direction ambiguities* Atmospheric Measurement Techniques, 2013, 6, 1053-1060, doi:10.5194/amt-6-1053-2013.
see: http://www.atmos-meas-tech.net/6/1053/2013/amt-6-1053-2013.html

[**RD12**] Hersbach, Hans, ECMWF, "The Usage of Scatterometer Data at ECMWF", presentation at IOVWST, 18-20 May2010.

see: http://coaps.fsu.edu/scatterometry/meeting/docs/2010_may/gridded/hersbach.pdf
[**RD13**] Collard, F., A. Mouche, B. Chapron, C. Danilo, and J. Johannessen, "Routine high resolution observation of selected major surface currents from space", in Proc. SEASAR Symp., SP-656, ESA, ESA-ESRIN , Frascati, Italy, 2008.
see: http://earth.esa.int/seasar2008/participants/287/pres_287_Collard.pdf
[**RD14**] Stoffelen, A.C.M., PdD Thesis, Utrecht University, 1998,
see: http://igitur-archive.library.uu.nl/dissertations/01840669/inhoud.htm
[RD15] ER-IS-EPO-GS-0201, ERS Ground Stations Products specification, Issue 3.1
[RD16] RMA-SIC-011109, Scatterometer Algorithm Review, Royal Military Academy, Signal and Image Centre, Brussels— Belgium.
[RD17] Madsen, S., "Estimating the Doppler Centroid of SAR Data", *IEEE Transactions on Aerospace and Electronic Systems,* vol. 25, no. 2, March 1989
[RD18] CLS-DAR-NT-12-137, DOPSCAT simulator high level description
[RD19] Iwashita, K.; Moriya, T.; Tagawa, N.; Yoshizawa, M., "Doppler measurement using a pair of FM-chirp signals," *Ultrasonics, 2003 IEEE Symposium on* , vol.2, no., pp.1219,1222 Vol.2, 5-8 Oct. 2003
[RD20] Cook, C., Radar Signals: An Introduction to Theory and Application

Annex 1: Overview of KNMI simulation software

The KNMI scatterometry simulation software basically executes the following steps:

(i) it imports a measurement geometry and expected noise values for each radar beam from a so called PseudoL1B file. In previous projects this was an input provided by other partners in the project, but unfortunately this turned out not to be possible in this current project. Alternatively a simple ASCAT- or QuikScat-like antenna geometry can be calculated. Since antenna details and signal processing are no part of this simulator, a constant Kp value must be supplied to allow adding noise to the system.

(ii) in a next step input winds for the simulation can be defined from a wide range of options. In the current study we either used a predefined constant wind vector as input, repeated many times, or we generated the u,v wind components for many wind vectors from a given Gaussian distribution with a fixed half width of 5.5 m/s for each wind component.

(iii) then the simulator loops over the wind vectors and for each input wind vector it executes these steps:

- it calculates the expected signals for each antenna, using the empirical GMF functions
- it adds instrument noise (based on the given *Kp*)
- it adds geophysical noise N_G (based on a parametrization as function of wind speed w) for wind speeds below 16 m/s:
-

$$N_G = \left(L_A / L_R\right)^{1/3} 6.44 \times 10^{-4} (16 - w)^2 \qquad \text{(eq. A1)}$$

For WVC sampling L_A of 25 km, and a reference resolution L_R of 50 km, this adds 13% noise at 0 m/s wind speed and 5% noise at 6 m/s. Above 16 m/s wind speed this noise term reduces to zero. Geophysical noise is caused by wind variability on the ocean surface and the imperfect sampling of each backscatter measurement of the WVC area. NOTE that this noise term is defined at and should only be applied to the NRCS at WVC level.

- it executes the standard KNMI wind retrieval routine as defined in our GenScat software, which is identical to what is used in operational processing for ASCAT and other instruments
- finally the found wind retrieval results are written to output files

The above simulator is mostly written in Fortran90. It implements the inner loops of the simulator and has been interfaced to the python scripting system (adding the outer loops) to allow fast and easy development and visualization. Using this scripting system the following features have been added:

- calculation of several possible Figure-of-Merit values (see section 2)
- the actual simplified calculation of the ASCAT and QuikScat geometries used for this study
- addition of Doppler signals to the ASCAT geometry definition
- looping over different locations in the swath (different WVC's)
- looping over different input wind vectors
- averaging of FOM results over expected climate distribution for wind vectors (Weibull distribution)

For ASCAT we only simulate one side of the instrument (this is implied in the next sections). The following simplified calculation was used to calculate the geometry of the antennas for ASCAT for the center of a given WVC with index iwvc:

$$x = 336 + iwvc * 25 \qquad \text{(eq. A.2)}$$

$$\beta = x / R \qquad \text{(eq. A.3)}$$

$$\beta_{side} = \arcsin\left[\sin(\beta) * \sqrt{2}\right] \qquad \text{(eq. A.4)}$$

$$L = \sqrt{(R+H)^2 + R^2 - 2(R+H)R\cos(\beta)} \qquad \text{(eq. A.5)}$$

$$L_{side} = \sqrt{(R+H)^2 + R^2 - 2(R+H)R\cos(\beta_{side})} \qquad \text{(eq. A.6)}$$

$$\gamma = \arcsin\left(\frac{R}{L}\sin(\beta)\right) \qquad \text{(eq. A.7)}$$

$$\gamma_{side} = \arcsin\left(\frac{R}{L_{side}}\sin(\beta_{side})\right) \qquad \text{(eq. A.8)}$$

$$\theta_{mid} = \beta + \gamma \qquad \text{(eq. A.9)}$$

$$\theta_{fore} = \beta_{side} + \gamma_{side} \qquad \text{(eq. A.10)}$$

$$\theta_{aft} = \theta_{fore} \qquad \text{(eq. A.11)}$$

in which the earth radius R is taken to be 6370 km, the satellite height H is taken to be 822 km. x denotes the distance to nadir for the center of each WVC, β denotes the angle between the lines from satellite to earth center, and from earth center to ground intersection. The result for the side looking antennas (fore and aft) is obtained by assuming a flat earth. The distance from satellite to ground intersection L is calculated using the cosine rule. The antenna looking angle γ is calculated using the sine rule. A small value for β is assumed, so we use the approximation $\beta = \sin \beta$. Finally the beam azimuth angles ϕ are assumed to be -45, 0 and 45 degrees, so the effect of orbit inclination is neglected. This is justified because the final FOM results are integrated over all possible wind directions with a constant weight for each wind direction.

For QuikScat, the following simplified calculation, assuming a flat earth, was used to calculate the geometry of the antennas for the center of a given WVC with index iwvc:

$$x = iwvc * 25 \qquad \text{(eq. A.12)}$$

$$\phi_{inner} = \arccos\left(\frac{x}{700}\right) \qquad \text{(eq. A.13)}$$

$$\phi_{outer} = \arccos\left(\frac{x}{900}\right) \qquad \text{(eq. A.14)}$$

$$\phi_{inner,fore} = -\phi_{inner} \qquad \text{(eq. A.15)}$$

$$\phi_{outer,fore} = -\phi_{outer} \qquad \text{(eq. A.16)}$$

$$\phi_{inner,aft} = -\phi_{inner} \qquad \text{(eq. A.17)}$$

$$\phi_{outer,aft} = -\phi_{outer} \qquad \text{(eq. A.18)}$$

The incidence angles are hard coded in this case to ϕ_{inner}= 46.25 and ϕ_{outer}= 54.25 for the inner and outer beam.